Excited State Dynamics in Semiconductor Nanostructures

Andrew Michael Sills

A thesis presented for the degree of

Doctor of Philosophy

School of Electronic and Electrical Engineering

The University of Leeds

UK

30 June 2017

Submitted in accordance with the requirements for the degree of Doctor of Philosophy

The University of Leeds

School of Electronic and Electrical Engineering

June 2017

The candidate confirms that the work submitted is his own and that appropriate credit has been given where reference has been made to the work of others.

Contents

List of Figures

List of Tables

This page is intentionally left blank

Acknowlegements

I would like to thank my friends and family. My supervisors Marco Califano and Paul Harrison, and also the EPSRC for supporting me with the DTG. Thankyou very much for all your help and support.

Physical properties of InSb

Breakdown field	$103 V cm^{-1}$
Mobility Electrons	$7.7104 cm^2 V^{-1} s^{-1}$
Mobility Holes	$850 cm^2 V^{-1} s^{-1}$
Diffusion coefficient Electrons	$2103 cm^2 s^{-1}$
Diffusion coefficient Holes	$22\ cm^2 s^{-1}$
Electron thermal velocity	$9.8105 m s^{-1}$
Hole thermal velocity	$1.8105 m s^{-1}$
Crystal structure	Zinc Blende
Group of symmetry	$Td2 - F43m$
Number of atoms in 1 cm^3	2.941022
Debye temperature	160 K
Density	$5.77\ g cm^{-3}$
Effective electron mass	$0.014 m_o$
Effective hole masses mh	$0.43 m_o$
Effective hole masses mlp	$0.015 m_o$
Electron affinity	$4.59 eV$
Lattice constant	$6.479 \mathring{A}$
Optical phonon energy	$0.025 eV$

List of Publications

i. A. Sills, M. Califano. "Origins of improved carrier multiplication efficiency in elongated semiconductor nanostructures. " *Physical Chemistry Chemical Physics*, vol 17, no 4, pp 2573-2581, 2015.

ii. A. Sills, P. Harrison and M. Califano "Exciton dynamics in InSb colloidal quantum dots. " *The Journal of Physical Chemistry Letters,* vol 7, no 1, pp 31-35, 2016.

Abstract

Over the past two decades quantum-dot-based photovoltaic devices have been attracting a lot of attention due to their *potential* high efficiencies and low cost fabrication. Unlike conventional photovoltaic devices where the absorption of a single photon always produces a single electron hole pair (exciton), quantum-dot-based devices can generate multiple excitons from the absorption of just a single photon. Thanks to this process, which is referred to as either carrier multiplication or multiple excition generation, quantum-dot-based devices can potentially reach higher efficiencies breaking the Shockley-Queisser limit. In addition, the colloidal synthesis techniques used to fabricate these devices are potentially very cheap and scalable. Despite the intrinsic potential of these devices, they are not currently at a stage where they can compete with commercial photovoltaics. In this thesis various factors that effect the efficiency of carrier multiplication are investigated. In addition new analytical methods are developed to form a contribution to theoretical work in this field.

Chapter 1

Intoduction

1.1 Photovoltaics

1.1.1 Beating the Shockley-Queisser Limit

The Shockley-Queisser (S-Q) limit is a good place to start a general summary of photovoltaics. This limit has long since been the benchmark against which the efficiencies of solar cell devices are measured. It is defined as the theoretical maximum efficiency of a single p-n junction solar cell device [1]. This limit is based on the conversion rate for a single pn junction solar cell with an ideal band-gap of 1.34 eV, which delivers a maximum efficiency of 33.7%. This ideal band-gap matches the peak frequency of the solar spectrum, which is roughly approximated by a black-body spectrum with the temperature of the surface of the sun (6000K), as shown in equation 1.1

$$\int_{\nu_g}^{\infty} \frac{1}{\exp\left(\frac{h\nu - qV}{kT_c}\right) - 1} \frac{2\pi\nu^2}{c^2} d\nu, \tag{1.1}$$

where q is the carrier charge, V is the inbuilt potential, T_c is the temperature and ν is the photon frequency.

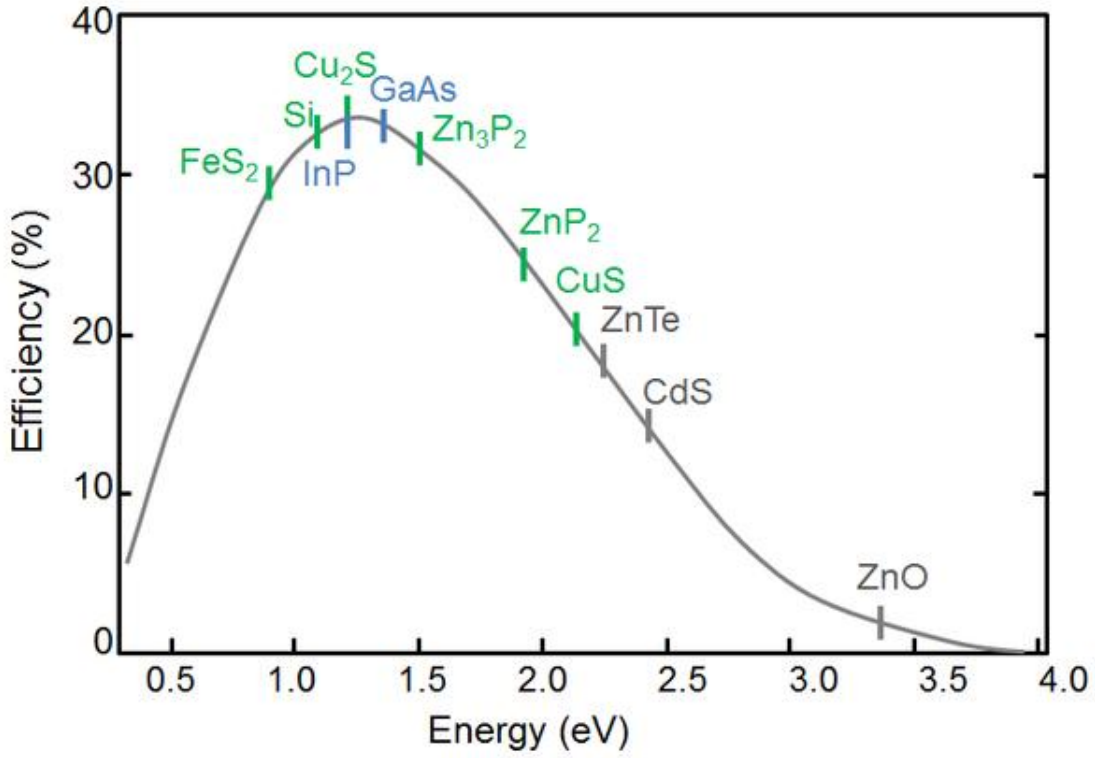

Figure 1.1 Shockley-Queisser limit for different single junction solar cells, based on solar black-body emission (image from actu.epfl.ch)

Solar cell engineering is often centred around beating the S-Q limit, which can be achieved in 4 different ways:

i. *Generation of more than one exciton (electron/hole pair) per incoming photon. (carrier multiplication);*

ii. *Use of multiple junctions with different band-gaps;*

iii. *Highly efficient relaxation, i.e., exciton relaxation not in excess of the band-gap energy, therefore no energy lost to phonon scattering;*

iv. *Use of optical instruments to concentrate sunlight;*

1.1.2 Efficiency Ratings

The most recent solar cell efficiency records (by NREL) are shown in 1.2. This type of graph gives a detailed comparison of the efficiency records together with a history of progress made for various types of photovoltaic devices. These include multi-junction solar cells, single-junction gallium arsenide solar cells, crystalline silicon solar cells and thin-film photovoltaics. Quantum dot solar cells are currently classed as emerging photovoltaics, which are typically studied in academia rather than industry. Given their promising attributes, it is highly likely that within the next two decades quantum dot solar cells will reach efficiency levels that allow them to be competitive with conventional photovoltaic devices, paving the way for large scale manufacture.

1.1.3 Single-Junction Silicon Solar Cells

Crystalline silicon-based solar cells make up roughly 90% of the commercial solar market [2]. There are several advantages to silicon-based photovoltaics: i) mature technology that is well understood; ii) non-toxicity, more environmentally friendly than GaAs; iii) abundance and low cost; iv) competitiveness in terms of cost per watt.

1.1.4 Single-Junction GaAs Solar Cells

High-end single-junction solar cells tend to use GaAs rather than Si due it its superior physical properties. These include high electron mobility and a band-gap that is both direct and also a close match to the peak absorption for a single junction solar cell (1.4 eV). In addition, its growth mechanisms are well understood compared to other

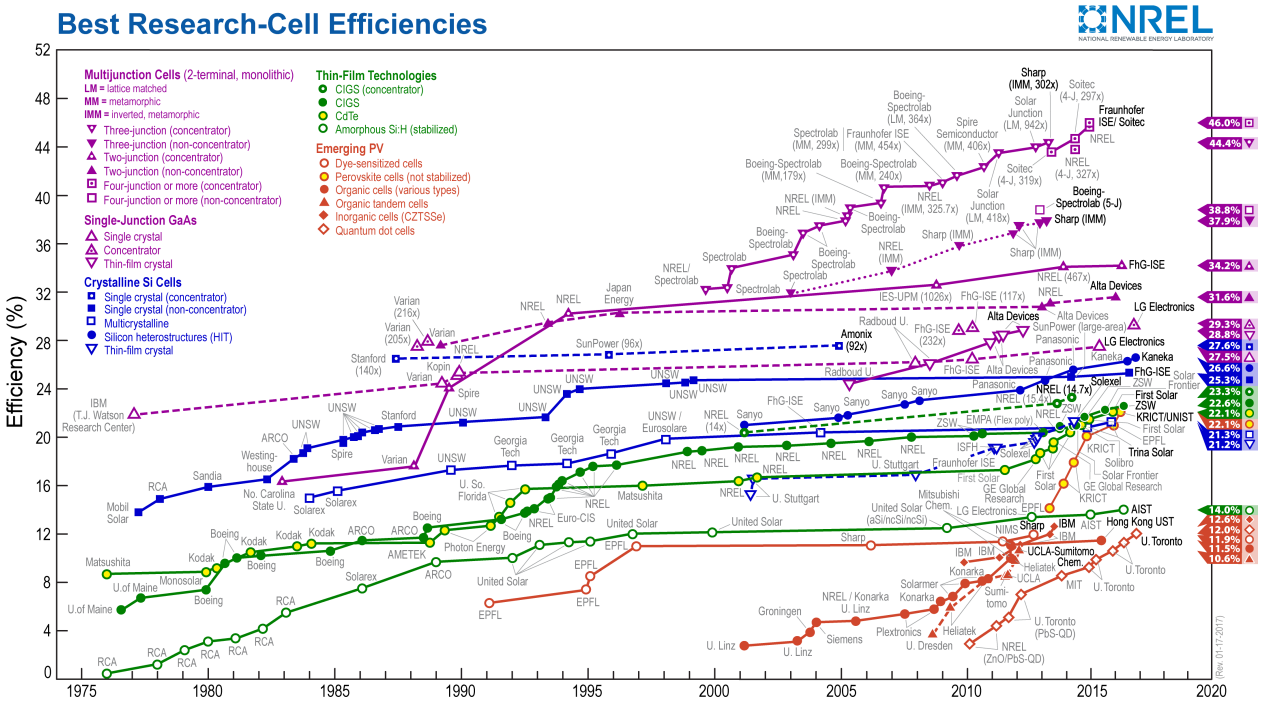

Figure 1.2 Solar Cell efficiency records for different types of semiconductors: (i) multi-junction cells, (ii) single-junction gallium arsenide cells, (iii) crystalline silicon cells, (iv) thin-film technologies, and (v) emerging photovoltaics.

direct band-gap III-V semiconductors. The theoretical maximum efficiency of GaAs single-junction cells is 33.16%. [3]. There are studies that link GaAs to cancer [4] and, although the evidence is by no means conclusive, this remains a major obstacle for its widespread commercial use.

1.1.5 Multijunction Cells

Multiple pn junctions are used to harvest photons with different energies across the full solar spectrum using several layers of semiconductor material. Each separate layer of material is carefully tuned to a specific wavelength of light. The theoretical maximum efficiency (under concentrated light) increases with the addition of more layers: 55% (two layers), 63% (three layers), up to 86% for an infinite number of layers [5] [6].

The ability to experiment with different numbers of layers and complex compound semiconductors means the efficiency records for these type of devices are increasing at a much faster rate than for single-junction solar cells. The manufacturing process can be very expensive due to the high costs of the precision epitaxial fabrication techniques required. Unfortunately, this additional fabrication cost leads to an increase to the cost of electrical power, with a cost to watt ratio that is typically higher than the cheaper single junction solar cells. This means they tend to be used in more niche applications where space and weight are at a premium. Examples include satellites or the new generation of solar based aeronautics. Incentives to drive down fabrication costs have led to the development of cutting-edge fabrication methods [7]. Further development of this technology could make multi-junction technology a mainstream commercial success.

1.1.6 Thin-Film Technologies

A thin-film of semiconductor is deposited on a substrate. The main advantage of this technology has historically been reducing manufacturing costs. However, more recently highly optimised film technologies have been used to produce devices with efficiencies of 22% [8] using a copper indium gallium diselenide (CIGS) film, which is highly competitive with crystalline silicon.

1.1.7 Emerging PV

Emerging PV are relatively new technologies in the early to mid stages of development. However, these technologies are rapidly catching up record efficiencies of more mature technology. Types of emerging PV include dye-sensitized cells [9], perovskite cells [10], organics cells [11] and quantum dot solar cells [12].

1.1.8 Light concentration

Optical instruments such as lenses and curved mirrors can be used to focus sunlight onto a small highly efficient solar cell. This is typically used with expensive multi-junction solar cells where higher light concentration increases the efficiency of the device [13–15].

1.2 Quantum Dot Solar Cells Configurations

Experimentalist have fabricated colloidal quantum dot solar cells in a number of different configurations. These methods are not dissimilar from those used in bulk semiconductor devices. For example, the Schottky quantum dots solar cells [16, 17] exploit the intrinsic built-in electric field between a conductive oxide layer and a metal contact to generate a photocurrent. Heterojunction quantum dot solar cells employ a layer of quantum dots on a transparent conductive oxide where diffusive exciton transport and exciton separation at the interface is used to generate a photocurrent [18–22].

Chapter 2

Carrier Multiplication in Quantum Dots

2.1 Colloidal Quantum Dots

Colloidal quantum dots (QDs) are semiconductor crystals dispersed in solution and passivated with organic ligands. These nanoscale structures were first observed in 1983 [23] and assigned the name quantum dot a few years later [24]. Due to their unique physical properties they have gone on to be incorporated into a number of electronic and optoelectronic devices, including photovoltaic cells, photodetectors, [25–27] and light-emission devices. [28–30]. The key feature is the quantum confinement effect which allows the optical and electronic properties to be tuned by carefully controlling the size [31,32] and structure [33]. In addition, the low cost of production [34] makes nanocrystals a very exiting prospect for a variety of next generation devices.

2.2 Quantum Confinement

Quantum confinement occurs when the dimensions of a material become of a similar size to the exciton Bohr radius, which is the expected distance between an electron-hole pair in the bulk. The confinement causes a change in the electronic and optical properties of a system: it increases the energy of the electronic states, thus leading to a widening of the band-gap and hence a blue shift in the emission spectra. This is often referred to as the size factor of quantum dots (shown in figure 2.1), where the band-gap can be tuned by controlling the size of the structures.

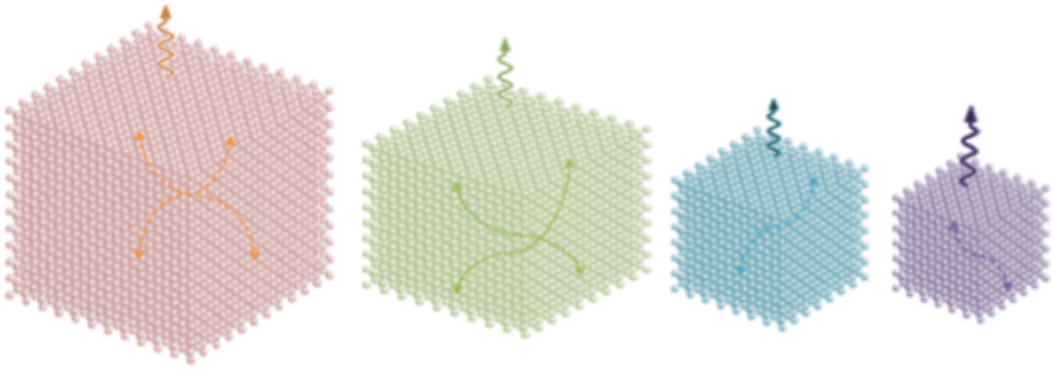

Figure 2.1 The size tunability of colloidal quantum dots.

In bulk semiconductors the dimensions of the crystal are much greater than the exciton Bohr radius. Therefore excited carriers are not confined, and the electronic and optical properties are determined by the properties of the crystal. In nanostructures (quantum wells, wires, dots, etc.) the size of the structure is on the same order of magnitude of the exciton Bohr radius:

$$a_b^* = \epsilon_r \left(\frac{m}{\mu}\right) a_b, \tag{2.1}$$

where a_b is the Bohr radius for a hydrogen atom at its ground state ($0.053nm$), m

is the mass, μ is the reduced mass, and ϵ_r is the size-dependent dielectric constant (relative permittivity). Excited states are created by the absorption of an incoming photon with a high enough energy to promote an electron from the valence band (VB) to the conduction band (CB). In bulk semiconductors the number of atoms is so high that these states form continuous bands. However, in confined structures there is a set of discrete energy levels, not dissimilar to individual atoms (they have an energy and momentum component). For this reason quantum dots are sometimes referred to as *artificial atoms*.

2.3 Colloidal synthesis

Colloidal quantum dots self-assemble in solution. The nucleation process can be carefully controlled by varying the interfacial tension, supersaturation and temperature of the solution to produce structures of a desired size and shape [35–39], including novel structures such as quantum rods [40–42] and quantum tetrapods [43–45].

2.3.1 Carrier Multiplication

Excited state dynamics in confined semiconductors differs vastly from the bulk. In conventional solar cell devices, the energy from an incoming photon usually excites a single exciton. Energy in excess of the band gap is typically dissipated in the form of phonon scattering. In a nanostructure where carrier multiplication is effective, high-energy photons are expected to excite on average more than a single electron across the band gap. This mechanism, known as Carrier Multiplication allows QDSC to beat the Shockley-Queisser limit [1]. To date Carrier Multiplication has been observed in nanocrystals made of a wide range of different semiconductors [46–50]. This provides

many options for future quantum-dot-based photovoltaic applications. However, a better understanding of the physical mechanism of CM is required in order to improve the overall efficiency of the device, i.e. the percentage of incident light converted into electricity. This relates to the internal quantum efficiency, which is defined as the ratio of the of carriers collected by the solar cell to the number of incident photons. Currently, the best recorded internal quantum efficiencies for quantum dot solar cells are still far from 200%) [51, 52], and in order to improve this factor, carrier multiplication needs to be better understood, so that the mechanism can be exploited to give improved performance, and compete with conventional photovoltaic devices in terms of both cost and efficiency. CM is typically described in terms of impact ionisation (II) [12, 46, 53–55], a term originally used to describe this process in bulk materials: the photon energy in excess of the band-gap, rather than being lost to the lattice in the form of phonons, can be transferred by one of the two photogenerated carriers to an electron in the valence band, exciting it to the conduction band, and creating a further exciton (for a total of two excitons generated per absorbed photon, see Fig. 3.1a).

2.4 Carrier Multiplication & Auger Recombination

The absorbed photon energy must be at least twice the band-gap E_g for carrier multiplication to take place [12]. In other words the excess energy of the carrier should be at least equal to the band-gap. If this is the case then a second valence electron can be excited across the band gap to create a bi-exciton. The inverse process is known as Auger recombination (AR), where a bi-exciton (XX) recombines to form an exciton (X). Interestingly, both impact ionisation and Auger recombination share

the same transition matrix elements. Such a relationship between II and AR has been cited as a reason for dismissing impact ionisation [56, 57] as the source of CM in NCs. This claim was base on the perceived incompatibility between the $\sim$ 10 ps AR lifetimes and the observed $<$ 400 fs CM decay. The crucial difference between the two processes. However, is that the initial states in the former represent the final states in the latter and *vice versa*.

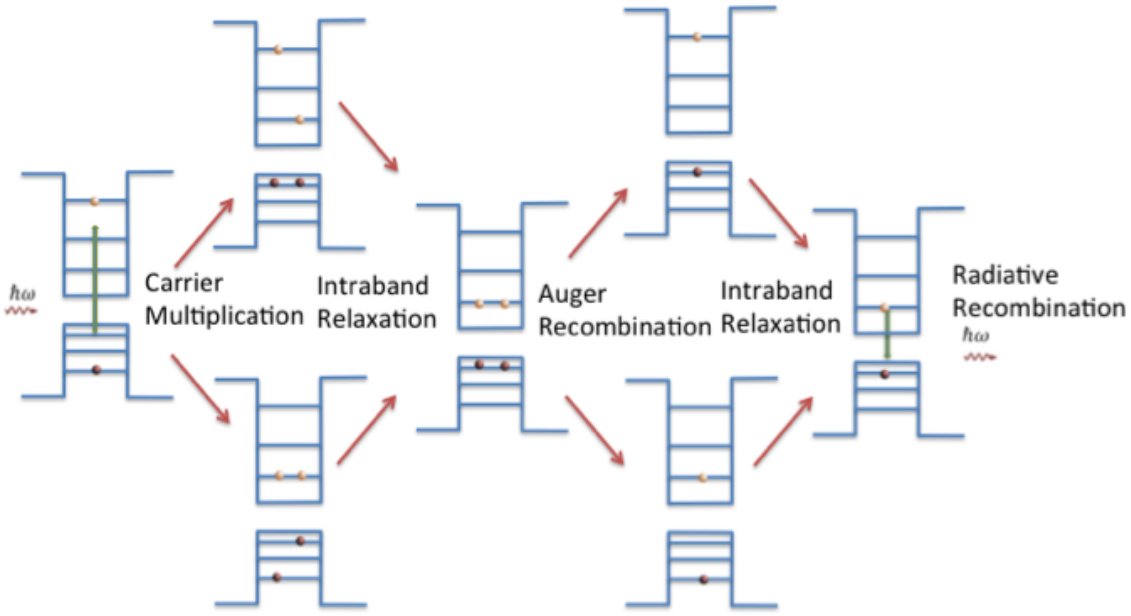

Figure 2.2 Exciton decay pathways: Carrier Multiplication, intra-band relaxation, Auger recombination and radiative recombination.

If, according to theory, a structure exhibits very fast Auger recombination rates, then the carrier multiplication rates will also be expected to be extremely fast, which is an excellent property for quantum dot solar cells.

Chapter 3

Origins of improved Carrier Multiplication in quantum rods

In this Chapter we investigate carrier multiplication in elongated structures [58]. The CM onset corresponds to a point at which CM becomes favourable since the density of bi-exciton states, $\rho_{XX}(E)$ is greater than or equal to the density of single exciton states, $\rho_X(E)$. Although the CM onset has been shown to be independent of the NC size, for spherical NCs of a specific material [59,60], it has also been shown to depend on the NC *shape*, specifically in elongated structures. [61–65].

Therefore further theoretical and experimental work is required on this subject [66] to shed light on these experimental findings. New insights into the origins of improved carrier multiplication could provide further incentives for future work in this field. Aside from the choice of material, the shape and size of the nanocrystals is a very specific feature that can be controlled in the design of the PV device. In a nutshell, careful control of the shape can provide tailor made band-gaps, with a favourable density of states, which is arguably the key factor in determining the efficiency of

carrier multiplication.

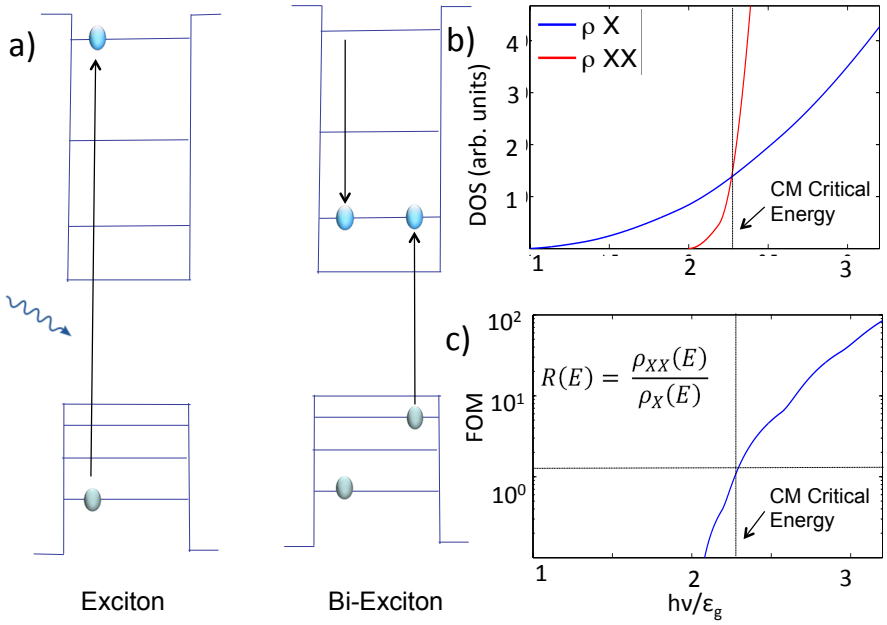

Figure 3.1 (a) Schematics of CM via impact ionisation. (b) Density of single exciton (blue) and bi-exciton (red) states versus energy for cubic GaAs NCs with sides of 10 lattice constants. (c) Ratio of red and blue curves in (b) plotted on a logarithmic scale to show a figure of merit (FOM) characteristic.

3.1 Improving Carrier Multiplication

The goal here is to specifically look at the improved carrier multiplication that has been observed in elongated structures. The origin of this effect could be attributed to many possible factors (listed below):

i. *the larger volume of the rod, when compared with a spherical structure with the same band gap, leading to a larger absorption cross section;*

ii. *a larger surface-to-volume ratio, leading to an increase in surface-related effects (such as ligand- or trap-mediated processes or other environmental effects);*

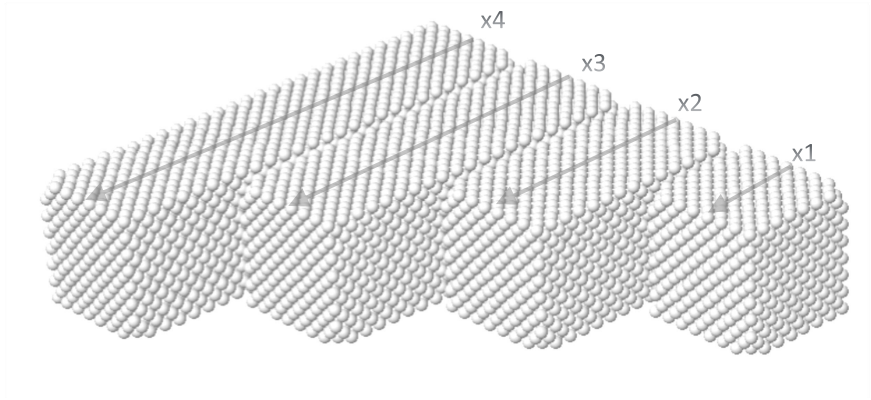

Figure 3.2 Elongated nanostructures with aspect ratios of 1,2,3 and 4. During the elongation process a large increase in the density of states occurs while the shift in band-gap is relatively small.

iii. *a different electronic structure leading to an increased (bi-excitonic) density of states (DOS);*

iv. *the enhanced Coulomb coupling that binds electrons and holes into well defined 1D excitons , leading to bimolecular (i.e., two-body) Auger interactions between the two excitons in rods [67], compared to the three-body interactions between free carriers in spherical NCs [68].*

Here we investigate the possible origins of the observed lowering of the CM onset by isolating the electronic structure effects (iii) from surface-related effects (ii), absorption effects (i), and effects due to enhanced Coulomb interaction (iv). By using a single-band effective mass model with an infinite potential barrier, we prevent the carriers wave functions from sampling the surface, effectively removing surface effects (ii) from the calculation. It could be argued that this approach is over simplistic and does not take the finer atomistic details of the structure into account. However, another way to put it would be to say the finer details are isolated from the model, and

if the effect of improved efficiency can be explained with a simple model, then that shows something interesting in itself, i.e. that the theory underpinning this model is the dominating effect for the improved carrier multiplication.

At the same time this approach allows us to investigate a range of elongations otherwise inaccessible to more accurate atomistic approaches, due to the prohibitively large numbers of atoms involved. By describing excitons in the single-particle picture, where $E(X) = E(e_i) + E(h_j) + E_g^{\text{bulk}}$ (see (3.5)), we neglect enhancement effects of the Coulomb interactions between electrons and holes due to confinement, excluding (iv). We then consider the single- and bi-exciton DOS following the absorption of a single high-energy photon, thereby excluding possible effects due to variations in the absorption cross section (i). We finally compare the effect of elongations at constant cross section with that of elongation at constant volume. We find that as the aspect ratio (i.e., the elongation) of the structure increases, so does the single-particle DOS in both the valence and the conduction bands. This leads to an increase in both single- and bi-exciton densities of states, with the latter increasing at a faster rate, though, causing a decrease in the energy E_0 at which the two curves cross (which is closely related to the energy position of the CM onset). This effect is important as a lowering of the CM onset is associated with increased CM efficiency [69, 70] and enhanced solar energy conversion [59, 71].

Theoretical work on carrier dynamics has shown that the available final (i.e., XX) states [53–55] and also that the AR rate to the number of final X states [72]. Therefore CM can occur at a faster rate than AR when the density of bi-exciton states $\rho_{XX}(E)$ is greater than the density of single exciton states $\rho_X(E)$ (see Fig. 3.1b). The ratio of these densities $R(E) = \rho_{XX}(E)/\rho_X(E)$ is hereby referred to as the CM figure of merit (FOM) [73] and is a useful parameter in the determination of NC efficiency. Ideally,

for solar cell applications, this ratio should be greater than unity, which, using this model would suggest a higher rate of II than AR. Conversely, a reduced $\rho_X(E)$ could be indicative of a reduction in the efficiency of phonon-assisted relaxation, the main mechanism competing with II. Indeed, tight-binding calculations [55] have shown that at high energies impact ionisation rates are comparable in bulk and nanostructured PbSe, which may suggest that the increase in efficiency caused by the relaxation of momentum conservation rule in the latter may be compensated by a reduced efficiency in phonon-assisted decay, due to a sparser density of electronic levels.

The importance of $R(E)$ has also been confirmed by the results of recent ab-initio time-dependent density functional theory calculations combined with non-adiabatic molecular dynamics [74], which interestingly also showed that multiple exciton *recombination* (AR) is only possible for energies in the window of opportunity $2E_g \leq E < 3E_g$, i.e., close to the crossing point between $\rho_{XX}(E)$ and $\rho_X(E)$. An alternative model proposed by Klimov explains CM in terms of direct generation of multiexcitons via Coulomb coupling to virtual single-exciton states [56]. In this model the CM efficiency depends on the ratio of the bi-exciton and single exciton generation rates, and therefore on $R(E)$.

Following the convention, [54, 55, 73] we define the CM critical energy E_0 as the energy at which $R(E) = 1$ (Fig. 3.1c). Above this energy CM rates are larger than AR rates, i.e., bi-exciton generation becomes faster, leading to more efficient carrier multiplication. The CM onset E_{onset} is defined as [54] $\max(E_0, E_{\text{opt}})$, where E_{opt} is the minimum photon energy such that either of the photo-generated carriers has sufficient energy to initiate CM. In this work we will be concerned with possible strategies to engineer the critical energy E_0. In particular, we will show that experimental observations of lower CM onsets in elongated nanostructures correlate with theoreti-

cal predictions of reduced values for E_0, thereby establishing a close correspondence between critical energy and CM efficiency.

The size-tunability of the band-gap is well established in NCs (blue shift in emission spectra with increased confinement). However, a model for the tunability of the CM onset requires consideration of the band-structure and in particular of the distribution of states just above the bi-exciton ground state energy $2E_g$. A theoretical study on the effects of the band structure on CM efficiency was conducted by Luo *et al.* [73] using the infinite-barrier truncated-crystal approximation (TCA) within the semi-empirical pseudopotential method. They calculated the CM FoM for *cubic* NCs of different sizes (l=$6a_0$, $8a_0$ and $10a_0$, where a_0 is the lattice constant), made of different materials, and found that it was larger for PbSe, Si, GaAs, CdSe, and InP, suggesting a lower CM onset and therefore higher efficiency for these materials. They concluded that high CM efficiency requires high degeneracy in the bulk band-edge states. As a consequence of its peculiar electronic structure [75], where both CBM and VBM are located at the 4-fold degenerate L-point, PbSe was shown to have the highest CM Figure of Merit (FoM). Conversely, InAs was found to have one of the lowest efficiencies, from this point of view, given its large Γ-L and Γ-X spacings in the bulk, which prevent any confinement-induced Γ-to-L and Γ-to-X electronic transitions in small NCs. In other materials (such as GaAs, InSb, and GaSb), small Γ-L spacings in the bulk cause the electron states to derive from the L-point Bloch state, in sufficiently small NCs, leading to larger CM efficiencies.

Since the publication of Luo's work, advances in colloidal synthesis techniques have paved the way for the manufacture of cubic nanostructures (cubic quantum dots and square-sectional quantum rods) for a variety of semiconductors of different sizes [76–79] using self-assembly techniques.

Cubic nonocrystals exhibit a higher packing density than spherical dots [80]. This is something worth noting as the long term interest of developing PV devices is that they are able to compete with mainstream technology. Also, it has been shown that the dot surface provides the main contribution to both CM rates and Auger multi-exciton recombination rates. It is still unclear whether the advantages of improved CM outweigh the disadvantages of increased Auger rates. However, cubic structures have twice the surface area to volume ratio of spherical structures, specifically $6/a$ for cubic and $3/a$ for spherical.

Also, recent breakthroughs promise even cheaper colloidal synthesis for nanocrystals, making the technology potentially more scalable [81].

Unlike in spherical or cubic structures, where electrons and holes experience equal quantum confinement in all three spatial dimensions, in an elongated structure the confinement is relaxed along one dimension, creating a quasi one dimensional system where the band-gap is largely determined by the smaller dimensions. However, as the elongation increases, the decrease in the confinement energy along that direction reduces the energy spacing between neighbouring states, increasing the DOS in both valence and conduction bands.

A group lead by Victor Klimov was the first to present experimental evidence to support the hypothesis that the CM onset is a useful parameter in determining the CM efficiency for PbSe NCs [69], reinforcing the importance of the former being as close to $2E_g$ as possible [66]. More recent experimental studies investigating the behaviour of this characteristic in quantum rods have revealed a general reduction in the CM onset for PbSe quantum rods compared to their dot-like siblings with similar band-gaps. However, the energy value to which the onset converges with elongation and the aspect ratio at which convergence is achieved are still controversial [62–64].

Cunningham et al. [62] measured an increase of CM efficiency and a concomitant reduction of E_{onset} from 2.9 to 2.33 for aspect ratios increasing from 1 to 4-5 in cylindrical structures with a diameter of 4.4 nm, while Sandberg et al. [63] observed a decrease from 3.2 to 2.6 in the electron-hole pair creation energy for aspect ratios reaching up to 7-8, albeit in narrower structures, with typical diameters of 3-3.6 nm.

This particular interest in PbSe nanostructures originates from a number of reasons: (i) the band-gap is small enough to allow CM for low energy photons corresponding to the infrared region of the electromagnetic spectrum; (ii); the unique band structure gives an extra 4-fold degeneracy in both conduction and valence band edges [75]; (iii) the relatively large dielectric constant causes a reduction in carrier-carrier interactions, leading to an increase in the exciton Bohr radius, which can, in theory, be up to the length of the rod [67]. However nanostructures made of a number of other materials may offer alternative advantages: e.g., ease of integration with existing Si-based technology (Si and Ge), more ideally placed band-gap for solar absorption (InAs, InSb), more mature colloidal technology (CdSe, CdS), etc. We therefore decided to screen a large sample of different materials.

We aim to first validate our method by comparing its results for non-elongated structures with the CM critical energies calculated by Luo *et al.* [73]. We will therefore consider cubic NCs with the same dimensions as those used in reference [73], which, as mentioned above, are now experimentally accessible in a variety of semiconductor materials and in different sizes. [76–79]

3.2 Methodology

There are many possible methods that can be applied to nanostructures in order to obtain the electronic structure, ranging from computationally expensive atomistic methods to more accessible continuum based approches. The reasoning behind using a simple single band model has already been discussed. The electronic structure in both the conduction (CB) and valence band (VB) is calculated using the eigenvalues solutions of the Schrödinger equation 3.1 for a quantum box with an infinite confining potential (the charge distribution of the 6 lowermost states is shown in Fig. 3.3a):

$$\frac{\hbar^2}{2m^*}\nabla^2\psi\left(x,y,z\right) = E_{x,y,z}\Psi\left(x,y,z\right) \tag{3.1}$$

$$\psi\left(x,y,z\right) = \psi_x\psi_y\psi_z \tag{3.2}$$

$$\psi\left(x,y,z\right) = \sqrt{\frac{2}{L_{x,y,z}}}\sin\left(\frac{\pi n_k x}{L_{x,y,z}}\right) \tag{3.3}$$

$$E^{CB,VB}_{x,y,z} = \frac{\hbar^2\pi^2}{2m^*_{e,h}}\left(\frac{i^2}{L_x^2}+\frac{j^2}{L_y^2}+\frac{k^2}{L_z^2}\right) \tag{3.4}$$

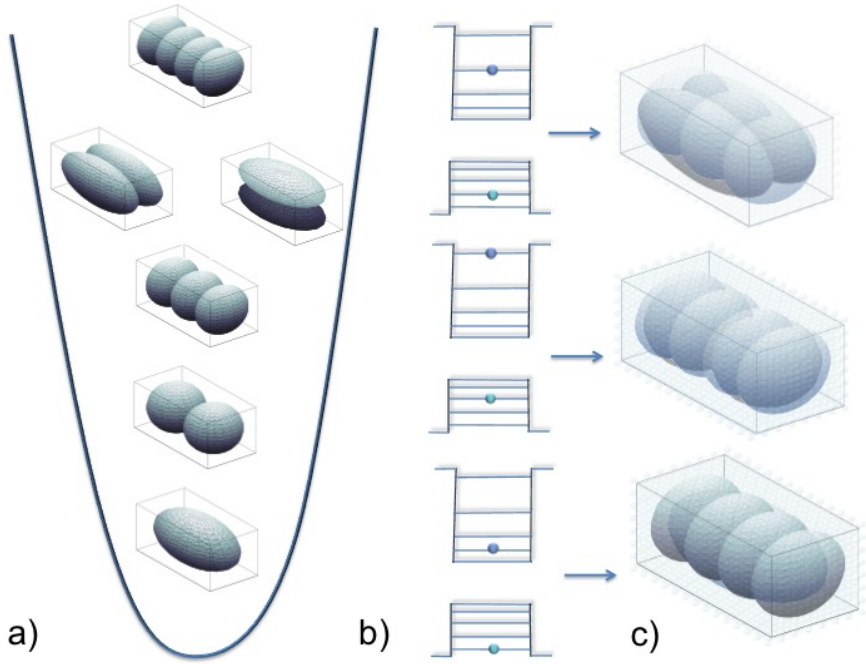

Figure 3.3 (a) The charge density of the 6 states closest to the band edge (111, 112, 113, 121, 211, 114) for a nanorod with aspect ratio 2. (b) Possible single-exciton configurations and (c) their corresponding charge distributions.

where the effective mass parameters listed in table 3.1 were used. In order to make sure that all energy levels within a specific energy window $[E_{min}, E_{max}]$ are included in the calculated DOS, a maximum quantum number n^{max} $(n = i, j, k)$ is pre-calculated, defined as the highest quantum number yielding an energy within the window while the other two $(m, l \neq n)$ are set to one. e.g. $E_{1,1,k^{max}} < E_{max}$ and $E_{1,1,k^{max+1}} > E_{max}$.

The single-exciton energies E_X are then obtained as

$$E^X_{i,j,k} = E^{CB}_{i,j,k} + E^{VB}_{i,j,k} + E_g^{\text{bulk}}, \tag{3.5}$$

where E_g^{bulk} is the bulk band gap for the given semiconductor material (possible single-exciton configurations are schematically shown in Fig. 3.3b in the single-particle picture, together with their charge density - Fig. 3.3c). In our approach we therefore

neglect (a) higher energy bands (such as the L valleys in GaAs, GaSb and InSb), (b) band anisotropies, and (c) excitonic effects, the most important of which is the red shift of the band edge due to electron-hole Coulomb attraction. Furthermore, the infinite potential is known to overestimate the confinement energy, as in reality there is a finite probability of the carriers to exist in the barrier. One possible strategy to compensate for this, is to model the structure as being slightly larger than its actual dimensions. Bryant *et al.* [82] showed that a better agreement with the measured optical gaps could be achieved by assuming $L' = 1.3L$, where L' is the overestimated cross sectional width of the dot. Here we choose not to follow this route and let the reader decide which size to use in the comparison with experiment (indeed the ratio between two consecutive sizes considered in this work - $6a_0$, $8a_0$ and $10a_0$ - is nearly 1.3). It has been suggested [73] that the inclusion of higher valleys [point (a) above] is important in the calculation of the DOS. However, here we are mainly concerned with the determination of the energy E_0 at which the *ratio* between the DOS is equal to 1. This quantity may be less sensitive to the details of the band structure at high energy. Indeed our calculated values for E_0 show a reasonable agreement with the results of the TCA (see Fig. 3.9 below), where the effects of higher bands are properly taken into account [73]. This result therefore provides a validation *a posteriori* of our simple approach.

The electronic structure of semiconductor nanocrystals has been previously investigated using a variety of theoretical approaches: (i) effective mass models and $k \cdot p$ methods [83–86] often provide analytical solutions which are easier and more intuitive to understand than the numerical results of atomistic methods, such as (ii) the tight-binding method [87–92], (iii) the semi-empirical pseudo-potential method, [93, 94], and (iv) fully self-consistent *ab-initio* methods, based on density functional the-

	m_e	m_h	$E_g(eV)$	$ExBohr(nm)$
GaAs	0.067	0.45	1.52	14
GaSb	0.041	0.4	0.81	23
InAs	0.023	0.41	0.42	42
InP	0.43	0.6	1.43	9.8
InSb	0.25	0.41	0.24	88
CdSe	0.13	0.43	1.75	4.9
Si	0.328	0.49	1.13	5.8
Ge	0.2194	0.33	0.74	22
PbSe	0.058	0.054	0.28	46

Table 3.1 Parameters used in the present calculations. For highly anisotropic semiconductors such as Si, Ge and PbSe the reported value is the average between longitudinal (m_l) and transverse (m_t) masses, according to the following expression $m^* = \sqrt[3]{m_l^2 m_t}$.

ory [95–102].

One advantage of the continuum single-band effective mass approach over atomistic methods is computational simplicity: the latter can become expensive when simulating very large structures such as nanorods, containing tens of thousands of atoms. Another attractive aspect of this choice is the possibility of completely decoupling the NC core from its surface in the calculations and therefore isolating electronic structure effects from possible environmental effects (such as interactions at the surface with ligands, unsaturated bonds, and the solvent), by using infinite potential barriers which prevent the carriers' wave functions from sampling the nanostructure's surface.

We are interested in the densities of exciton and bi-exciton states within the energy range $2E_g<E<3E_g$, i.e., just above the energy threshold for bi-exciton generation, but excluding higher order multi-excitons. In their determination, it is important to consider Pauli's exclusion principle for each exciton and bi-exciton state. For example, while determining the degeneracy of a single exciton $X_{\alpha,\beta} = |e_\alpha; h_\beta\rangle$ [where e_α (h_β) is the electron (hole) state $\alpha = i, j, k$ ($\beta = h, l, m$), solution of (3.4)] is simple (it is always four, including pseudo-spin), the case of a bi-exciton $XX_{\alpha,\beta,\gamma,\delta} = |e_\alpha, e_\beta; h_\gamma, h_\delta\rangle$ is slightly more complicated and depends on whether the two electrons in the CB and

the two holes in the VB are in the same state or not (i.e, whether or not $\alpha = \beta$ and/or $\gamma = \delta$).

Once the energies and degeneracies of exciton and bi-exciton states have been calculated for both cubic and elongated structures, the FoM $R(E)$ is obtained as the ratio of their DOS (Fig. 3.1c). The energy at which $R(E) = 1$ (the point where the curves $\rho_{XX}(E)$ and $\rho_X(E)$ intersect, see Fig. 3.1b) is then obtained for several values of the aspect ratio, keeping either a constant cross section (and varying the volume) or a constant volume (and varying the cross section).

Luo *et al.* [73] pointed out that since the Coulomb operator in the Auger matrix elements only couples states that differ by no more than two particles, one should consider the ratio $\rho_{XX}(\varepsilon, E)/\rho_X(\varepsilon, E)$, between the bi-exciton and exciton DOS, where *one carrier is fixed* in the single-particle level at energy ε. This led them to introduce the quantity

$$R_2(E) = \frac{1}{N(E)} \int_{\varepsilon_{\min(E)}}^{\varepsilon_{\max(E)}} \rho(E) \frac{\rho_{XX}(\varepsilon, E)}{\rho_{X(\varepsilon,E)}} d\varepsilon \tag{3.6}$$

as CM figure of merit. The results of their calculations show little difference between the curves $R(E)$ (which neglects the Coulomb selection rule) and $R_2(E)$ for most materials, especially regarding the energy E_0 at which they are equal to 1. As the determination of such an energy is the main focus of our investigation, for the sake of simplicity we will therefore neglect Coulomb selection rules and consider R.

The single-particle DOS calculated for VB and CB are shown in Fig. 3.4. Most of the simulated semiconductor NC structures have a larger DOS in the VB than in the CB. Due to the very small electron effective mass in InAs, the DOS in the CB of nanocubes made of this material is very low; whereas the symmetric band structure for PbSe is instead a consequence of the roughly similar electron and hole effective

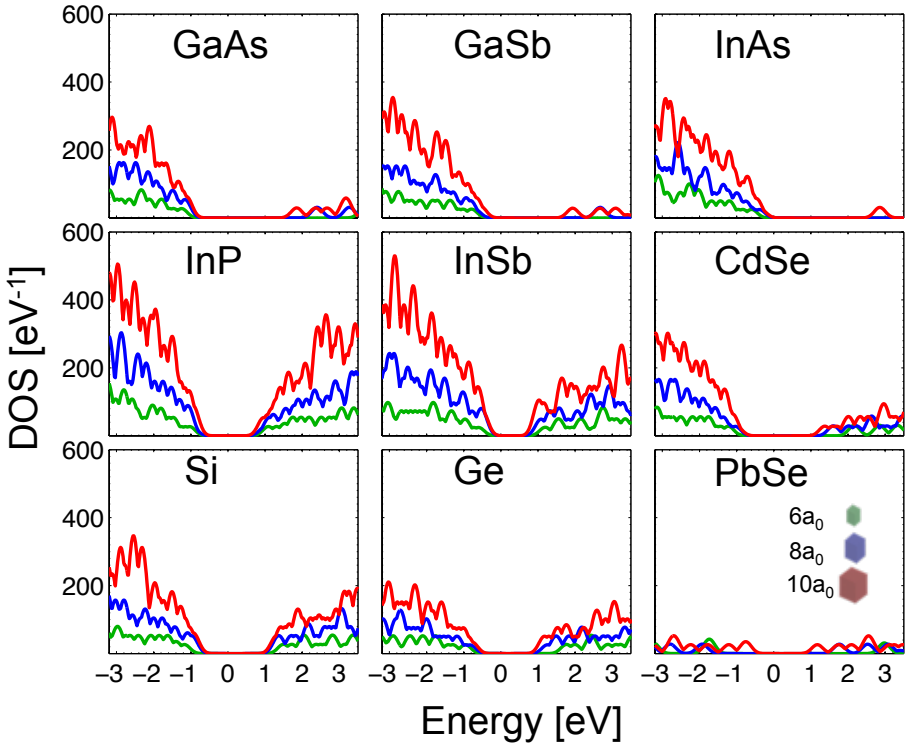

Figure 3.4 The single-particle density of states for cubic NCs of different materials (GaAs, GaSb, InAs, InP, InSb, CdSe, Ge, Si and PbSe) for three different dot sizes (red $L = 10a_0$, blue $L = 8a_0$, and green $L = 6a_0$, where a_0 is the lattice constant and L is the length of the cube).

masses used in the calculation (see Table 3.1). InP NCs appear to have the highest DOS in both bands, while at the same time having a relatively large band gap.

Compared to the cubic NCs shown in Fig. 3.4, a fourfold increase in volume (aspect ratio) yields, for most materials, a decrease in the band-gap similar to (or smaller than) that obtained with a 25% increase in the cube size, with, however, a much larger increase in the corresponding density of states in the elongated structures, particularly significant at the band edges.

Starting from these single-particle DOS we then calculated the single- and bi-exciton DOS, and finally the CM FoM.

Before presenting the effects of elongation on the CM critical energy, we will vali-

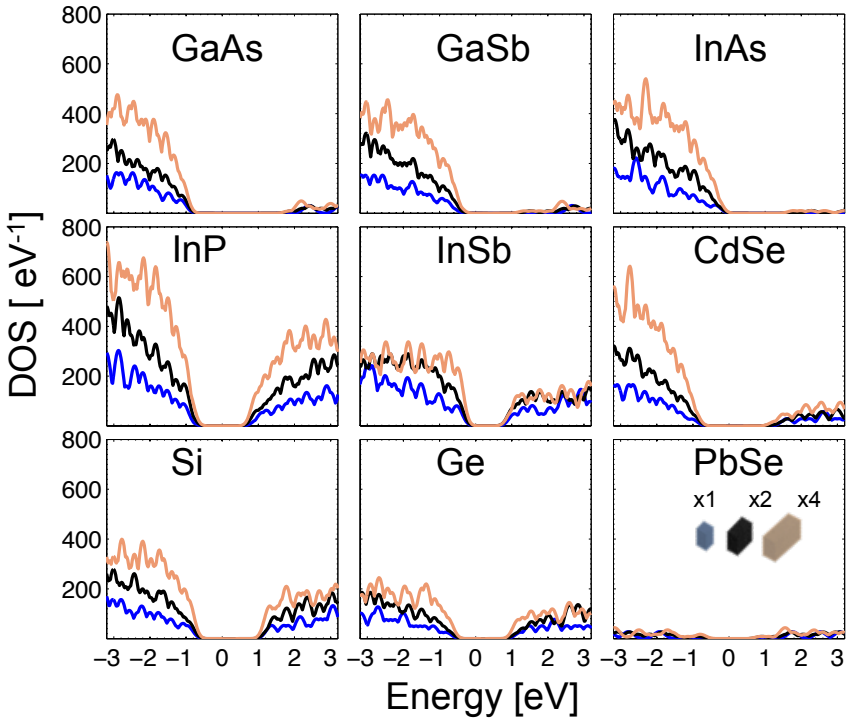

Figure 3.5 The single-particle density of states for square cross-section nanorods of different materials (GaAs, GaSb, InAs, InP, InSb, CdSe, Ge, Si and PbSe) for three different aspect ratios (1, blue line; 2, orange line; and 4, black line) with a constant cross section of $8a_0^2$, where a_0 is the lattice constant. Compared to the cubic NCs shown in Fig. 3.4, a fourfold increase in volume (aspect ratio) yields, for most materials, a decrease in the band-gap similar to (or smaller than) that obtained with a 25% increase in the cube size, with, however, a much larger increase in the corresponding density of states, particularly significant at the band edges.

date our method by comparing its results for cubic structures (i.e. aspect ratio = 1) with those obtained with the truncated crystal approximation [73]. Our calculated CM FoM are displayed in Fig. 3.6 (solid lines) for all materials considered, as a function of the excitation energy: our results show a clear size dependence in most of the cases, except for InAs and PbSe, in good agreement with observations in these two systems [60, 71]. This lack of size dependence is due in InAs to the extremely sparse conduction band: a much larger increase in size than what we consider here would be required to access higher energy levels in this band.

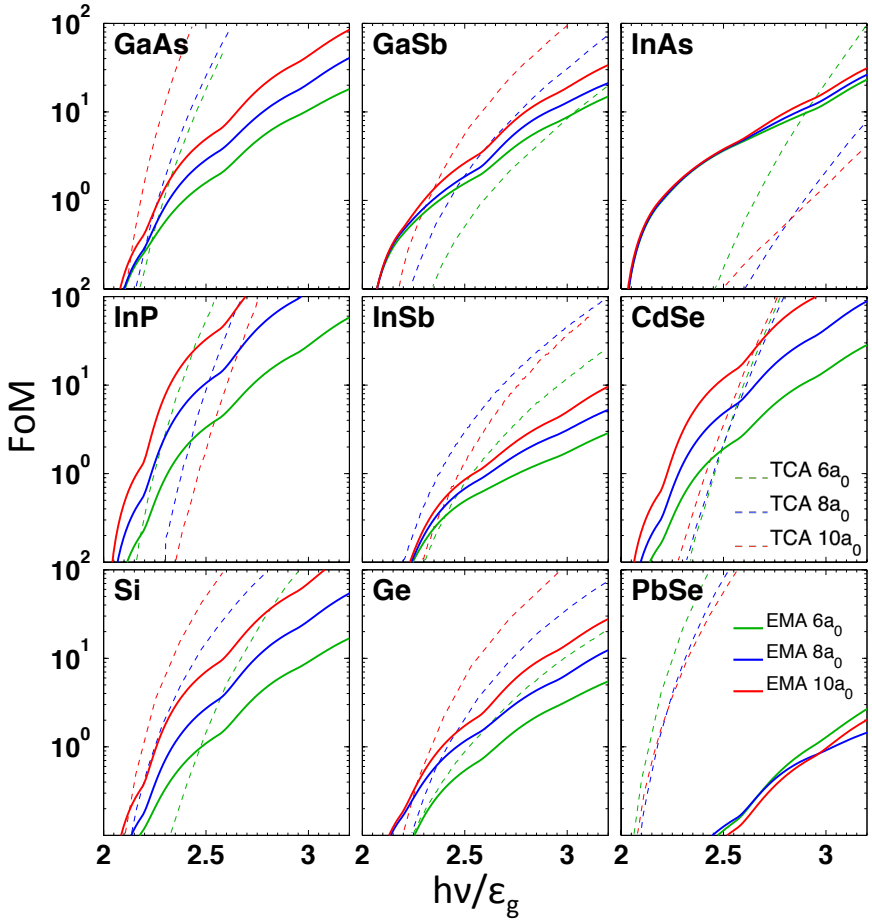

Figure 3.6 Figure of Merit characteristics for cubic NCs of different materials (GaAs, GaSb, InAs, InP, InSb, CdSe, Ge, Si and PbSe) for three different dot sizes ($L = 10a_0$, red lines; $L = 8a_0$, blue lines; and $L = 6a_0$, green lines. a_0 is the lattice constant and L is the length of the cube). Solid lines: present work; dashed lines TCA [73].

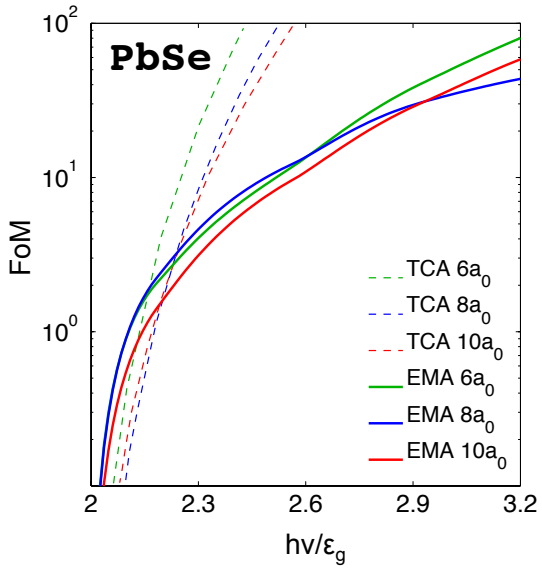

Figure 3.7 PbSe FoM: Same as in figure 3.6, with the extra 4 fold degeneracy at the band edges included.

The results of TCA are presented in Fig. 3.6 as dashed lines. The two approaches predict similar trends for the CM FoM as a function of photon energy in most of the materials considered (with some quantitative differences at the boundaries of the energy region of interest), except in the case of InAs, where TCA predicts a more marked size dependence, in contrast with experiment [71]. On the other hand our calculations predict a clear size dependence for CdSe NCs, in contrast with TCA and experiment [48].

The FOM for PbSe shown in Fig. 3.6 was obtained using the solutions of (3.4), i.e., without accounting for the extra degeneracy of the bulk band edges in this material. The effect of this degeneracy is illustrated in Fig. 3.7, where 3 extra states were added by hand at the band edges, to simulate the 4-fold degenerate L states in bulk PbSe (for consistency with our method (3.4), the results presented below were all obtained without including this "artificial" degeneracy). Our calculated CM critical energy in

Fig. 3.6 shows better agreement with the experimentally determined CM onset [46], compared to that obtained using TCA, whereas the value of E_0 presented in Fig. 3.7 shows a closer comparison to the TCA results.

Most of the FoM characteristics shown in figure 3.6 compare reasonably well with the TCA, in particular for energies close to $2E_g$. We find that for most semiconductors the CM critical energy is closer to $2E_g$ for larger structures and shifts to increasingly larger values with decreasing size, following the expected decrease in the single-particle DOS.

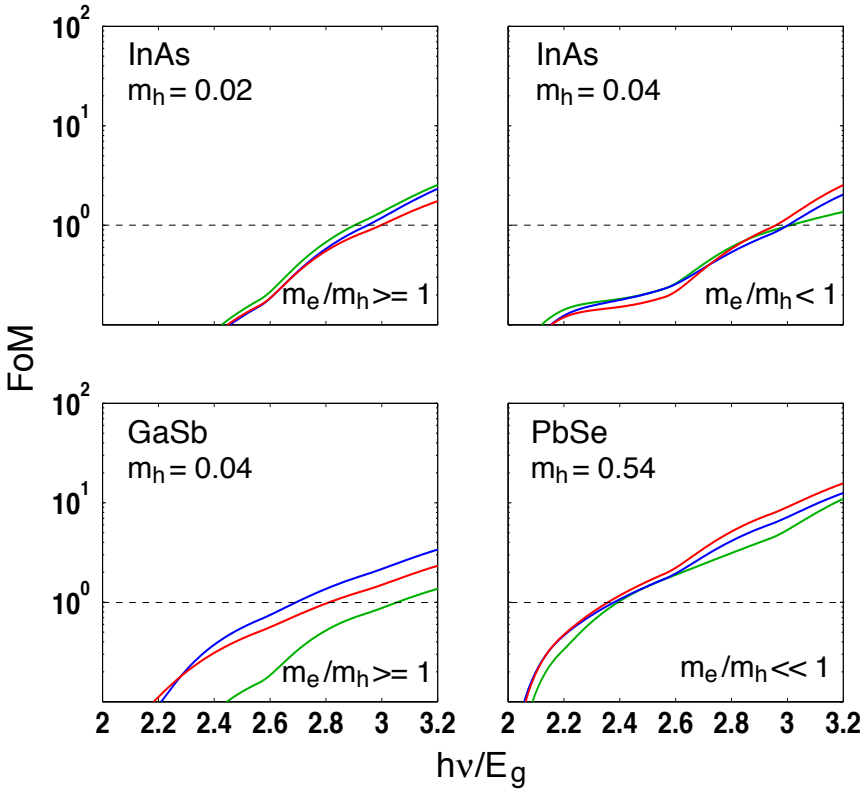

Figure 3.8 Recalculated FoMs for InAs, GaSb and PbSe using the same parameters as in figure 3.6, with the exception of the value of the hole effective mass (reported in the plots).

However, an inverse size dependence can also occur, i.e. larger dots can exhibit a reduced E_0 with an increase in size. This can happen in strongly confined systems,

when the decrease in band-gap has a greater effect than the increase in the DOS, causing an overall reduction of the number of states in the window of opportunity $2E_g < E < 3E_g$. For the work presented here only PbSe (exciton Bohr radius in the bulk $R_{\mathrm{Bohr}} = 46$ nm) shows this inverse size dependence, while the CM critical energy calculated for InAs is size-independent. In the work reported by Luo *et al.* [73], instead, this inverse size dependence was found in InP and to a lesser extent also in PbSe and InAs (in both of which complete inversion occurred only after intersection with the $R(E) = 1$ line, see Fig. 3.6) and InSb (where only the two curves relative to the largest sizes were found in reverse order). If strong confinement were the only origin of this effect, then, using the value of the bulk exciton Bohr radius as an estimate of it, we would expect InSb (which has the largest value of R_{Bohr} among the materials considered) to exhibit the most marked inverse size dependence, followed (with decreasing values of R_{Bohr} [103]) by PbSe, InAs, GaSb, InP and so on. However, as this is not the order found in neither our calculations nor in those performed by Luo *et al.* [73], we speculate that other properties (such as the value of electron and hole effective masses and their ratio) play an important role in determining the actual size dependence. To confirm this we re-calculated the FoM for: (a) InAs using two different hole effective mass values about one order of magnitude smaller than the actual ones and similar to that of the electron ($m_h = 0.02m_0 \lesssim m_e$ and $m_h = 0.04m_0 > m_e$); (b) GaSb with $m_h = 0.04m_0$ (i.e., 10 times smaller than the correct value and $\sim m_e$); and (c) PbSe using $m_h = 0.54m_0$ (i.e., 10 times larger than the correct value and than m_e). We find (see Fig. 3.8) (a1) a complete inverse size dependence for InAs if $m_h \sim m_e$ and $m_e/m_h \gtrsim 1$; (a2) a photon-energy-dependent behaviour if $m_h \sim m_e$ and $m_e/m_h < 1$, where smaller sizes have larger FoM (i.e., an inverse size dependence) for $h\nu \lesssim 2.7E_g$ and then the dependence on size is reversed,

becoming "normal" for photon energies above $3E_g$; (b) a partial inversion in GaSb for $m_h \sim m_e$ and $m_e/m_h \gtrsim 1$; and (c) a normal size dependence for PbSe when $m_h \gg m_e$ and $m_e/m_h \ll 1$. As expected the CM critical energy approaches $3E_g$ as the effective mass ratio approaches 1.

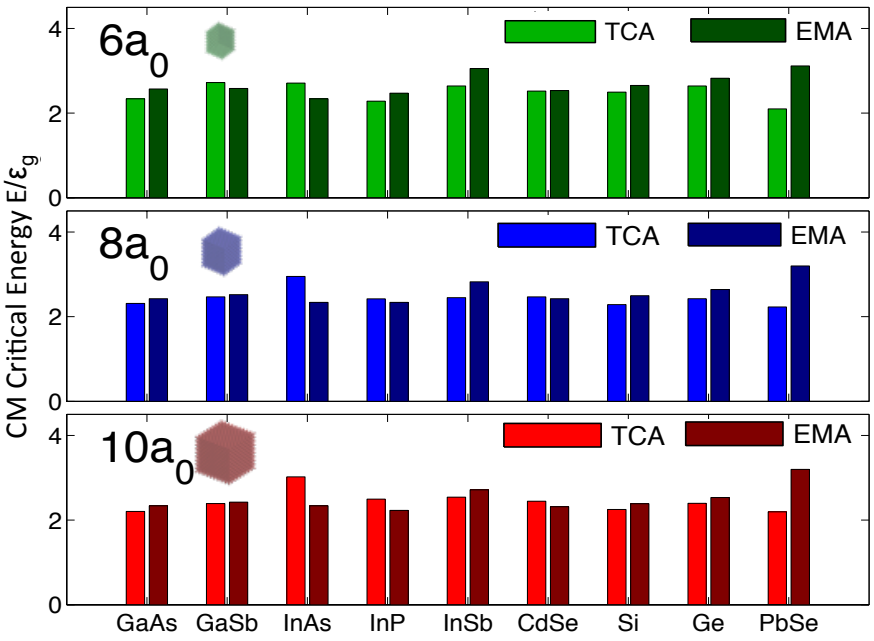

Figure 3.9 A comparison of the CM critical energies E_0 (with $R(E_0) = 1$) obtained from Fig. 3.6 for effective mass vs TCA. The color coding follows the same convention as Fig. 3.6, i.e., light and dark green: $6a_0$, light and dark blue: $8a_0$, and light and dark red: $10a_0$.

The most important question is however: how well can EMA approximate the results of TCA regarding the position of the CM *critical energy*? This is, in fact, the quantity we will focus on in elongated structures. A detailed comparison of the CM critical energies obtained with the two methods is presented in Fig. 3.9, where for PbSe we report the results from Fig. 3.6 (i.e., without the additional 4-fold degeneracy of the band edges used in Fig. 3.7). This is the set we will use in our elongated structures calculations. The agreement is generally quite good for all materials and NC sizes,

except for InAs and PbSe (and, to some extent, InSb) which are also the materials that exhibit the weakest agreement for the calculated band-gaps (not shown).

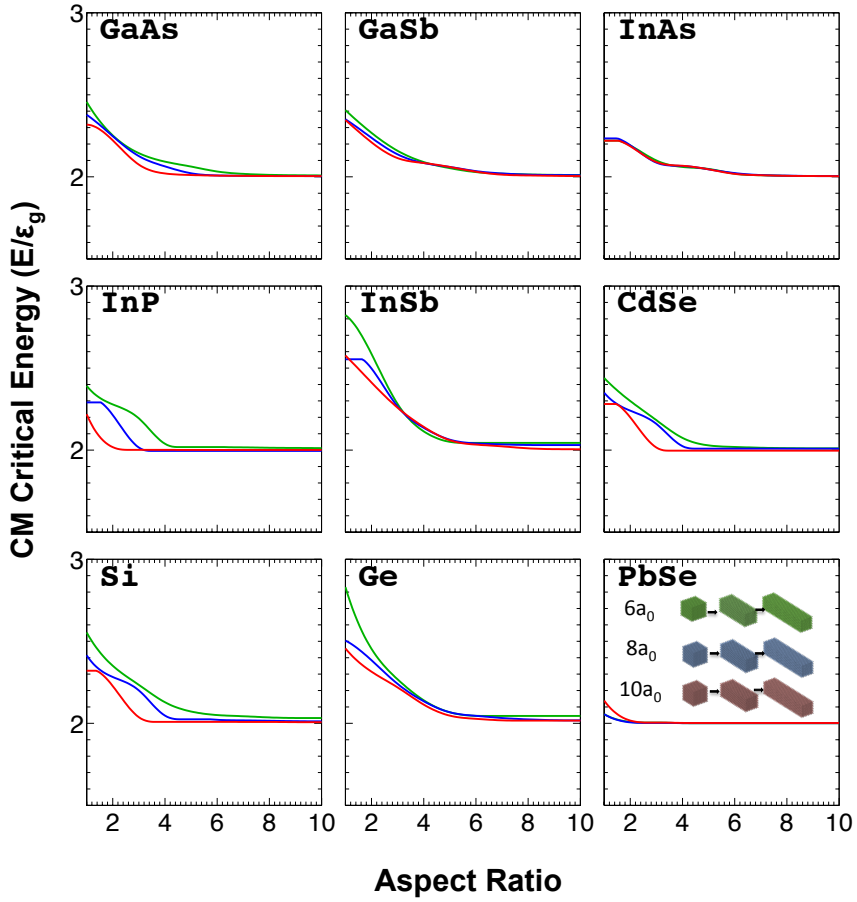

Figure 3.10 Variation of (normalized) CM critical energies as a function of aspect ratio at constant cross section calculated for three different widths $6a_0$, $8a_0$ and $10a_0$.

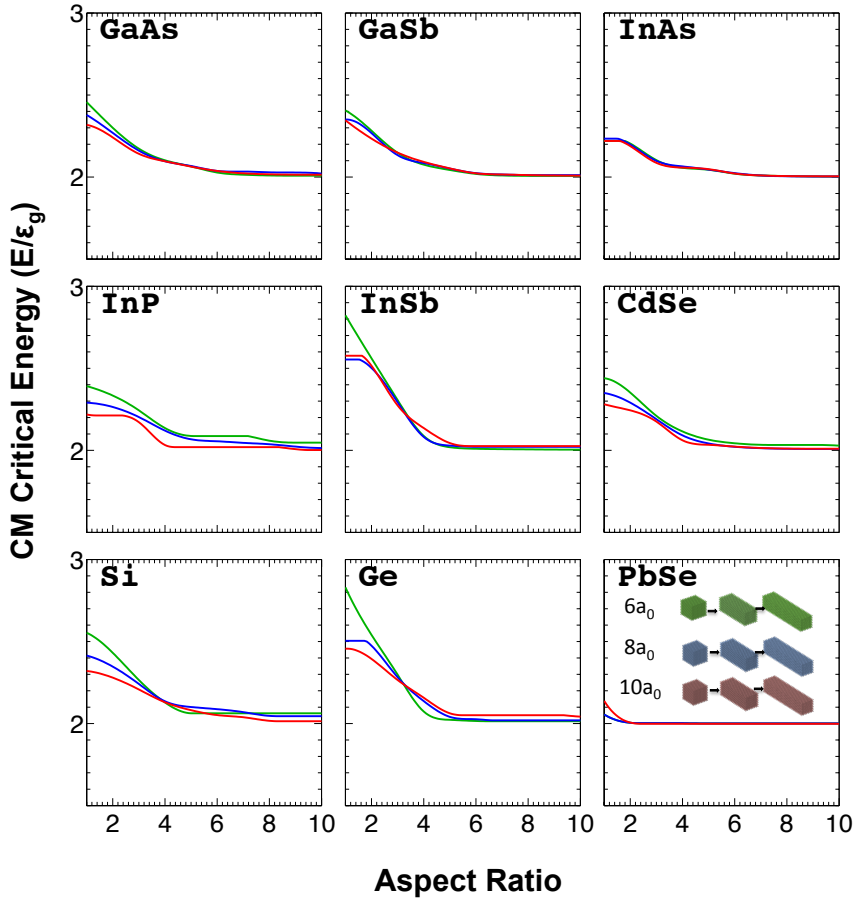

Figure 3.11 Variation of (normalized) CM critical energies as a function of aspect ratio at constant volume, calculated for three different volumes: $6a_0^3$, $8a_0^3$ and $10a_0^3$.

Having established the reliability of our calculated CM critical energies for cubic structures, we can now proceed to investigate the effects of increasing nanocrystal elongation. The variation of E_0 as a function of aspect ratio is presented in Fig. 3.10 for elongations at constant cross section, and in Fig. 3.11 for elongation at constant volume. The former case reflects the experimental conditions in which preferential growth along one direction is achieved, maintaining the cross section unaltered and

resulting in an almost constant band gap, whereas the latter case allows us to remove all possible volume-scaling effects, by keeping the volume constant and therefore varying both cross section and band gap. The general trend looks qualitatively similar in the two cases, the CM critical energy decreasing with elongation, but exhibiting a faster convergence at constant cross section, for most materials. A closer inspection of Fig. 3.10 reveals, however, a remarkable material-dependent behavior: GaAs, GaSb, InP, CdSe, Si and Ge exhibit a marked size-dependence of the aspect ratio $\sigma_{\min}$ at which E_0 converges to the minimum value of the CM onset (theoretically $2E_g$). In these materials, $\sigma_{\min}$ ranges from about 2 (in InP) to 5 (in Ge and GaSb) for the largest structures, and from about 6 (in CdSe) to ~ 10 (in Ge), and even > 10 (see below), for the smallest rods, and is always inversely proportional to the rod size. For InAs, InSb and PbSe, $\sigma_{\min}$ is instead size-independent. In the case of PbSe rods with $L = 8a_0$ (4.9 nm) we predict a decrease of the CM critical energy from $\sim 3.0E_g$ to $\sim 2.25E_g$ for an increase of σ from 1 to 4, in good agreement with the experimental results of Cunningham et al. [62] who observed a reduction of E_{onset} from 2.9 to 2.33 for aspect ratios increasing from 1 to 4-5 in nanorods with typical diameters of 4.4 nm. Furthermore, our predicted size independence for $\sigma_{\min}$ is consistent with the recent findings of a diameter-independent maximum for the CM yields observed at aspect ratios of about 8 [65]. Indeed, according to our results, the CM threshold does not exhibit any further decrease (hence the CM efficiency is not expected to further increase) with increasing values of σ beyond about 9 (this value is also in fair agreement with experiment). Our predicted value for the CM critical energy of a $L = 6a_0$ (3.7 nm) rod with $\sigma = 8$ ($\sim 2E_g$) is, instead, in disagreement with the data reported by Sandberg et al. [63], who find a reduction of the electron-hole pair creation energy from $\sim 3.2E_g$ to $\sim 2.6E_g$ with elongation to $\sigma = 7 \div 8.4$ for rods with

average radii of 3 and 3.6 nm.

Interestingly we also find that in some materials (InP and Si) the value of E_0 for the smallest structure does not converge to the theoretically expected value of $2E_g$ for any value of the aspect ratio considered (up to 10), requiring structures longer than $60a_0$ (37 nm) to reach it.

In the case of elongation at constant volume (Fig. 3.11), we find that for all materials (except PbSe) the CM critical energy converges at much higher values of σ, compared to the case of elongation at constant cross section, with $\sigma_{\min}$ generally larger than 6 for all rod sizes considered. In this case only InP shows a size-dependent $\sigma_{\min}$ and E_0 does not converge to $2E_g$ for a larger number of materials (InP, CdSe, Si and Ge). These different features observed in Fig. 3.11 compared with Fig. 3.10 can be explained in terms of the competition between the opposite effects on the DOS caused by increased elongation (i.e., reducing confinement) along one direction (which leads to an increase in the DOS), and increased confinement in the perpendicular plane (which decreases the DOS), combined with the behavior of the band-gap as a function of aspect ratio in the two cases. For elongation at constant volume (i.e., when the cross section is reduced), the increase in confinement along the two shorter axes would lead to a decrease in the DOS, which is balanced by the large increase of both band-gap and elongation. For elongations at constant cross section, instead, there is no increase in confinement, and the decreased confinement along the structure long axis leaves the band-gap largely unchanged, after an initial small drop (materials with large bulk band-gaps, such as CdSe, exhibit the smallest decrease). In the latter case, therefore, the CM critical energy converges at lower aspect ratios than in the former.

3.3 Conclusions

A continuum approach was used to model the band structure of cubic NCs of different materials and sizes, using effective mass parameters. From the calculated single- and bi-excitonic DOS, the CM critical energies E_0 were obtained for all the structures considered. The results were found to be in good agreement with the estimates obtained with more detailed theoretical approaches. Furthermore, the level of confinement (strong vs weak) and both the absolute value of electron and hole effective masses and their ratio were found to play an important role in determining the size dependence of the CM FoM in different materials. This method was then used to explore the effect on the CM critical energies of elongation, up to sizes inaccessible to atomistic approaches. In all cases considered E_0 tends towards the theoretical absolute minimum of the CM onset of two band-gaps for sufficiently long rods. Elongation at constant cross section leads to an increase in the single-particle DOS, while keeping the band-gap nearly unchanged, making more states available in a given energy window. In structures elongated at constant volume the band-gap increases sharply due to the large decrease of the shorter axes, creating a larger energy window, and the resulting DOS is a consequence of the competition between the effects of decreased confinement along the elongation axis and of increased confinement across it. As a consequence, in the case of elongation at constant cross section (the case reflecting experimental growth conditions) the CM critical energy converges for smaller values of the aspect ratio, and, in many materials, exhibits a marked size dependence of the aspect ratio $\sigma_{\min}$ at which this convergence is achieved.

In summary, our results show that the origin of the decrease of the CM onset observed experimentally in elongated structures can be attributed purely to electronic

structure effects, as surface-related effects and effects due to both increased absorption and enhanced Coulomb coupling have been accurately filtered out in our investigation. This conclusion paves the way to the implementation of CM-efficiency-boosting strategies in nanostructures based on the lowering of the CM onset, specifically by manipulation of the geometry of the structure.

Chapter 4

Geometry of Strained Quantum Dot Structures

4.1 Introduction

This chapter focuses on accurately determining the size of computationally generated strained quantum dots. The motivation for this was to obtain better agreement between theory and experiment, for example consider two sets of results for a core-shell structure, the first set is theoretical, while the second set is experimental. It is important to make sure both sets of results are held to consistent standards of measurement. However, the current standard of determining the size of a dot theoretically does not work for strained structures. With this in mind a new code has been written to correct this problem, together with an alternative strain method and an image processing code that can read scanning tunnelling microscopy (STEM) images.

4.2 Strain

Core-shell quantum dots are fabricated with an inner core of semiconducting material surrounded by a different semiconductor as an outer shell. These two materials may have different lattice constants as, for example, the silicon/germanium core/shell structures shown in figure 4.1, where silicon has a lattice constant of $5.4331\mathring{A}$, and germanium $5.658\mathring{A}$. The difference in the natural bond lengths of these two materials causes strain on the lattice when they are bonded to one another. This lattice strain leads to bond bending and bond stretching and possibly dislocations in the lattice. The semi-empirical pseudopotential method (SEPM) does not provide any provision for this relaxation; therefore if we want to explore the effects of strain then a separate method needs to be applied to the atomic position data before solving the Hamiltonian. The valence force field method is a semi-classical method used to relax atoms within the supercell with the goal of minimising the strain energy, according to

$$\begin{aligned} E_{VFF} = \sum_i \sum_j^{nn_i} \frac{3}{8} \Big[\alpha_{ij} \Delta d_{ij}^2 \quad + \alpha_{ij} \Delta d_{ij}^3 \Big] \\ + \sum_i \sum_{k>j}^{nn_i} \frac{3\beta_{ijk}}{8 d_{ij} d_{ik}} \left[(\mathbf{R}_j - \mathbf{R}_i) \,.\, (\mathbf{R}_k - \mathbf{R}_i) \right. \\ \left. - \Big(cos\theta_{jik} \quad d_{ij} \quad d_{ik} \Big]^2 \right. \\ + \sum_i \sum_{k>j}^{nn_i} \frac{3\sigma_{ijk\cdot}}{d_{ik}} \Delta d_{ij} \left[(\mathbf{R}_j - \mathbf{R}_i) \,.\, (\mathbf{R}_k - \mathbf{R}_i) \right. \\ \left. - cos\theta_{ijk} d_{ij} d_{ik} \right], \end{aligned} \tag{4.1}$$

where $\Delta d_{ij}^2 = [[(\mathbf{R}_j - \mathbf{R}_i) d_{ij}^2]/d_{ij}]^2$. $\mathbf{R}_i$ is the position vector for an atom and Σ^{mn_i} gives the summation over the atom's nearest neighbours. Coefficients for bond stretch-

ing (α), bond angle bending (β_{jik}) and bond-length-bond-angle interaction σ_{jik} are all derived from bulk properties.

This procedure is typically applied to input geometry for both SEPM and tight binding methods when a DFT calculation is computationally expensive. More information on this method can be found in the literature [104–106].

This method needs to define parameters of a fictitious material, which will fill the vacuum section of the supercell. Arbitrary fictitious parameters can be difficult to define and the methodology does not always follow an exact science. This turned out to be one of the most problematic aspects of this method, as it was not clear how to derive the parameters for new materials.

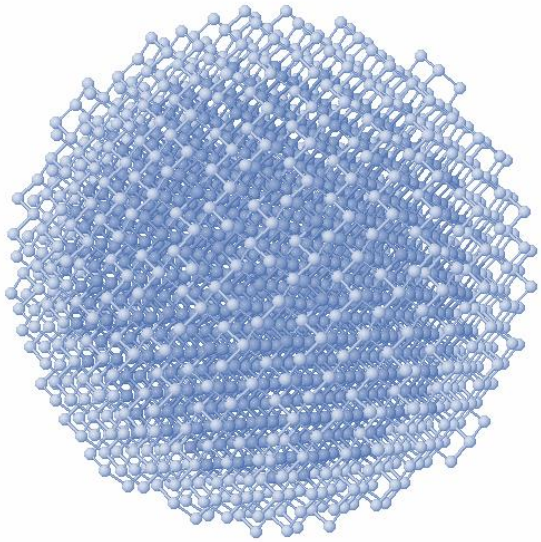

Figure 4.1 A core/shell silicon/germanium quantum dot strained using the VFF method.

4.3 Empirical Strain

A new empirical model for strain was developed as a possible alternative to the valance force field (VFF) method. The goal was to create a strain model where the bond lengths were fitted to experimental data for a core/shell QD of a particular size. A deformation function is defined to model the strain along the radius of the structure. This is used to stretch or squash the vector space which defines the lattice. This empirical model involves the physical measurement of core-shell quantum dot bond lengths using a very precise experimental method such as scanning tunnelling microscopy. The bond lengths would be sampled at several key points along the radius and fitted to a function, which would define the deformation function. The main obstacle in the application of this method is the lack of suitable experimental data. While many STEM images of core/shell quantum dots are available in publications, they are not of a high enough resolution to accurately extract the bond lengths at specific points along the structures radius.

During the development of this code an estimation of the deformation function was used as a substitute for an empirically derived deformation function. A three step linear piecewise deformation function was used, starting at the core lattice constant then rising to the shell lattice constant and then levelling off. Smoothing can be applied to make the function more continuous. It could be argued that under this type of strain neither the core nor the shell would have their native bulk like bond lengths. This could be accounted for by the deformation function, however the value would be arbitrary at best. In order to develop this model a comparison with DFT and VFF strain for the same structure would need to be implemented. One other potential application of this method would be to investigate the effect of external

forces, since the lattice can be stretched or squeezed using a defined vector field, perhaps pressure or magnetic forces. Further work would be needed to refine this model, and at present it serves as a quick approximation to strain.

The application of this model may be difficult to justify. However, one could argue that we are already using an empirical model for the atomic positions, since we are applying a lattice constant measured from the bulk. Therefore if we are already using an empirical model then an extension of the empirical model is a possibility.

4.4 Radius of Strained Structures

For unstrained spherical nanocrystals the effective radius (R) is defined as a function of the the number of atoms (N_{dot}) and the bulk lattice constant (a_0). For zinc-blend dots this is given by

$$R = 5a_0(\gamma N_{dot})^{1/3}, \tag{4.2}$$

where a_0 is the bulk lattice constant,N_{dot} is the number of atoms and $\gamma = 3/32\pi$. This relationship is derived from from consideration of the atomic density, where the number of atoms in a unit cell defines the number of atoms per unit volume. This has been the golden standard for many years. It is an elegant and accurate way to determine the radius based on the number of atoms. However, the only downside is the fact that it does not work for strained structures, where the bond lengths are non-uniform. With this in mind we look at the best method to determine the size of a structure, with the goal of finding something consistent with the effective radius. This involves using more computationally advanced geometry, such as the convex hull and the Voronoi Cell around an atom.

4.4.1 Convext Hull - *Surface Atoms*

Initially it was thought that the convex hull of the lattice points would be a robust method to determine the volume of an arbitrary structure. This is a mathematical method for defining the outer bounds for a set of (lattice) points S, i.e. the edge ($2D$) or surface ($3D$) for a set of points (illustrated in figure 4.2). The convex hull is computed by finding the set of all convex sets, and then obtaining the intersection of this set to give the convex hull. For N points $p_1, \ldots, p_N$, the convex hull C is then given by

$$C = \left[\sum_{i=1}^{N} \lambda_i p_i :\geq \forall i \cap \sum_{i=1}^{N} = 1 \right], \tag{4.3}$$

where λ is a positive coefficient associated with each point, the sum of all coefficients is always equal to unity. [107].

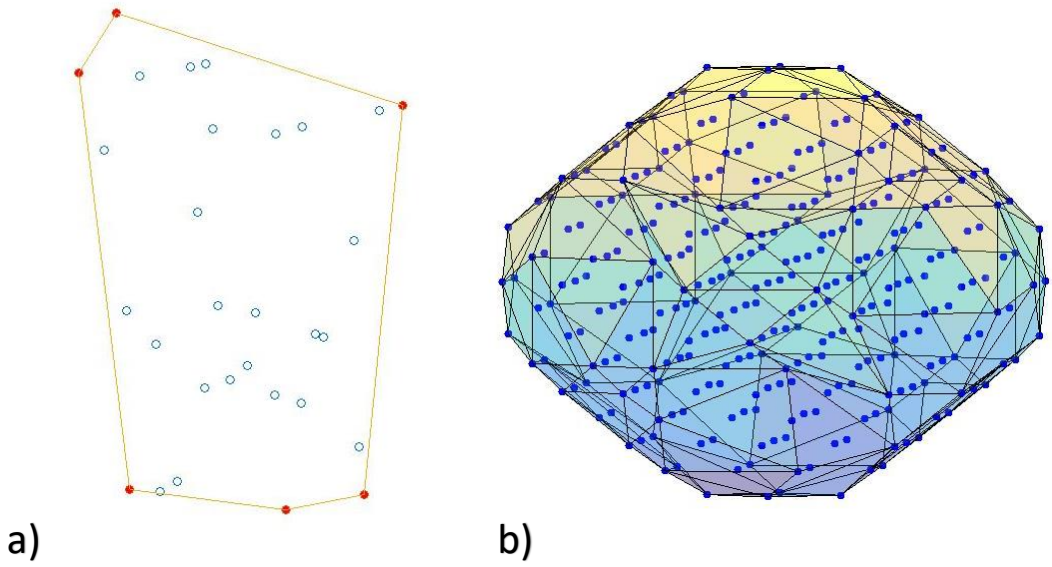

Figure 4.2 a) Simple Diagram showing the convex hull for a set of blue points, the red outline connects the convex hull set. b) 3D representation of the convex hull for a set of lattice points.

The volume of a convex hull is obtained by Delauney triangulation of all points found within the convex hull, and summing up the individual volumes of each triangulation. Applying this method to a crystal lattice is problematic since it does not consider all the volume local to the surface atoms.

4.4.2 Voronoi Cells Method

For every atom a Voronoi cell is constructed that includes the local volume (i.e. the region of space that is closest to each particular atom). This requires an extension of the lattice at the surface, which was implemented using a variation of the *arbitrary passivation code* (see chapter 6), where the likely position of the extra points is calculated.

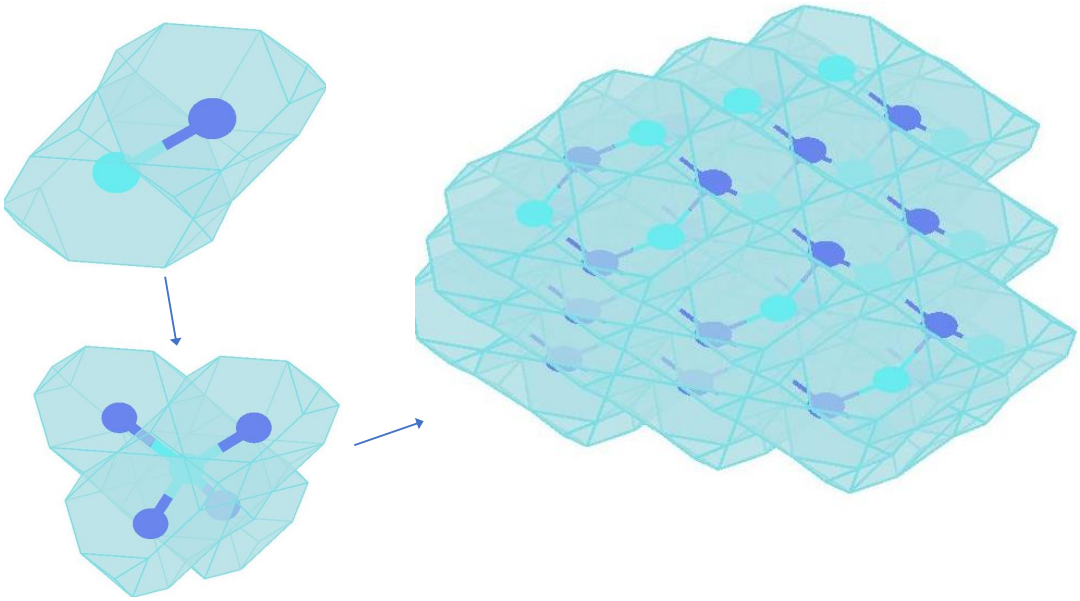

Figure 4.3 Illustration of Voronoi cells built around lattice points.

Initially it was thought that the convex hull for all the verticies of the Voronoi cells would provide the most accurate model to determine the volume. However, this gives

an overestimate due to the additional volume of enclaves between surface Voronoi cells. For an unstrained structure, the sum of all the Voronoi regions is completely equivalent to traditional effective radius calculations. A comparison of alternative measurement methods is shown in figure 4.4.

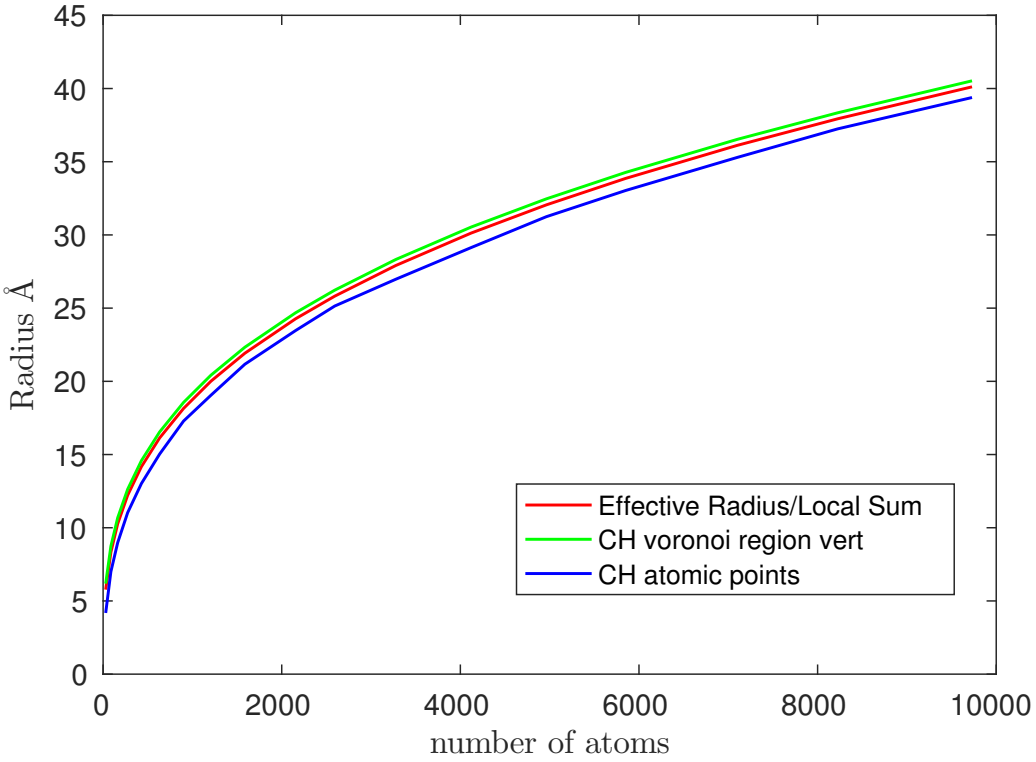

Figure 4.4 Radius as a function of atomic number using four different methods. The effective radius/local sum methods are identical, convex hull of atomic points gives an under estimate, while the convex hull of the Voronoi vertices gives a slight overestimate.

In addition the summation of Voronoi cell volume can also be applies to irregular structures such as tetrapods (shown in figure 4.5). This makes it a more complete general method for determining the volume for arbitrary structures in a way that is consistent with previous models for unstrained structures.

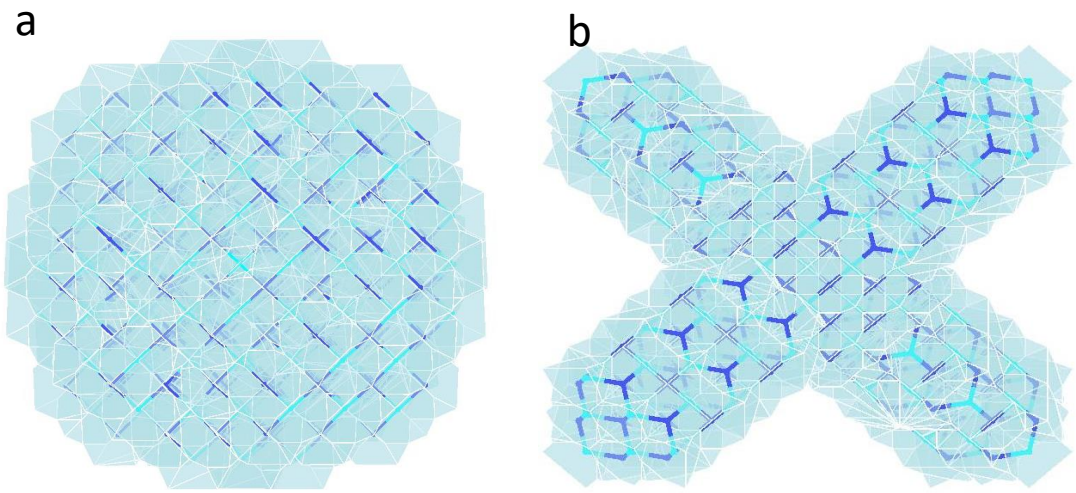

Figure 4.5 The set of voronoi cells are shown for a) strained quantum dot and b) tetrapod. Using this method the volume of any structure can be accurately determined.

4.5 TEM Image Processing

TEM (transmission electron microscopy) is typically used for imaging of quantum dots. An electron beam is transmitted through a sample of quantum dots, which produces an ultra-high resolution image due to the small wavelength of electrons. Using this technique individual atoms within a nanostructure can be imaged. This can be used to provide an estimate of the NC radius. The diameters are often measured from the image, with an average taken for a small batch of structures. This is a process that is often implemented by hand. Increasing the accuracy of these measurements can be achieved using computational algorithms that can automate this process. This makes sure the process is consistent and reproducible. Together with the work on size determination, this could pave the way for better agreement on size between

experimental and theoretical results.

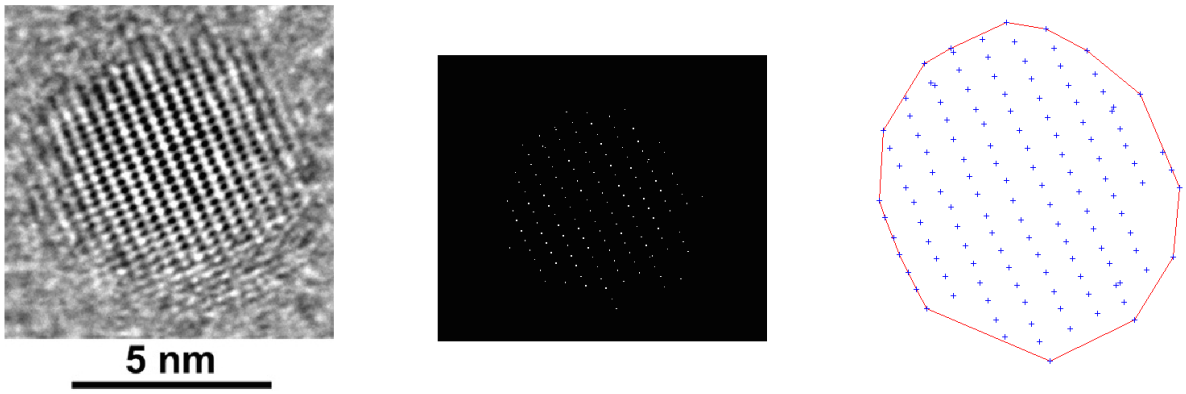

Figure 4.6 A simple image processing algorithm is used to estimate the size of quantum dot using a TEM image. The example shows a CdSe quantum dot with a radius of $5nm$
.

A simple image processing algorithm was written which locates the atomic positions and defines a 2D convex hull. The volume of this can be used to estimate the radius $r = \sqrt{\frac{A}{\pi}}$. After the hue and saturation are removed and the contrast is increased, the image complement is then found. Light clusters of pixels are then defined as atomic positions, which can then be used to define the convex hull. This algorithm can be used on an entire ensemble of dots.

4.6 Input Geometry

The first stage of the SEPM process is to define the input geometry where a set of coordinates are generated within a supercell. This involves a utility code which will generate these coordinates. Several codes were written that provide this type of functionality to generate spherical/cubic rods and dots, core-shell structures, quantum tetrapods and quantum rings for zinc-blende, wurzite and rock-salt semiconductors.

4.7 Conclusions

The major achievement presented within this chapter was the model for size determination of strained structures. This is potentially very useful since it is entirely consistent with the analytical effective radius calculation (i.e., it gives the same results for unstrained structures). In addition this method can be extended to determine the volume of any arbitrary nanostructure such as tetrapods (shown in figure 4.5 b). The empirical strain method is unlikely to be applied since the fitting parameters are not currently available. At present they are fairly arbitrary, however extensive DFT analysis could be used to generate the strain parameters that generate the same strain profile as a DFT calculation. The application of image processing to accurately determine the size of experimental quantum dots would probably require further development if it was to be implemented. However, it currently serves as a proof of concept that could be taken further in future.

Chapter 5

Semi-Empirical Pseudopotential Method

5.1 Introduction

This chapter provides an overview of the theoretical framework required for the semi-empirical pseudopotential method. This begins with a brief overview of atomistic methods, followed by a more detailed account of the history and derivation of pseudopotentials, pseudopotential methods and eigensolvers.

5.2 Many Body Problem Atomistic Methods

The many body Hamiltonian defines the operator corresponding to the total energy of the system

$$H\Psi = E\Psi \tag{5.1}$$

The total energy is made up of two parts: the potential energy and the kinetic energy. Full consideration of the many body system requires consideration of iterations between all the carriers

$$H = \underbrace{\sum_{i=1}^{N} \left(-\frac{\hbar^2}{2m}\nabla_i^2 - Ze^2\frac{1}{|\mathbf{r}_i - \mathbf{r}_j|} \right)}_{\text{kinetic energy}} + \overbrace{\frac{1}{2}\sum_{i=j}\frac{e^2}{|\mathbf{r}_i - \mathbf{r}_j|}}^{\text{potential energy}} \tag{5.2}$$

where $\mathbf{r}_i$ denotes the electron position and $\mathbf{R}$ denotes the nuclei position. This expression is valid for a system of N electrons around just a single nucleus (much simpler than for a crystal).

$$\Psi(\mathbf{r}_1, \mathbf{r}_2, \ldots, \mathbf{r}_N) = \psi(\mathbf{r}_1)\psi_2(\mathbf{r}_2)\ldots\psi_N(\mathbf{r}_N) \tag{5.3}$$

The all electron problem is far too computationally expensive to be solved in any realistic time period. The many body scales *exponentially* with the number of states, due to the sheer complexity of the wave-function (shown in equation 5.3). There is no known algorithm with polynomial scaling to this problem, and it is not expected to arrive any time soon. Therefore, atomistic methods need to apply a series of approximations (such as Bloch functions and pseudopotentials) due to the sheer complexity of the physical system. There are often subtle differences in the way these approximations are applied between differing methods. However, they are usually underpinned by similar physical and mathematical concepts.

5.3 Bloch Functions Modulated by Plane Waves

The symmetry and periodicity of the crystal lattice can be exploited to simplify the problem and reduce computational time. The crystal is a periodically self repeating structure (assuming no strain). Therefore, the wave function is also expected to be a periodical function. Mathematically this wave function can be expressed as a Bloch wave where the function $u(\mathbf{r})$ is a periodic function with the same periodicity of the crystal lattice. In other words the wave function can be expressed as a Bloch function u_k, which is modulated by a plane wave:

$$u(\mathbf{r}) = \frac{1}{\sqrt{\Omega}} \sum_{\mathbf{G}=\mathbf{0}}^{\infty} C_{\mathbf{k}}(\mathbf{G}) e^{i\mathbf{G}\cdot\mathbf{r}} \tag{5.4}$$

Here the Bloch function is expanded into a Fourier series using the reciprocal lattice vector $\mathbf{G}$. This basis is both orthogonal and normalised ($\langle \phi_{\mathbf{G}} | \phi_{\mathbf{G}'} \rangle = 0$). The wave-function $\phi_{\mathbf{k}}$ in this orthonormal basis is

$$\phi_{\mathbf{k}}(\mathbf{r}) = \sum_{\mathbf{G}=\mathbf{0}}^{\infty} C_{\mathbf{k}} \phi_{\mathbf{G}}(\mathbf{r}) e^{i\mathbf{k}\cdot\mathbf{r}}. \tag{5.5}$$

This can be applied to express the wave-functions for particular eigenstates,

$$\psi(r) = \sum_{n}^{N_{\mathrm{B}}} \sum_{\mathbf{k}}^{N_k} c_{n,\mathbf{k}\, u_{n,k}}(\mathbf{r}) e^{\mathbf{k}.\mathbf{r}} \tag{5.6}$$

where $u_{n,k}(x)$ are Bloch wave-functions for a state n and at k-points $\mathbf{k}$.

5.4 Unit Cells and Supercells

The supercell is to quantum dot analysis what the unit cell is to bulk analysis (shown in figures 5.1 and 5.2). For a bulk semiconductor the unit cell is the smallest unit that can be replicated to reproduce the entire crystal structure $\vec{T} = u_1\vec{a}_1 + u_2\vec{a}_2 + u_3\vec{a}_3$.

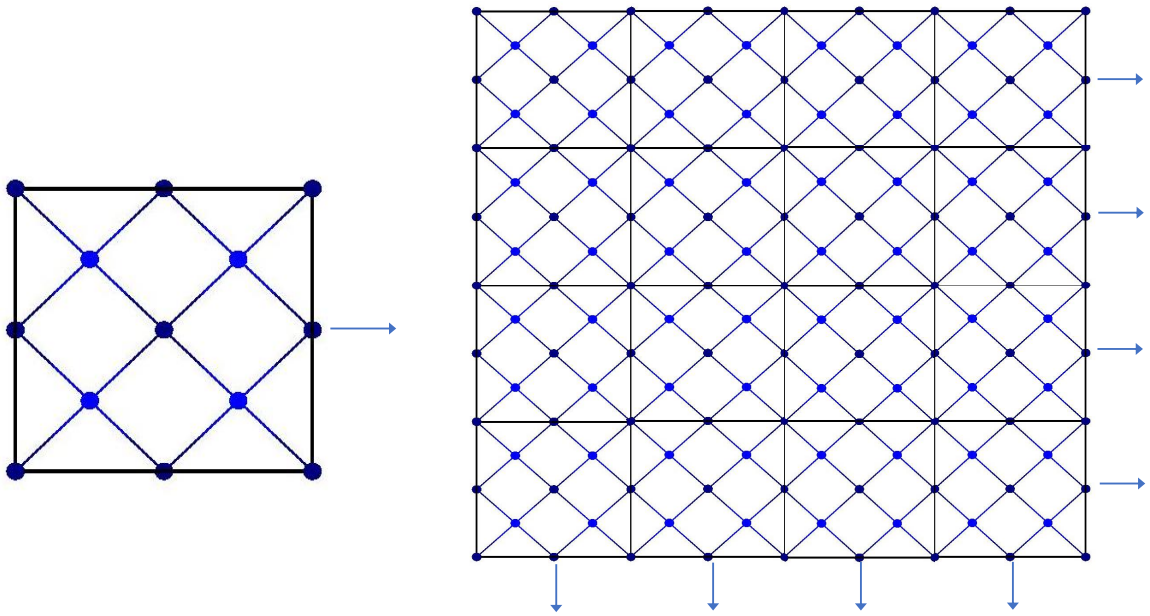

Figure 5.1 Top down view of an 8-atom unit cell, replicated to produce bulk semiconductor material.

This periodicity allows the wave function to be expressed as a Bloch function. For a quantum dot the periodicity comes from the supercell, which is replicated to produce an infinite array of quantum dots separated by a vacuum. The supercell needs to be large enough to avoid interaction effects between neighbouring cells (see figure 5.2), but not too large as this will increase the number of grid points and therefore the computation time.

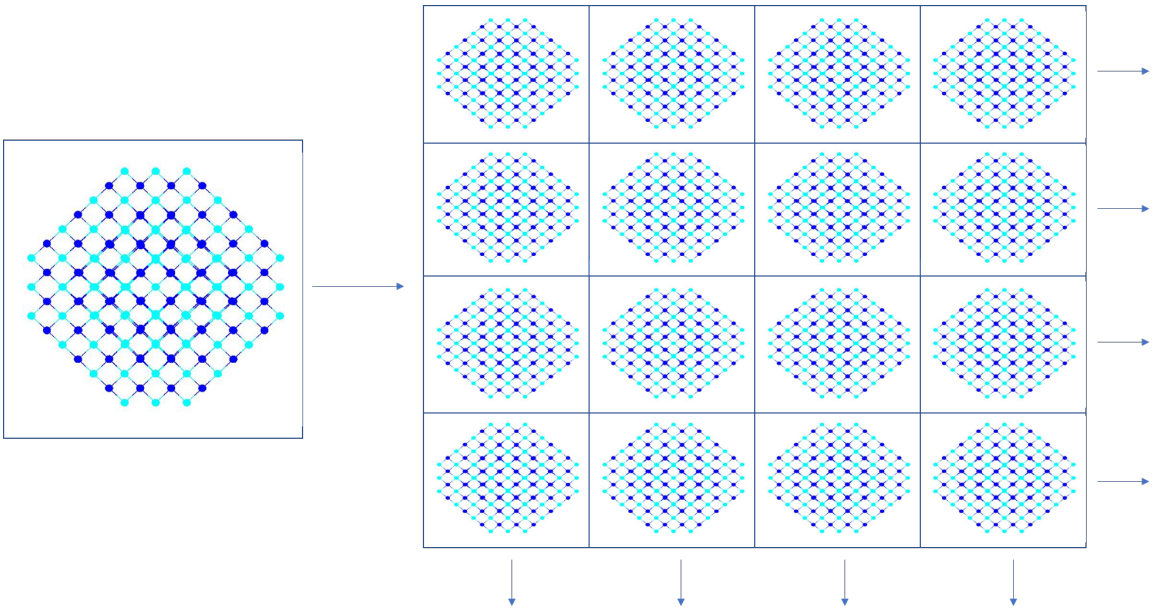

Figure 5.2 Illustration of the replicated supercell to form a super lattice. This is required for plane wave based theoretical calculations. For a bulk calculation the supercell is the unit-cell (shown in figure 5.1).

Typically the vacuum between neighbouring supercells needs to be at least one lattice constant. While this is a relatively well established rule of thumb, the effects were verified by running the same calculation with and increased spacing between neighbouring quantum dots i.e. larger vacuums. As expected, there was negligible difference between the results.

5.5 Pseudopotentials

The configuration of the outer shell or valence electrons determines the chemistry of the atom, describing how these atoms react with one-another to form crystalline solids. This idea forms the foundation of the *frozen core* approximation, which assumes that core electrons are unperturbed by external forces and therefore the Schrödinger equation for the system can be solved for just the valence electrons.

Pseudopotentials provide an approximation to the many-body behaviour of electrons that orbit atoms, reducing their complexity to a level where solutions are computationally realistic. The pseudopotential of a system can be expressed as a Fourier series

$$V(\mathbf{r}) = \sum_{\mathbf{K}} V(\mathbf{K}) e^{i\mathbf{K}\cdot\mathbf{r}} \tag{5.7}$$

$$V(\mathbf{K}) = \sqrt{\Omega} \int d^3 r V(\mathbf{r}) e^{-i\mathbf{K}\cdot\mathbf{r}} \tag{5.8}$$

This allows the wave-function to be solved in a periodic system of plane waves. When solving a system of quantum dots, a supercell is used instead of a unit cell as the basis for a periodic function. The formulation of pseudopotentials was initially drawn out by Phillips and Kleinman [108], whose work set the foundations of the methodology used today.

5.6 Empirical Pseudo-potentials

A basic empirical pseudo-potential code was written to help understand methods. This involved following a similar specification to the methodology outlined in most text books on quantum electronics [109]. To begin with the pseudopotential is written as a Fourier series (shown in equation 5.7). The contribution of pseudopotentials for every atom in the unit cell needs to be considered. The diamond lattice of silicon and germanium has 2 atoms within its primitive unit cell. For any structure with more than one atom per unit cell (i.e. anything except simple cubic) we need to define a structure factor

$$S_{\mathbf{K}} = \frac{1}{N}\sum_{i=1}^{N} e^{i\mathbf{K}\cdot\mathbf{r_i}}, \tag{5.9}$$

which is a summation for all N atoms within the unit cell, where the atoms are located at positions $\mathbf{r}_i$. This leads to a modification of the pseudopotential shown in equation 5.7 where the coefficients are corrected by the structure factor as $V_{\mathbf{K}} \rightarrow V_{\mathbf{K}} S_{\mathbf{K}}$. Atoms are located at positions $\mathbf{r}_1 = \frac{a_0}{8}(1,1,1) = \mathbf{x}$ and $\mathbf{r}_2 = -\frac{a_0}{8}(1,1,1) = -\mathbf{x}$. Therefore the complete structure factor can be written as:

$$S_{\mathbf{K}} = \frac{1}{2}\left(\exp(-i\mathbf{K}\cdot\mathbf{x}) + ...\mathbf{K}\cdot\mathbf{x})\right) = \cos(\mathbf{K}\cdot\mathbf{x}), \tag{5.10}$$

Only the first few reciprocal lattice vectors need to be used since $V_{\mathbf{K}}$ decreases rapidly with increased reciprocal lattice vectors. The k-vectors are given by $\mathbf{K}_0 = (0,0,0)$, $\mathbf{K}_3 = (1,1,1)$, $\mathbf{K}_4 = (2,0,0)$, $\mathbf{K}_8 = (2,2,0)$ and all cyclic permutations of these reciprocal lattice vectors.

The form factors for silicon and germanium are shown in the table below.

Form Factor	Si	Ge
V_3	-0.2241	-0.2768
V_8	0.0551	0.0582
V_{11}	0.0724	0.0152

Using this method it is possible to derive the band-structure shown in figure 5.3

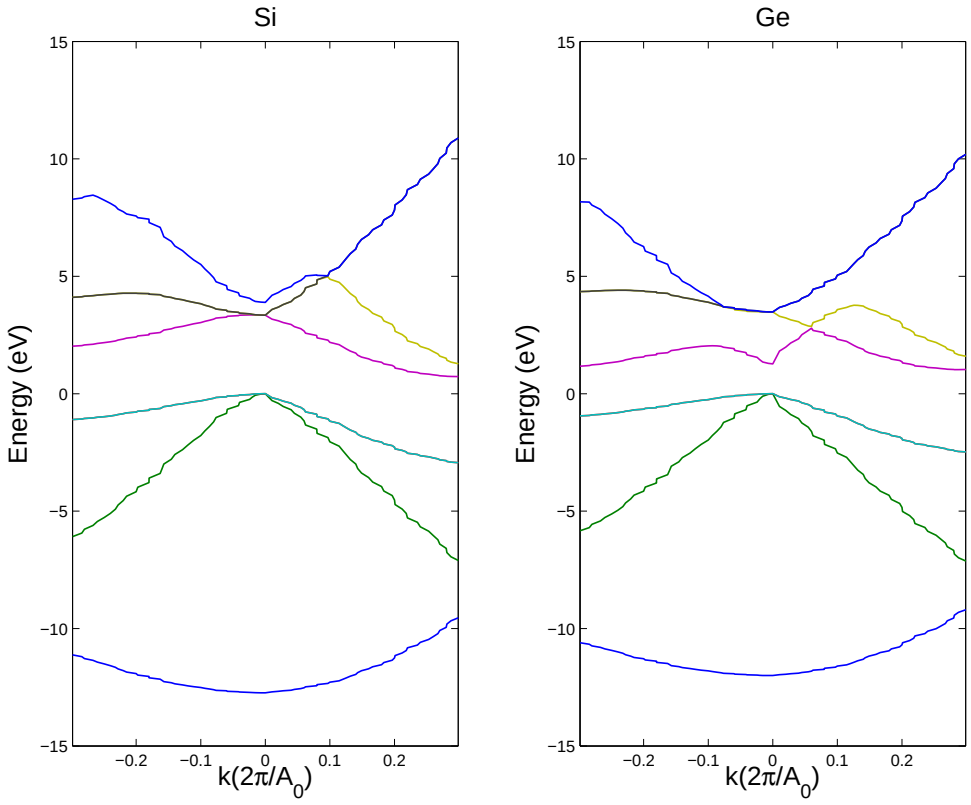

Figure 5.3 Bandstructure for Silicon and Germanium calculated using a basic empirical pseudopotential method. The lattice constant is given by A_0.

5.6.1 Local-Density-derived Semi-Empirical Pseudopotentials

Density Functional Theory (DFT) is one of the most widely used ab-initio methods to determine the physical characteristics of many-electron system by computation of the ground state. The ground state is related to the electron density by the Kohn-Sham equations. This framework provides the means to reduce the many-body problem of N electrons with 3N spatial coordinates to a set of three spatial coordinates. This is achieved by using a functional of the electron density

$$V_{\mathrm{KS}}(\mathbf{r}) = \int \mathrm{d}\mathbf{r}' \frac{n(\mathbf{r})}{|\mathbf{r} - \mathbf{r}'|} + V_{\mathrm{xc}}(\mathbf{r}) + V_{\mathrm{ext}}(\mathbf{r}), \tag{5.11}$$

where V_{xc} is the exchange-correlation energy and V_{ext} is the external potential, for more details see Gross *et al.* [110] and references therein.

Empirical pseudopotentials are typically fitted to reproduce physical observables of the bulk, such as electronic energies and the bulk band-gap. However, they are not very good at reproducing wave-functions. This problem gave rise to the semi-empirical pseudopotential method, where the semiempirical pseudopotentials were partially derived from Local-density approximations (LDA) for bulk semiconductors:

$$\left(-\frac{1}{2}\nabla^2 + v_{KS}(\mathbf{r}) \right) \psi_i(\mathbf{r}) = \epsilon_i \psi_i(\mathbf{r}), \tag{5.12}$$

This involves using a DFT code, which uses standard norm-conserving nonlocal pseudopotentials [111]. Historically ABINIT has been the most widely used code to generate semi-empirical pseudopotentials, so its use is recommended, in order to ensure consistency.

In eq. 5.12 the Kohn-Sham potential $v_{KS}(\mathbf{r})$ is the superposition of local pseudopotentials, the non-local pseudopotentials and the electron-electron interaction:

$$v_{KS}(\mathbf{r}) = v_{local}(\mathbf{r}) + v_{nonlocal}(\mathbf{r}) + v_{xc}(\mathbf{r}). \tag{5.13}$$

The potential $V_{LDA}(r)$ is a periodic function and can be expanded in a Fourier series, which means it can be used in a plane-wave based calculation following a similar type of methodology implemented for EMP methods. The Kohn Sham equation in reciprocal space is

$$V_{LDA}(\mathbf{G}) = \int_{\Omega} d^3 r V_r(\mathbf{r}) e^{i\mathbf{G}\cdot\mathbf{r}}, \tag{5.14}$$

where the set of the reciprocal lattice vectors is given by $\mathbf{G}$ and the volume of the unit-cell is given by Ω. The values calculated at discrete $\mathbf{G}$-vectors are taken and then fitted with a spline (or other fitting technique). The pseudopotentials are fitted such that the bulk band-gap is reproduced. The exact details of this are very complicated and were not part of this work, however Bester *et al.* [112] and references therein is a good source for a more complete explanation of this fitting procedure.

5.7 Atomic Position Generation

The first stage is to use a suitable atomic position generation code which writes an output file with the supercell vectors, the normalised positions and the atomic potentials for every atom in the structure. This should also include the passivants at their respective positions with their potentials included. For more on this stage refer to sections on passivation and crystal structure. If the structure (not including passivants) contains more than 2 atom types (eg. core/shell or alloy structure), then extra information regarding the percentage of atoms each atom is bonded to is required. Several codes were written that provide this type of functionality, including the ability to generate complex structures such as pyramids (figure 5.2), ring and tetrapods 5.4.

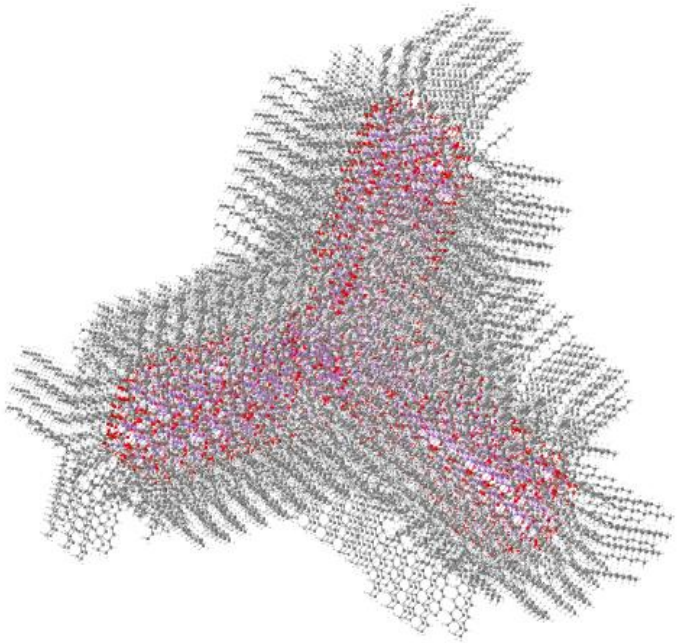

Figure 5.4 A tetrapod passivated using atomic ligands.

5.8 Generating the Crystal Potential

The local part of the potential energy shown in equation 5.2 is generated with the atomistic detail of the structure. This is implemented using a parallel code called GENPOT (GENerate POTential) where the superposition of the local potentials is computed in the form of scalar volumetric data. Once the positions files have been generated, with the locations of all the atomic potentials, the effective crystal pseudo potential can be generated on a grid defined by the supercell dimensions, according to

$$V_{\mathrm{loc}}^{\mathrm{SEPM}}(\mathbf{r}) = \sum_{\alpha,j,n} v_{\alpha}\left(\mathbf{r} - \mathbf{R_n} - \mathbf{r}_{\alpha j}\right), \tag{5.15}$$

where $V_{\text{loc}}^{\text{SEPM}}(\mathbf{r})$ represents the total crystal potential as a function of position ($vecr$, and v represents the atomic potentials. The atom type is denoted by α and j denotes the atomic index. A full GENPOT code was written in MATLAB, which outputs suitable files to be used with PESCAN (see figure 5.6). There was a plan to write a MATLAB eigensolver also. However, this turned out to be far more complicated than anticipated.

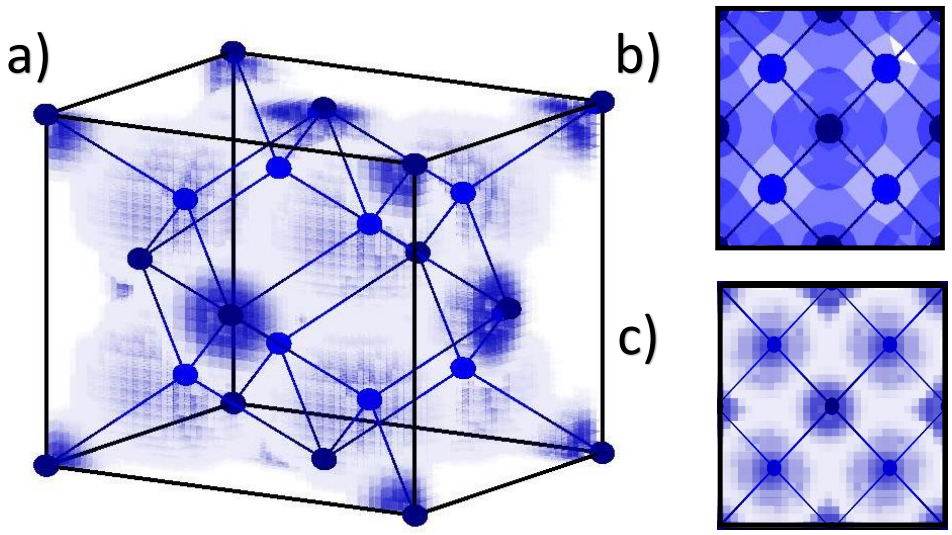

Figure 5.5 InSb potential within an 8 atom unit cell a) volume rendered isometric, b) top down isosurface c) top down volume rendered

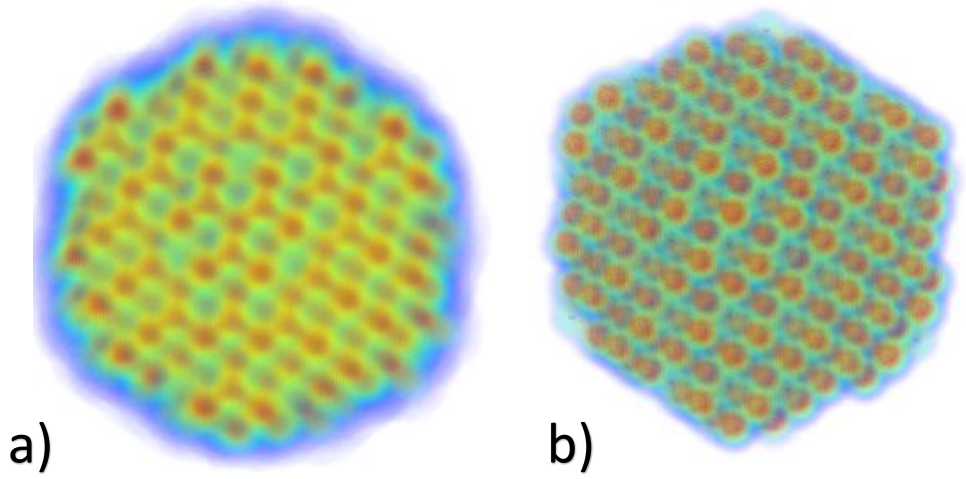

Figure 5.6 The total crystal potential for an InSb quantum with passivation (a) and without passivation (b).

5.9 Single particle Schrödinger Equation

A parallel implementation of an eigensolver for pseudopotential calculations is necessary in order to solve large quantum systems in a relatively short time frame. Parallel Energy Scan (PESCAN) [94,113] is a parallel eigensolver for non self-consistent semi-empirical pseudopotential-based electronic structure calculations and was the primary eigensolver used in this thesis. In this method the single-particle Schrödinger equation is given by:

$$\left(-\frac{\hbar^2}{2m_0}\nabla^2 + V_{loc}^{SEPM}(\mathbf{r}) + \hat{V}_{nloc} + \hat{V}_{so} \right)\psi_i(\mathbf{r}) = \epsilon_i \psi_i(\mathbf{r}) \tag{5.16}$$

where V_{loc}^{SEPM} is the superposition of the local pseudopotentials (shown in equation 5.15) and $\hat{V}_{nl}$ and $\hat{V}_{sp}$ are short range operators that account for the non-local ad spin orbit potentials respectively. The single electron/hole wave function is represented by

a plane wave basis set where a cut-off energy is defined to restrict the number of plane waves, allowing convergence of the system. A standard 3D FFT is used to transform the local potential from real space to reciprocal space (note that the output of the total crystal potential is in real-space despite the fact that the local pseudopotentials are derived in reciprocal space). There is an option to include non-local pseudopotentials in the Hamiltonian, and spin-orbit interactions are also included.

5.10 Folded Spectrum Method (FSM)

Unlike in *ab-initio* approaches such as DFT, the goal here is not to obtain a complete set of states deep into each band. The method is more about the ability to obtain a few states of interest around the band-gap (interior eigenstates), which give enough information to calculate exciton energies. This is possible thanks to a process known as the folded spectrum method originally conceived by Zunger's group [93], where the spectrum ε_i is folded about a reference energy ε_{ref} according to:

$$\left(\widehat{H} - \varepsilon_{ref}\right)^2 \psi_i = \left(\varepsilon_i - \varepsilon_{ref}\right)^2 \psi_i \tag{5.17}$$

$$\left(-\frac{\hbar^2}{2m_0}\nabla^2 + V_{loc}^{SEPM}(\mathbf{r}) + \hat{V}_{nloc} + \hat{V}_{so} - \varepsilon_{ref} \right)\psi_i(\mathbf{r}) = \left(\varepsilon_i - \varepsilon_{ref}\right)^2 \psi_i). \tag{5.18}$$

The reference energy is an input parameter: a specified number of states are returned that have energies closest to its value. In order to obtain VB states, the reference energy should be just above the HOMO, while CB states are obtained by setting ε_{ref} just below the LUMO. However, if these energies are too close then the values may

not fully converge within a reasonable number of iterations. By default the code uses a standard conjugate gradient algorithm. However, it is possible to use a Davidson algorithm [114], or a LOPCG (Locally Optimal Preconditioned Conjugate Gradient) algorithm [115], if the user has a specific type of problem that runs more efficiently using one of these methods. On completion of this process, the desired energies and wave-functions for the single electron states are given as outputs

$$\psi_i(\mathbf{r}) = \sum_{\mathbf{G}} c_i(\mathbf{G}) e^{\mathbf{G}.\mathbf{r}}.. \tag{5.19}$$

All the wave-function data is stored in one compressed binary file. This requires expansion to generate the wave-functions (shown in equation 5.19) or charge distributions for each individual energy level

5.11 Optical Properties

Excitonic effects need to be accounted for in order to predict the optical properties of semiconductor nanocrystals. A simple interpretation could simply use the energy difference between single particle states to estimate the energy required to excite an electron from one state to another. This does not consider the Coulomb interaction between the two carriers nor does it consider the probability associated with the transition (indicating whether the transition is bright or dark). In order to obtain a complete model of the optical properties, the excitonic wave functions need to be determined by calculating the Coulomb exchange integrals [116], and finally the dipole matrix elements are computed [116,117]. This is similar to the type of analysis implemented to determine the densities of exciton and bi-exciton states discussed earlier on. However, here the full atomistic single particle wave functions are used.

5.11.1 Expansion of Single Particle Wave-functions

A many-body expansion of the single particle wave functions is implemented in terms of single-substitution Slater determinants

$$M^{(a)} = \sum_{v,c} A^{a}_{v,c} \langle \psi_v \left| r \right| \psi_c \rangle. \tag{5.20}$$

The Slater determinant describes the wave function of a two carrier system, including both the symmetry requirements and the Pauli exclusion. This provides a set of exciton states with contributions from single particle states.

5.11.2 Screening Electron-Hole Coulomb Interaction

For bulk semiconductors a simple dielectric constant describes the screening in the electron-hole Coulomb interaction. However, for nanocrystals position-dependent screening (ε) and Coulomb potential v are required to describe many body interactions

$$v\left(r_e, r_n\right) = e^2 \int \varepsilon^{-1}\left(r_e, r\right) \left| r - r_h \right|^{-1} dr \tag{5.21}$$

The single particle wave functions are then used to form a set of Slater determinants. In this expansion, it is important to specify the number of electron and hole states used. The output provides a set of exciton states that are formed through contributions from single particle states.

5.12 Excitonic Wave Functions

The excitionic wave functions for a pair of eigenstates ψ_v and ψ_c are calculated by solving the Coulomb direct integrals

$$J_{vc,v'c'} = e^2 \sum_{\sigma_1,\sigma_2} \int\int \frac{\psi^*_{v'}(\mathrm{r}_1,\sigma_1)\psi^*_c(\mathrm{r}_2,\sigma_2)\psi_{c'}(\mathrm{r}_1,\sigma_1)\psi_v(\mathrm{r}_2,\sigma_2)d\mathrm{r}_1 d\mathrm{r}_2,}{\varepsilon(\mathrm{r}_1,\mathrm{r}_2)|\mathrm{r}_1-\mathrm{r}_2)|} \tag{5.22}$$

and exchange integrals [116]

$$K_{vc,v'c'} = e^2 \sum_{\sigma_1,\sigma_2} \int\int \frac{\psi^*_{v'}(\mathrm{r}_1,\sigma_1)\psi^*_c(\mathrm{r}_2,\sigma_2)\psi_{c'}(\mathrm{r}_1,\sigma_1)\psi_v(\mathrm{r}_2,\sigma_2)d\mathrm{r}_1 d\mathrm{r}_2,}{\varepsilon(\mathrm{r}_1,\mathrm{r}_2)|\mathrm{r}_1-\mathrm{r}_2)|,} \tag{5.23}$$

including the single-particle wave functions for both conduction (ψ_c) and valence (ψ_v) band, which depend on both position (r) and spin (σ). These can then be used to determine the excitionic energies, complete with the Coulomb interaction. This calculation is the major bottleneck in terms of computational time.

Chapter 6

Passivation & Surface Analysis

6.1 Introduction

The main goal of this chapter was to design a general passivation routine to be used within the semi-empirical pseudopotential method. This was to provide the necessary framework to passivate semiconductors such as InSb, GaAs and GaSb. The longer term goal was to develop a general method that could be used to passivate any semiconductor by means of pseudo atoms (or some other passivation method). The idea was that for every surface there exists an ideal passivation. However, there are many questions that need to be asked insofar as what constitutes an ideal passivation, which will be discussed in this chapter.

6.2 Surface States

Surface states are quantum states that tend to localise around individual surface atoms. The main source of surface states can be attributed to unpassivated or poorly passivated dangling bonds. However they may also be caused by surface features

(voids/facets) and the surface composition (stoichiometry). Trap states are difficult to avoid in colloidal structures because every dangling bond needs to be capped by a ligand and only a single uncapped dangling bond is required for a trap state. Furthermore, peculiar surface features, such as atoms with 3 dangling bonds may be more difficult to passivate due to the geometry of the surface and the positioning of the atomic ligands. Surface states often have energies within the band gap. These may have a detrimental effect on physical properties of the NC, including a reduced transfer rate of photo-generated charge carriers, reduced optical absorption, reduced quantum efficiency, and reduced luminescence [118]. Electrochemical effects caused by trap states at the surface can reduce the conductivity of the structure, where electrons and holes can be trapped and have reducing or oxidising behaviour [119]. Surface states cannot just be ignored in theoretical calculations since the surface represents a large portion of the nanocrystal. The surface structure and surface orientation play a big role in determining the electronic and optical properties of semiconductor quantum dots. Typically, theoretical models work towards isolating core states and pay little attention to surface effects. However, in recent years surface analysis has been gaining more attention [120–123], due to an increased need to explain experimental data on surface effects. Firstly the surface-to-volume ratio of quantum dots increases very quickly with decreasing quantum dot size. The surface to volume ratio (in terms of numbers of atoms) is an important parameter to consider when dealing with passivation, because it gives a rough idea of how much of the charge distribution is expected to reside around surface atoms. For example, a small quantum dot, with fewer than a thousand atoms, will have a very high surface to volume ratio, as shown in figure 6.1. Therefore we expect a higher fraction of the total charge distribution to be located around the surface.

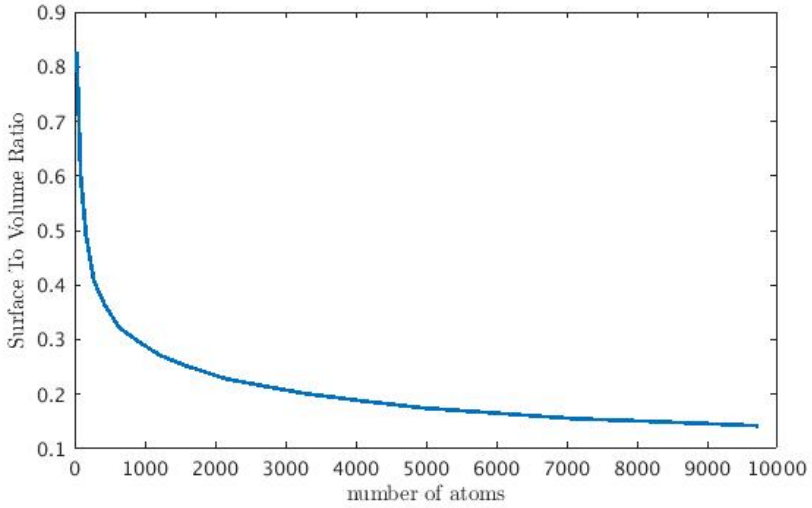

Figure 6.1 The surface to volume ratio of zincblende quantum dots. This quantity is a useful tool in defining how good a passivation is for a structure of a given size.

6.3 Organic Ligands

Organic ligands are used as capping agents in the colloidal synthesis process. There are a wide range of ligands used in the fabrication of quantum dots for device applications. These include alkylthiols [124, 125], aromatic thiols [126], alky- lamines [127], mercaptocarboxylic acids [128] and atomic ligands [129]. In figure 6.10 a spherical GaAs quantum dot a with $10\mathring{A}$ radius passivated with oleic acid is shown. Simulation of organic ligands is far more complicated than simulation of a crystal. First, reliable pseudopotentials do not exist for the atoms in these structures, and would therefore need to be derived. Also, ligands are not static: their long chains of atoms have many degrees of freedom and move around relative to one another. The effects of this dynamics cannot be overlooked as they have an impact on how carriers are distributed across the surface. Therefore, we can conclude that accurate simulation of the atomic ligands is going to be very difficult and may require more advanced

(and computationally expensive) models. In terms of generating photo-current in a quantum dot solar cell device, the passivation can act as a partial insulator reducing conduction of charge, therefore it is important to select a passivant that does not prohibit the generation of photo-current.

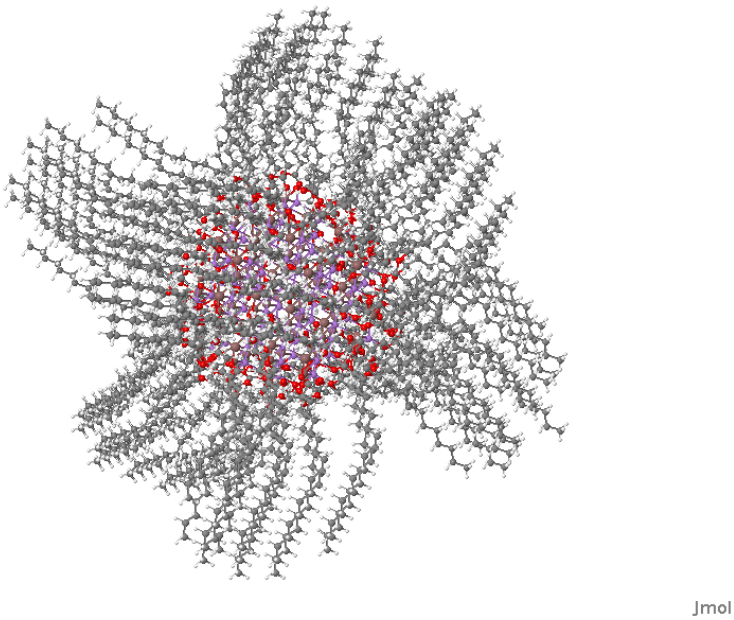

Figure 6.2 Small quantum dot passivated with oleic acid.

Attempts were made to passivate a structure using organic ligand molecules. Unfortunately, accurate pseudopotentials are not available. Several rough estimations were tried. However, none of them produced spectra without trap states in the gap.

6.4 High Bandgap Material Passivation

In this passivation method the supercell is filled with a high band-gap material (larger than the band-gap of the quantum dot) [130, 131]. This is essentially similar to simulating a StranskiKrastanov (SK) quantum dot, which may differ from the colloidal

variety. Also the complexity of the calculation will increase due to the increased number of atoms and the need to use a different surrounding material for the VB and the CB. The most common method of passivation is to use a Gaussian pseudo-atom (see next section).

6.5 Gaussian Potential Passivation

Gaussian Potential Passivation is the standard approach when applying the SEPM. Short range spherically symmetric ($V(\mathbf{r}) = V(|\mathbf{r}|)$) Gaussian electrostatic potentials

$$V(r) = \alpha e^{-(|r-R_p|/\sigma)^2} \tag{6.1}$$

are placed close to the surface atoms to cap the dangling bonds.

These capping potentials are used to generate a total crystal potential that contributes to the local part of the Hamiltonian, which is then solved using an eigensolver. The parameters of this passivation agent are the Gaussian width (σ), height (α) together with the distance from the surface (R_p). The dangling bong angle is usually consistent with the lattice. This gives 3 parameters per bond type. Typically there are 4 types of bond, namely anions and cations for one and two dangling bonds respectively. This gives a 12-dimensional parameter space for a set of passivants. This can be simplified by using the same passivation for anions and cations for both one and two dangling bonds.

Initially scientists would find a set of passivation parameters by manual trial and error. Passivation parameters were tested by computing the eigenvalues and eigenvectors and seeing if they were in agreement with the criteria of a good passivation. New parameters were selected and tested using a combination of personal intuition and

experience in the methodology. This is not only very time consuming, but it is also difficult to predict how long the task will take. Therefore it is difficult to allocate time resources to this task, and in the end there is no guarantee that a suitable passivation will be found. To overcome the problem of manual trial and error, algorithms were devised that would sample the parameter space in an efficient manner. One way to reduce the sampling space is to decide on a minimum step size (shown in figure 6.3) which relates to the resolution of the grid. This criterion has never been mentioned in the literature so far.

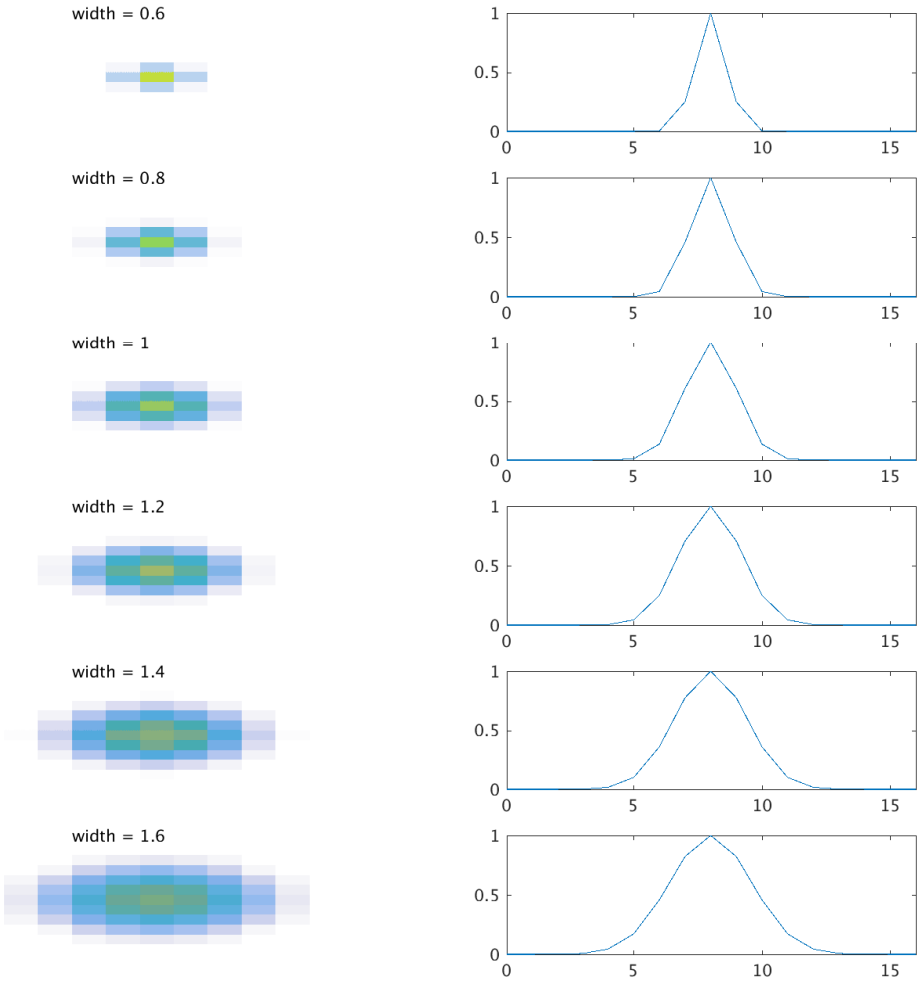

Figure 6.3 3D (left column) and 2D (right column) representations of Gaussian passivation parameters. The resolution of the grid is low ($16n \times 16n$ per unit cell. This means that the minimum step size does not need to be any smaller than $\Delta W/2$, where W is the separation of grid points, and n is the number of grid points per lattice constant.)

A brute force approach that tries and tests the entire search domain has no way to carefully select the next passivation parameter, as it will just cycle through a predetermined domain. This can be time consuming with a 12 dimensional parameter

space producing terabytes of data when performing an exhaustive search.

This procedure allows a subset of passivation parameters to be selected without a fully exhaustive domain search. The most widely used sampling algorithm was devised by Graf *et al.* [132] who used the global optimisation scheme DIRECT (abbreviation of DIviding RECTangles). Each successive sampled passivation parameter set gives more information which is used to decide where to search next.

The quality of the passivation is tested by solving the Schrödinger equation, and evaluating the extent of confinement for the band edge states. This is implemented using a simple volumetric integration, which treats the structure as a perfect sphere and determines the percentage of the total charge that is localised within the core.

6.5.1 Limitations of Search Algorithms

Limitations to simple spherical integration are: (i) it assumes the dot to be perfectly spherical; (ii) it does not show which bonds are poorly passivated. For anions and cations with differing numbers of dangling bonds it provides specific information as to which of the parameters require tuning, meaning individual parameters can be tuned to get a suitable passivation within fewer iterations. This is an improvement since more information about the passivation is given, meaning smarter decisions can be made when searching a space of possible parameters.

6.6 Arbitrary Passivation Code

Pseudo atoms are usually added to the NC structure during the atomic-position-generation process. However there are several situations when a passivation needs to be added to an NC surface afterwards:

i. If a structure has undergone relaxation by VFF or other method. The pseudo atoms need to be added to the surface relative to the new positions of the NC surface.

ii. If the structure of the NC needs to be modified manually, by adding or removing atoms that did not look realistic experimentally (i.e., protruding from an otherwise flat facet). The passivation needs to be run separately in this case.

iii. If full atomic ligands are added to the surface, either as a full passivation or for calculations of the rates of electron/hole transfer to molecular acceptors on the surface. For example, it might be necessary to add the acceptors first, then passivate the rest of the NC surface. For calculations of hole de-localisation effects in the presence of specific organic linkers. In these cases the photoluminescence (PL) energy shifts, and charge density plots are useful analytical tools to shed some light on experimental findings [133–136].

The basic functionality of this code is to add pseudo atoms to an unpassivated surface. This works by reading in the atomic position file and determining the surface atoms by counting the nearest neighbours: All atoms with fewer that 4 nearest neighbours are surface atoms. The positions of the passivants is found using geometric methods on the nearest neighbours. A similar code was used to define the local regions around each atom, which is necessary to define both the size of a strained structure (chapter 4) and the local surface charge (later in this Chapter). Passivation with atomic ligands is implemented by defining a set of vectors for the ligand direction (from the surface), and rotating and shifting a set of points, which define the ligand, to the position and direction of that vector.

6.7 Pseudo-Hydrogen Based Methods

Hydrogen has been used in DFT to passivate the surface of group 4 semiconductors such as silicon [137] and germanium [138]. Each dangling bond has exactly one electron that can pair with the hydrogen to form a stable covalent bond. However, this is not the case for binary materials such as III-V and IV-VI semiconductors. Unfortunately, the construction of hydrogen pseudopotentials is very difficult. Unlike other atoms, there are no core electrons for hydrogen. Also, the H atom is the smallest atom, so it's movement requires a special treatment to take into account the relativistic effects, which depend on the material and surface orientation. [139]. Pseudohydrogen is a simple fictitious atom, with properties that are based on real hydrogen. However, the potential is scaled in line with the ideal fractional charge required to fully saturate the dangling bonds (shown in figure 6.4). Pseudo-hydrogen passivation has been applied extensively by Jingbo Li's group [137,140,141], within the charge patching and DFT methods. However, despite its success, it is not currently a wide-spread strategy in semi-empirical pseudopotential simulations.

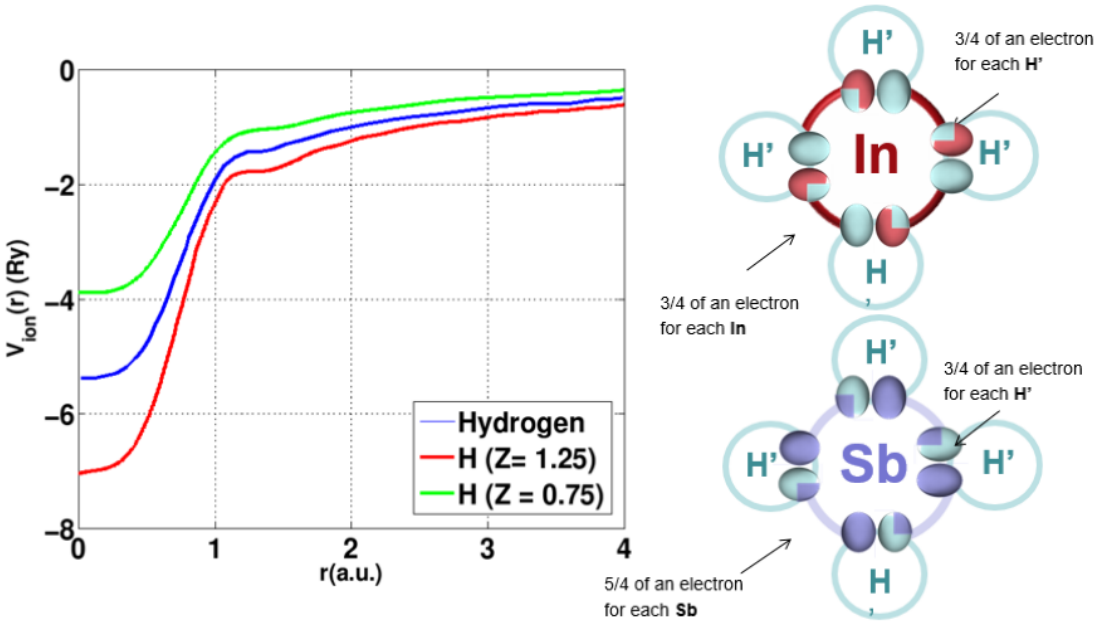

Figure 6.4 The spherically symmetric pseudopotential for hydrogen (blue), pseudo-hydrogen 0.75 fractional charge (green) and pseudo-hydrogen 1.25 fractional charge (red) - right section. The left section illustrates how pseudo-hydrogen fully saturates the covalent bonds using In and Sb as an example.

These pseudo-hydrogenic ionic potentials were used in (5.17) as local potentials in real-space, using bond lengths found by relaxation in the DFT code SIESTA. Unfortunately, this lead to the appearance of many states in the gap. There were also several potential output files that come from using the fractional charge utility within SIESTA, some of these were also tried, but failed to produce suitable results.

A reliable methodology that facilitates the derivation of passivation parameters from local density calculations would perhaps be the most ideal method of passivation. This would mean that passivation parameters for any semiconductor could be obtained based on the LDA pseudopotentials. A passivation method was presented for GaN [142]. In this method pseudo-atom characteristics were derived in real-space, by calculating the difference between a hydrogen passivated DFT grid and an

unpassivated SEPM total crystal potential grid. The spherical potential was then interpolated and fitted to a Yukawa potential and successfully applied to passivate GaN nanowires.

6.8 Surface Charge Analysis

The surface charge analysis code (SURCA) was designed to determine the quality of individual passivation parameters by measuring the percentage of the charge distribution that resides around surface atoms. The code works as a standalone unit so is not restricted to analysis of passivants.

6.8.1 Grid Matching

Charge distribution data is represented as scalar volumetric data on a grid. The grid size is determined by the product of the supercell size (in lattice constants) and the number of Fourier grid points per lattice constant used in the pseudopotential fitting. The atomic position data needs to be scaled such that it matches the grid data. This was verified by running test calculations on a single atom. This showed that the atomic position was rounded to the nearest Fourier grid point.

6.8.2 Local Atomic Region

The local region is defined as the volume contained within the Voronoi cell around an atom. This is the region of space that is closer to a particular atom than to any other atom. The Voronoi cell (show in figure 6.5), or Voronoi region, R_k , associated with the site P_k is the set of all points in X_X whose distance to P_k is not greater than their distance to the other sites P_j , where j is any index different from kk . In other

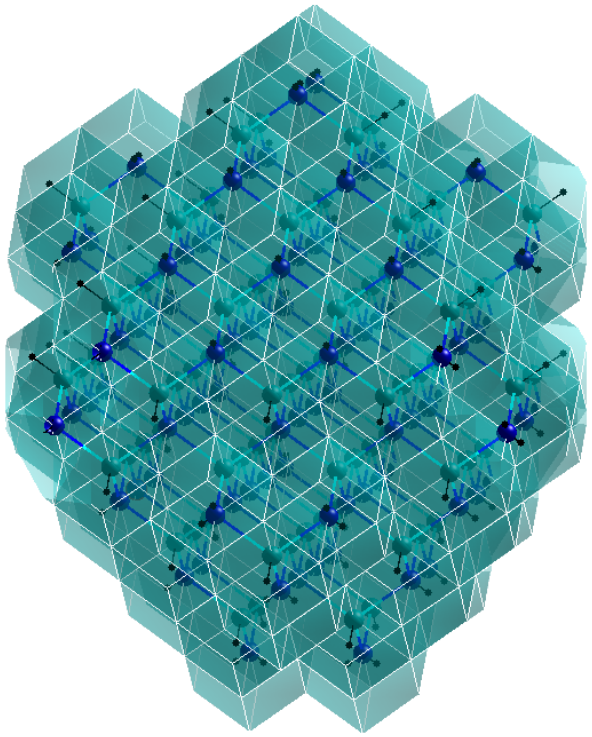

Figure 6.5 The Voronoi regions (transparent cyan) on-top of a small quantum dot.

words, $R_k = \{x \in X \mid d(x, P_k) \leq d(x, P_j) \text{ for all } j \neq k\}$. The Voronoi method is also applied in the decomposition of k-space. This is similar to the Wigner-Seitz cell

(see figure 6.6), which, however, is defined for a lattice and not for all atomic points. The local region considers the lattice and the basis of the crystal, basically all atomic sites.

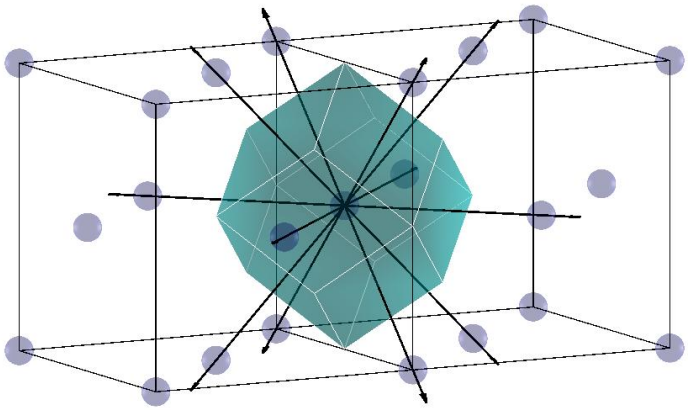

Figure 6.6 The Wigner-Seitz unit cell for zincblende. It is important to note that this is not the same as what has been defined as the local region, since in the latter the atomic positions are made up of two interlocking fcc structures for the anions and cations, while the Wigner-Seitz is just for a single fcc (or other) crystal structure.

The surface atoms of different types are identified by counting the nearest neighbours of all the atoms. A pairwise distance matrix is then computed between the atomic positions and the grid points. Each grid-point is assigned to the closest atomic position. A fictitious shell is generated in order to properly define the local regions for the surface atoms. Once the Voronoi regions of the surface atoms have been defined, the total charge local to each type of surface atom is computed by summing

the weights of all local grid-points.

6.8.3 Percentage Surface Charge

Defining the amount of charge that resides within each unique atomic region provides the framework to decouple the core charge density from the surface charge density. The surface charge density is a good indicator on how well a structure is passivated.

A Voronoi region is defined around every surface atom (shown in figure 6.7). This requires extra points to be generated outside the surface, using a similar procedure to the arbitrary passivation code. This will prevent spectral weight residing in the vacuum being assigned to surface atoms. The next stage is to generate a pairwise distance matrix of atoms and grid points. The spectral weight at each grid point is then assigned to that atom, and is the local charge density around that atom. The sum of the surface charge $\Sigma Q_{surface}(r)$ can be found and expressed as a percentage α by dividing by the total charge $\Sigma Q_{total}(r)$ according to

$$\alpha = 100 \times \frac{\Sigma Q_{surface}(r)}{\Sigma Q_{total}(r)}. \tag{6.2}$$

This code can also be used to identify trap states, due to the large value of local charge density in a trap state. In order to verify this, a trap state was created (shown in 6.8) by deliberately leaving a surface atom unpassivated. Using the aforementioned surface charge analysis code the correct location was correctly identified.

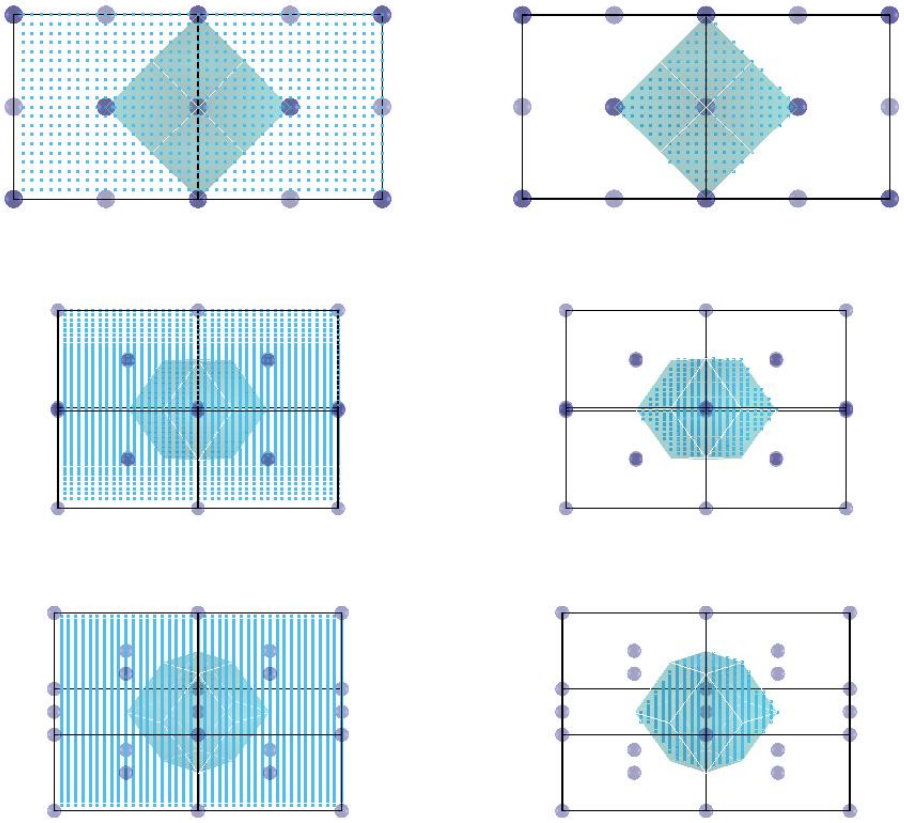

Figure 6.7 This figure illustrates a testto examine if the grid-points within local regions are correctly isolated. The left column shows all the grid-points. The right region shows those located within the defined region of space i.e. closer to a given atom. Different angles are shown to illustrate that is works from all perspectives. The grid points are shown inside and outside this region using the Voronoi method, confirming it is working correctly.

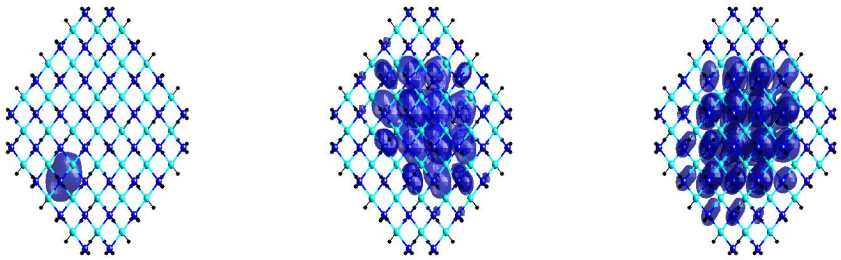

Figure 6.8 Trap state in a CdSe quantum dot with $r = 15\mathring{A}$ together with two core states. The location of this trap state was correctly identified using the surface charge analysis code. The local region is shown by the cyan box and the darker blue contours show the iso-surface of the trap state charge density.

6.8.4 Passivation Signature

The passivation signature is defined here as the average surface charge per bond type. Using the passivation signature, the quality of the bond specific passivation parameters can be decoupled from the system. This means a poor quality passivation can be identified and modified. The ability to isolate the effects of low quality passivants can be useful because the individual parameter can be tuned. This could easily be taken a step further to look at the effects of surface voids and surface facets.

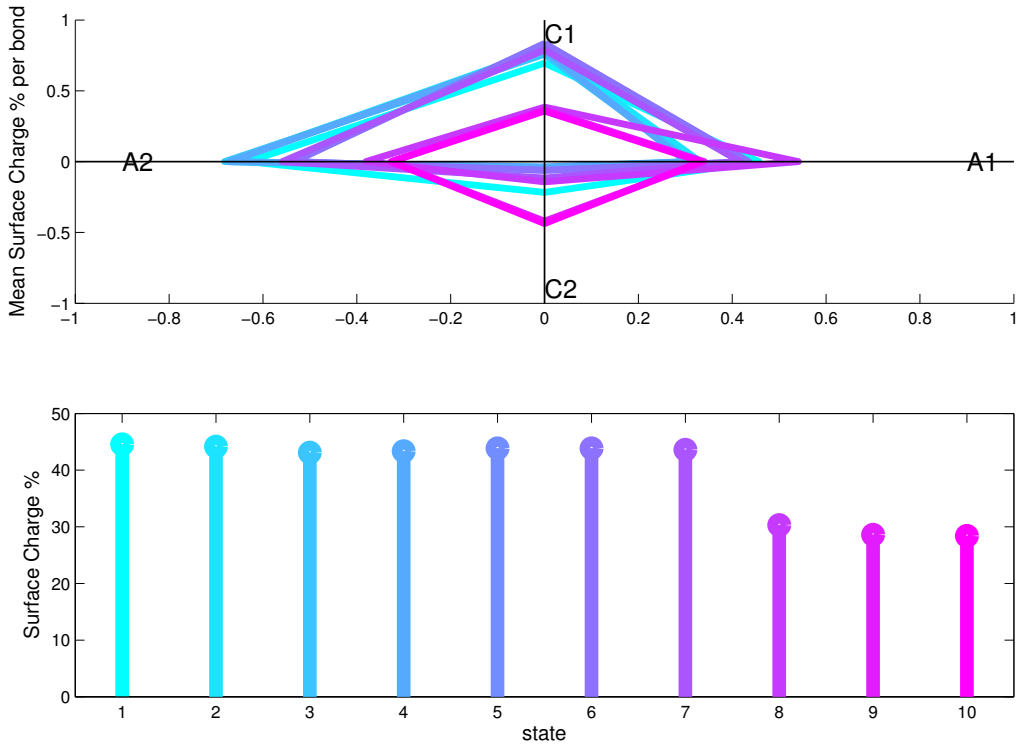

Figure 6.9 Passivation Signature for 10 CB eigenstates for a small InSb dot. This kind of graph was designed to visualise the quality of a passivation, the smaller the diamond the better the passivation since all four bond types (cation with one dangling bond, C1, cation with two dangling bonds, C2, anion with one [A1] or two [A2] dangling bonds) have a lower portion of the total charge around them.

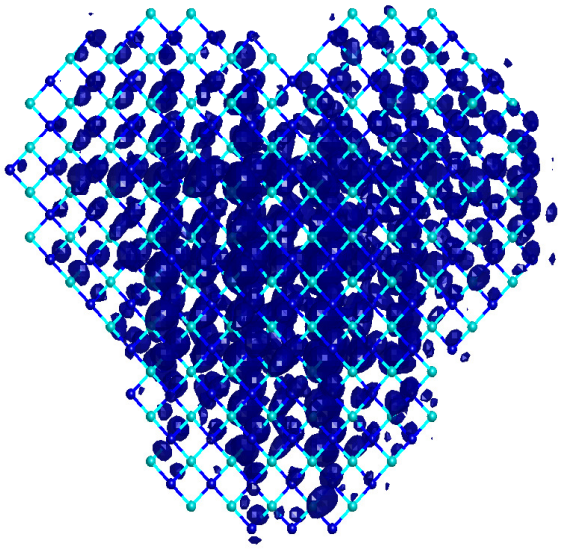

Figure 6.10 Charge Distribution for the CBM of an InSb tetrapod. A tetrapod is an example of a nanostructure where decomposition of charge needs to be implemented at the atomistic level.

6.9 Core/Shell Passivation

Core/shell passivation is a rather crude method to passivate a semiconductor nanocrystal and it was implemented for InSb, before a good passivation was found. If the passivation parameters for a particular semiconductor are unknown then an ultra-thin shell of a "passivatable" material can be used, with the appropriate passivants. The are no problems with the method insofar as the removal of states from the gap is concerned. However, the major downside is the fact that an additional material is introduced into the system, which could lead to theoretical parasitic effects.

6.10 Other Passivation Methods

Several alternative methods of passivation were explored. These methods were not successful in providing the foundations of a general passivation method. However, they are briefly documented here to show what has been tried and why it was not a suitable method. Firstly, passivation parameters where generated to have the same interaction potential with the surface atoms as the with the anions to cations (and vice-versa). The change in potential between anions and cations was interpolated on a three dimensional grid. Then a short range equivalent passivant was constructed to give a similar interaction at the edge of the crystal. Another idea was to create a barrier specifically tailored to fit any quantum dot based on the surface geometry, a passivation manifold with high potential to prevent the electron sampling the surface (shown in figure 6.11). The origins of this idea came from effective mass methods whereby an infinite potential barrier is used to ensure the wave-function resides within a quantum dot.

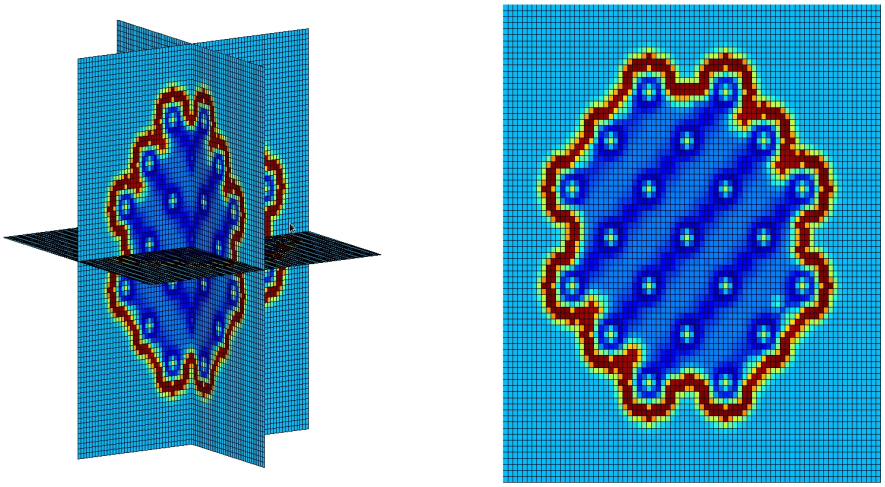

Figure 6.11 The total crystal potential of a passivation manifold wrapped around a quantum dot.

Unfortunately, this passivation manifold approach did not offer any promising results. The manifold was tested on both InSb and GaAs, for a large space of manifold parameters (distance from surface and the Gaussian height/width). Finally Crystal truncation was another method experimented in real-space (using the real-space GENPOT code). The idea was to generate a crystal potential that was cut from the bulk. Basically the supercell was filled with atoms, to generate the potential. Then the potential relating to the dot was isolated and the rest set to a very high value (to simulate a high energy potential barrier). This used a similar mechanism to the local charge distribution code, where points within local regions were found, and only those close to an actual lattice point were included. This yielded a set of surface states, and was abandoned as a possible method.

6.11 Conclusions

The outcome evolved slightly leading to a method of analysing the surface charge density on an atomistic level. This can be used as a standalone code within a traditional sampling-based passivation routine, which can be applied to test passivation parameters. In addition, it can also be used to identify and analyse trap states and possibly a number of other applications that require a detailed view of the surface charge density. Several different avenues were explored for passivation. The most effective were found to be automated algorithms and the idea of a passivant as a pseudo atom. This work led to the passivation of InSb, a semiconductor with a small band-gap and GaAs a semiconductor with a large band-gap. Looking at the work objectively, it is clear that an understanding of the discrete potential grid has been shown to be useful when deciding the step sizes for different bond lengths, poten-

tial widths and heights, which can be time saving in ruling out repeat calculations. Perhaps the most original addition to this method was the local charge distribution calculation, which not only provides a more accurate representation of the core and surface charge but also allows the charge around different bond types to be tuned giving more information on the quality of the passivation.

Chapter 7

Size-Induced Electronic Transitions

7.1 Introduction

Ideally semiconductor nanocrystals will exhibit direct optical transitions for states around the band edge. This will lead to efficient photon absorption, which is a desirable quality for photovoltaic devices. Electonic transitions can be defined in both real and reciprocal space. In this chapter new more complete methods are presented to define these transitions in a quantitative way.

7.2 Size-Induced Electronic Transitions - *k-space*

For direct band gap semiconductors we expect the conduction band states to be more susceptible to electronic transitions, due to the confinement energy having a greater effect on a lighter effective mass. For example, direct-to-indirect transitions in k-space (Figure 7.1) can occur if the CBM of the bulk material has a smaller effective mass than an electronic state above it with a conduction-band valley. If the difference in energy between these two valleys is less than the change in confinement energy then

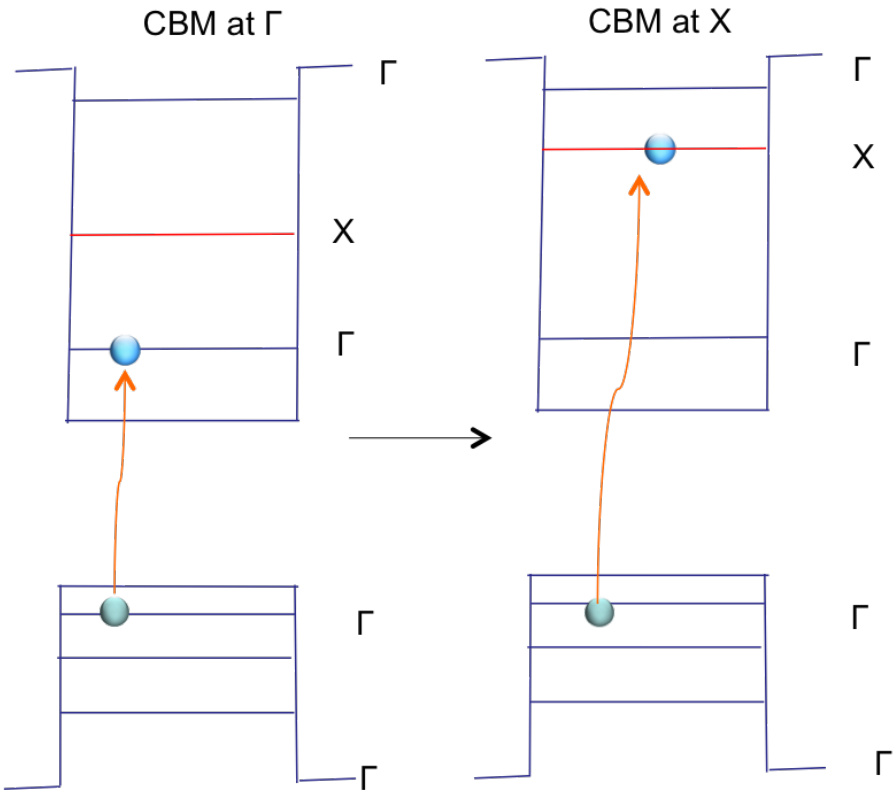

Figure 7.1 Direct-to-indirect transitions in reciprocal space. Adapted from [143]

a direct to indirect transition can occur. An electronic transition of this type was predicted to occur in free-standing GaAs nanocrystals. [144]. This was confirmed in theoretical work by Zunger's group [143].

7.3 Distribution of k-vectors

Momentum is a conserved physical quantity. Therefore an electron cannot gain energy and move to a higher state with different k-vectors without a change in momentum (usually provided by a phonon). A direct transition in reciprocal space occurs when an electron moves from one state to another where both states have a largely similar

distribution of momentum. Conversely, an indirect transition occurs when there is a largely different distribution of position and momentum. This means we start by obtaining the eigenvalues and eigenfunctions for a pair of states (usually the band edges) by solving the Schrödinger equation

$$\left[-\frac{1}{2}\nabla^2 + V(r) + V_{so}\right]\psi_i = E_i\psi_i \tag{7.1}$$

The specific details of solving this equation are given in chapter 5. The solution to equation 7.1 is in the form of a superposition of plane wave basis functions e^{ikr} with expansion coefficients $c_i(k)$

$$\psi_i(r) = \sum_k c_i(k)\, e^{ikr}. \tag{7.2}$$

To analyse the results, we have subjected all wave-functions to a "majority representation" decomposition

$$P_i(k) = \sum_{n=1}^{nstates} \left|\langle \psi_i(r) \left| u_k(r)\, e^{ikr} \right\rangle\right|^2 \tag{7.3}$$

where $u_k(r)\, e^{ikr}$ is a complete set of bulk Bloch states. The projection of Eq. 7.3 is evaluated as $P_i(k) = \sum_G |C_i(k+G)|^2$ and is referred to as the spectral weight at a given k-point, here G is the reciprocal lattice vector. The total sum for all the spectral weight should sum to unity (i.e. the electron must be somewhere).

The reciprocal-space character of state i is quantified by summing $P_i(k)$ over all the k points contained in a Voronoi cell Ω_{vor} centred around a specific high-symmetry point (Γ, L, X, etc.): $w_i^{\Gamma(vor)} = \sum_{k\in\Omega_{vor}} P_i(k)$.

7.4 Voronoi Decomposition of k-space

Decomposition of k-space has been implemented by generating spheres seeded around high symmetry points Γ L and X [143]. The problem with this method is that spheres do not pack in a 3 dimensional Euclidean space. Therefore, as an alternative to defining spherical regions, we instead define Voronoi regions seeded around their respective high symmetry points. We call these high symmetry regions: i.e. regions of space around a high symmetry point. This defines regions that pack, such that every k-point is considered and assigned to a unique high symmetry point. To determine the k-points within a high symmetry region ($k \in \Omega_{vor}$), a Euclidean distance matrix between all the high symmetry points λ_j and all the k-points k_i are defined as $a_{ij} = \|k_i - \lambda_j\|_2^2$ giving an $n \times m$ matrix where n is the number of high symmetry points and m is the number of k-points. The index of $min(a_{ij})$ is then found and used to reference the closest high symmetry point for every k point. This defines a locus of points which are located within the Voronoi cell corresponding to the high symmetry point. The total spectral weight in each high symmetry region can then be summed up and expressed as a fraction of the total spectral weight (the total spectral weight should be very close to unity since the probability of the electron being found somewhere is one, and this electron will have a momentum component).

In order to illustrate the process of Voronoi decomposition, we use the example of the fcc lattice. The fcc Brillouin zone is a truncated octahedron with six unique high symmetry points (Γ, L, X K, U and W) meaning that there are to be seven corresponding high symmetry regions, one seeded around each point (shown in figures 7.2 and 7.3).

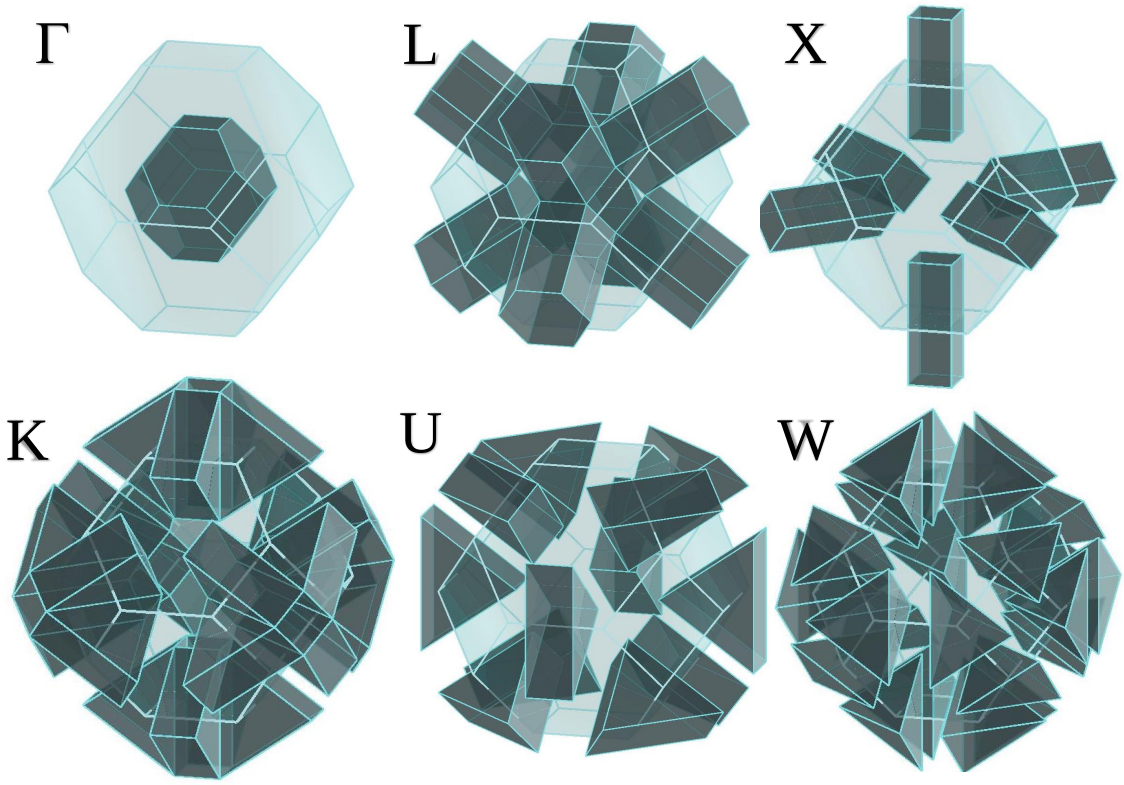

Figure 7.2 Complete set of high symmetry regions associated with every high symmetry point for an fcc lattice. The full shape of each region is shown extended into the neighbouring Brillouin zone. The centre of these regions are Γ (center of the Brillouin zone), L (centre of a hexagonal face), X (centre of a square face), K middle of an edge joining two hexagonal faces, U (middle of an edge joining a hexagonal and a square face) and W (corner points).

7.4.1 Boundary Problem

The discrete distribution of k-vectors between neighbouring Voronoi cells may lead to a potential boundary problem. Neighbouring cells have a well defined interface between one another, and if a k-point is on or close to the boundary, all the spectral weight located at that point is assigned to only one k-point. To overcome this problem an interpolation method needs to be applied to mathematically construct more data points within the range of the discrete data set of k-points. The goal of this

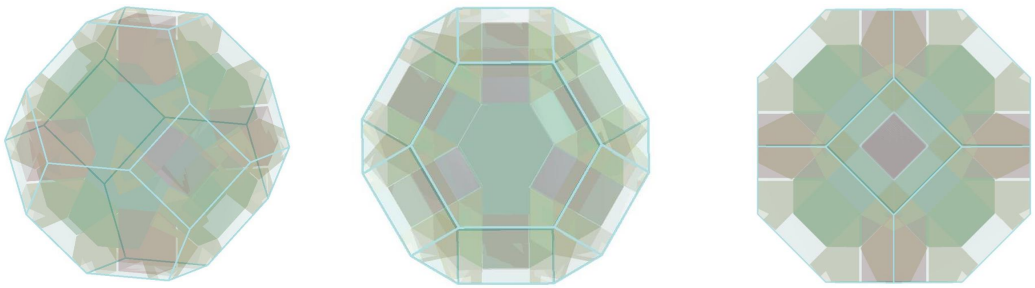

Figure 7.3 Illustration of the Brillouin zone with the high symmetry regions represented in different colors. Each of the three graphs is the same plot from a different viewpoint.

interpolation method would be to make sure the spectral weight is distributed more smoothly, in order to give a more accurate depiction of how the momentum of the state is distributed. While there are many mathematical methods of interpolation, they are non designed specifically for this problem. With that in mind, a vector interpolation method was created for this task. Once again the method leans heavily on Voronoi theory, where this time a Voronoi cell is seeded around each k-point to define a local region. A meshgrid is then defined over the entire Brillouin zone with a more dense resolution than the k-mesh. The spectral weight for each k-point is then distributed evenly over all local mesh points.

7.5 Electronic Transitions in Real-Space

Electronic transitions are usually described in terms of k-vectors. However, the position vectors can also be considered. If a pair of states with different charge distributions have little overlap between one-another, then a transition between these two states is highly improbable. This type of transition may occur in a variety of scenaria: i) core-shell/embedded matrix structure when electrons and holes are distributed in

different materials; *ii*) trap/defect state, where the localised charge distribution creates very little overlap with the core states, leading to a low transition probability. A direct transition in real-space occurs when an electron moves to a state with a largely similar charge distribution. The logical progression is to implement a more quantitative method, whereby the overlap of a conduction band wave-function $\psi_{vb}(r)$ and a valence band wave-function $\psi_{cb}(r)$ is calculated.

The wave-function overlap cannot be implemented on a point by point basis since there is no accounting for the distribution over a particular region or the nearest position that can be occupied. This is illustrated in figure 7.4.

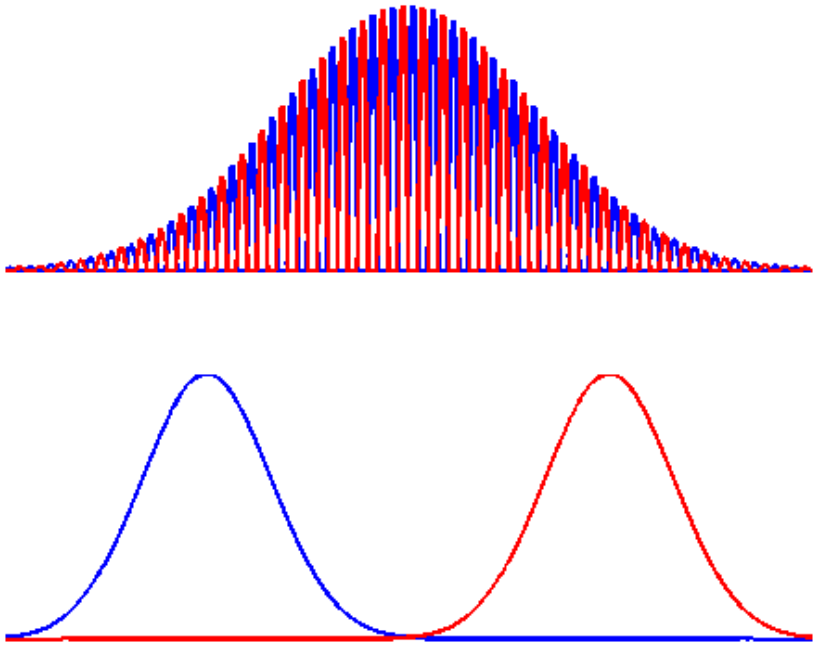

Figure 7.4 Two hypothetical wave-function overlap scenarios, one marked in red the other marked in blue. The first scenario shows a pair of wave-functions where the probability of occupation alternates between high and low. These two wave-functions are out of phase so the overlap is zero. The same as two completely separate wave-functions separated by a large distance.

7.6 Real-space Volumetric Overlap - *real space*

A regional analysis is an alternative to a point by point approach. If the active volume of a state can be defined, then the overlap between two states can be computed.

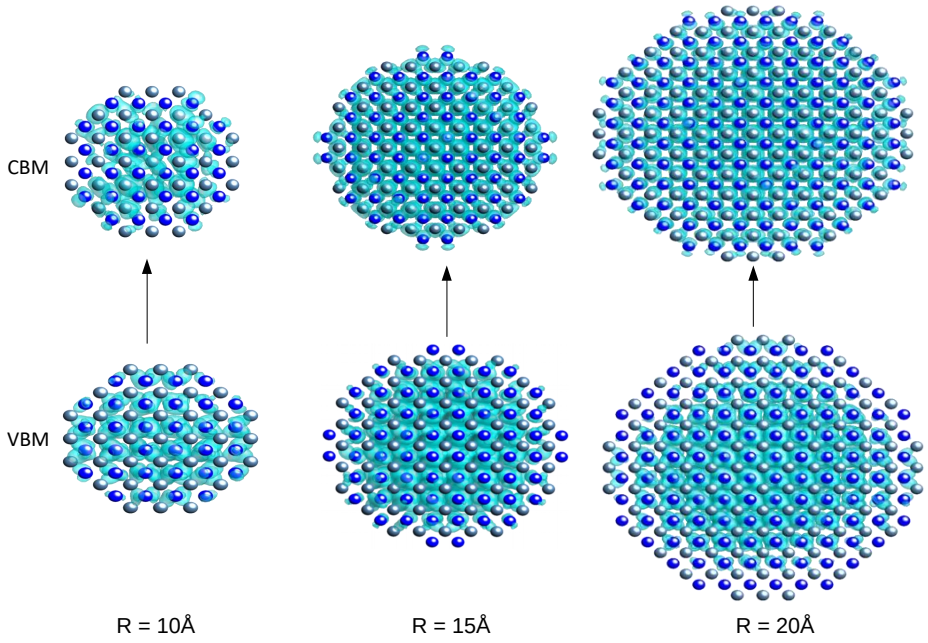

Figure 7.5 Charge Distributions for the CBM and VBM of InSb quantum dots with radius 10, 15, and 20Å.

The charge distributions shown in figure 7.5 are all considered to yield direct transitions in real-space. This is because the majority of the charge originates from the same region of the structure. The basic premise of volumetric overlap is that we identify how much of the active volume is shared between a pair of states. Equation 7.4 shows how the percentage of volume overlap can be calculated, where V_a and V_b are the effective volumes of eigenstates a and b Examples of excitonic overlap are shown in figure 7.6.

$$P_{overlap} = 100 \times \frac{Vol(V_a \cap V_b))}{Vol(V_a \cup V_b)} \tag{7.4}$$

The effective volume is defined as the region of space where the majority of spectral weight resides. The contours of the charge distribution in 7.5 are defined by an iso-surface. The iso-value is computed using a histogram on the volumetric data. These give a good representation of the majority charge, by finding the points that are enclosed by the triangulated data. For a pair of states the union and intersection for a pair of charge distributions can be found. This allows the percentage overlap given in equation 7.4 to be calculated. The volume for a set of points can be found by using the convex hull function, and the points within a triangulated surface can be found using the inpolyhedron method, which is part of the geom 3D toolbox. The convex hull can either be the bounding active region or alternatively the sum of all the clusters, which can be isolated using a k-means clustering method.

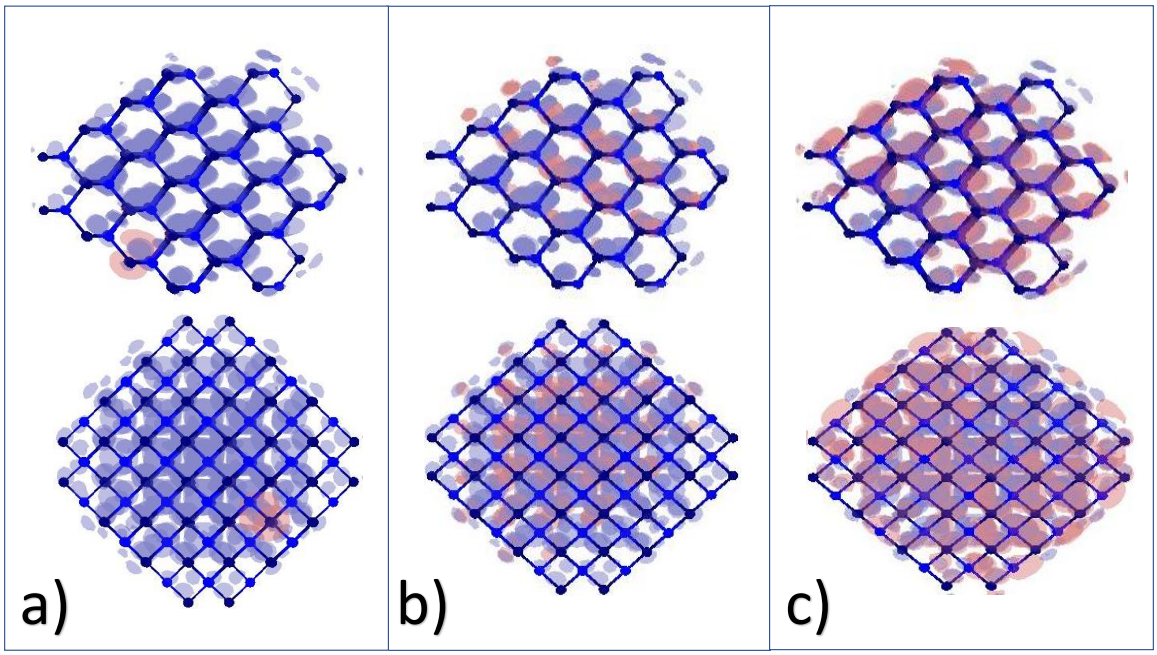

Figure 7.6 Charge distributions for three electron-hole configurations, a) VB trapping state with very little overlap with the CB, b) states with medium overlap, c) states with high overlap (c). The isosurface are red and blue for the VB and CB respectively. Note that the upper and lower plots are represent the same data from a different viewpoint.

7.7 Grand Transition Characteristic

The goal here is to find a single parameter that describes the direct portion of a transition between a pair of states. For example, if the CBM composition in k-space were 70% Γ, 15% X, and 15% L (assuming we consider a three way partition), and the VBM was 90% Γ, 5% X, and 5% L, then the transition characteristic would be $\Gamma_{CBM}/\Gamma_{VBM}$, which is equal to 77.78% direct. In real space the volumetric overlap is the best metric found to describe the extent of 'directness' in a transition, so it can be used as the real-space transition characteristic. By putting these parameters together we have the Grand Transition Characteristic:

$$\Theta_{grand} = mean(\Theta_{kspace}, \Theta_{rspace}), \tag{7.5}$$

where Θ_{grand} is the grand transition characteristic, while Θ_{kspace} and Θ_{rspace} are the respective real-space and k-space characteristics. This might be a useful parameter in expressing the overall direct nature of a transition, which may be useful in some circumstances.

7.8 Conclusions

The new Voronoi decomposition model (k-space) could hopefully lay the foundations for further investigations into direct-to-indirect transitions. This method allow every k-point to be assigned to a unique high symmetry point, without any overlap between neighbouring regions. Spectral interpolation of the k-points is an additional option, which might be useful in some circumstances, however it is not essential. The method could also be extended to work with different crystal structures such

as rock-salt or wurzite. The real-space analysis methods are not fully mature and would require further development. Volumetric overlap could be useful if applied to core-shell structures in real-space. This would provide a quantitative analysis of how much of the charge distribution resides in each material section. Also novel structures such as tetrapods could be investigated, a high level of charge localisation is present in different arms of the structure.

Chapter 8

Excited State Dynamics in InSb Quantum Dots

8.1 Introduction

The ultra-fast bi-exciton decay times observed in colloidal InSb quantum dots might be due to an Auger recombination process, which would imply ultra-fast carrier multiplication. This, together with the strong confinement, high carrier mobility and narrow band-gap would make these structures ideal for next generation quantum dot based photovoltaic devices. In this chapter we explore this possibility, the work was published in the The journal of physical chemistry letters [145].

8.2 Physical Properties of InSb

Colloidal InSb quantum dots show particularly promising physical properties for next generation electronic and optoelectronic devices. This is due to the unique physical properties of bulk InSb, which has excellent transport and strong confinement effects,

due to the extremely large electron mobility and exciton Bohr radius, respectively [146].

Experiments on the size dependent optical properties of InSb QDs [147], show the band gap converging to the value of the bulk band gap at L rather than to that at Γ, with increasing dot size. A possible explanation of this is a direct-to-indirect transition in reciprocal space (see chapter 7), taking place outside the experimental range, i.e., for $R > 3.2$ nm, in contrast with what was predicted for other semiconductor materials [143], where such a transition occurred at much smaller sizes (the strong confinement of InSb might be a cause of this). In addition, the measured bi-exciton recombination times [148], attributed to Auger processes, are an order of magnitude faster in InSb QDs than observed [149–151] and predicted [152] in materials such as CdSe. As for the process of electron cooling, also attributed to Auger decay, the measured lifetimes are in line with those commonly found in nanostructures [149, 150, 152–156]. These observations rise the question of whether, unlike in the case of other materials, different (intra-band and inter-band) non-radiative decay processes may be governed by different (i.e., Auger and non-Auger) mechanisms in InSb quantum dots.

8.3 Stoichiometry: Theory & Experiment

The experimental results for the size-dependent absorption spectra found in *Liu et al* do not provide any information relating to the stoichiometry of the structures used. In-order to shed some light on the differences between the experimental [147] and theoretical (calculated using effective mass methods [157]) spectra, two different stoichiometries are used. These are created by exchanging the anion and cation sites, as shown in figure 8.1. While neither of these are likely to match what has

been presented experimentally, the results will give some indication of how much the electronic and optical properties differ.

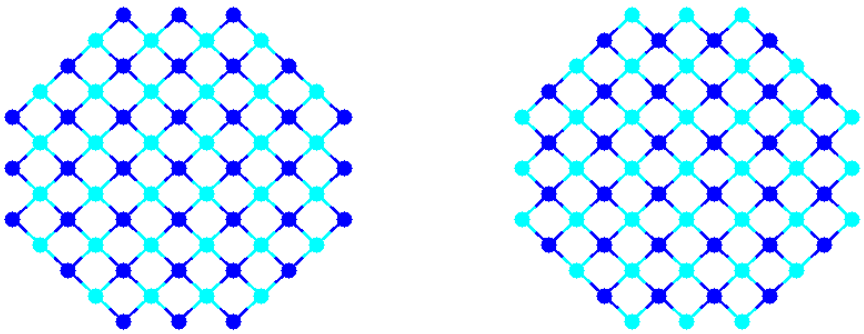

Figure 8.1 Alternate stoichiometry is illustrated here. The atomic positions are identical for both structures, however, anions (cyan circles) and cations (blue circles) are exchanged.

Continuum-based approaches assume perfect stoichiometry (same numbers of anions and cations), since the method is based on parameters derived from the bulk. In addition, careful control of the stoichiometric composition is a further tool to modify and fine tune the properties of InSb dots, as it has been shown to be the case for PbS nanostructures [158].

8.4 Methodology

The eigenvalues and eigenvectors are obtained using the semi-empirical pseudopotential method [159], including spin-orbit coupling. The excitonic effects are accounted for via a configuration interaction scheme [160]. This is covered in more detail within chapter 5. The Voronoi decomposition method shown in chapter 7 is used to analyse the composition of the eigenvectors, to see if there is a direct-to-indirect transition. Finally, the probability of transition per unit time between a pair of eigenvectors is

used to calculate Auger decay times, which can be calculated using Fermi's Golden Rule according to [152]

$$(\tau_{\mathrm{AMT}})_i^{-1} = \frac{\Gamma}{\hbar} \sum_n \frac{| < i|\Delta H|f_n > |^2}{(E_{f_n} - E_i)^2 + (\Gamma/2)^2}. \tag{8.1}$$

where $|i>$ and $|f_n>$ are the initial and final states, E_i and E_{f_n} are their energies, ΔH is the Coulomb interaction and $\hbar/\Gamma$ is the lifetime of the final states.

8.5 Excitonic Energies

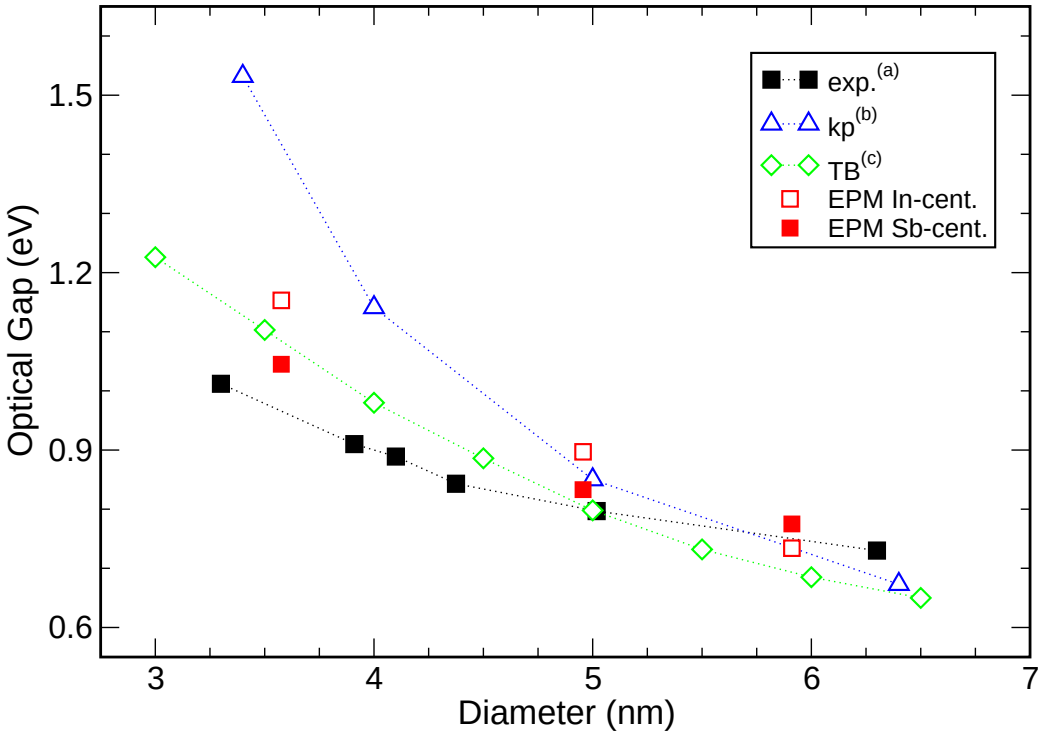

Figure 8.2 Optical gaps: comparison of our results (red empty squares, In-centred; red solid squares, Sb-centered) with experiment [147] (black solid squares), and the results of other theoretical approaches (8-band **k·p** method [157], empty blue triangles; atomistic tight-binding approach [161], empty green diamonds).

Figure 8.2 presents a comparison between the excitonic energy gaps calculated

for In-centred and Sb-centred quantum dots of different sizes and the experimentally measured optical gaps [147]. It can be seen that an In-rich stoichiometry yields slightly larger optical gaps than observed experimentally, for small structures, whereas Sb-rich structures reproduce observation well within the range of sizes considered. Figure **??** also includes the predictions of other theoretical approaches, the continuum-like 8-band **k·p** method [157] and the atomistic tight-binding approach [161]. While the latter calculations (obtained for anion-centred structures) yield good agreement with experiment, the agreement achieved by the former approach is only good in a very limited size range. Most importantly, both theoretical curves (and our In-centred one) *cross* the experimental curve, i.e. predict an increasingly lower gap than is observed, for sizes larger than about D=5 nm, a characteristic not exhibited by our Sb-centred results. As the room temperature InSb bulk band gap at Γ is 0.180 eV [146], it would be reasonable to expect the excitonic gap of the quantum dots to converge to this value with increasing size, as the predictions of **k·p** theory appear to do. However, the experimental gaps seem instead to converge to a larger value, closer to the bulk band gap at L. [147]

8.6 Wave Function Composition

A direct-to-indirect Γ-to-L transition could be responsible for the observed convergence of the excitonic spectra within this size range. This effect has already been documented in the case of GaAs quantum dots [143]. If this is the case, since bulk InSb has a direct band gap, the conduction band of the observed dots should have a prevalent L character and should undergo an L-to-Γ transition for structures larger than those within the experimental range. To help answer this question, we performed

a k-space decomposition of the conduction band (CB) wave functions.

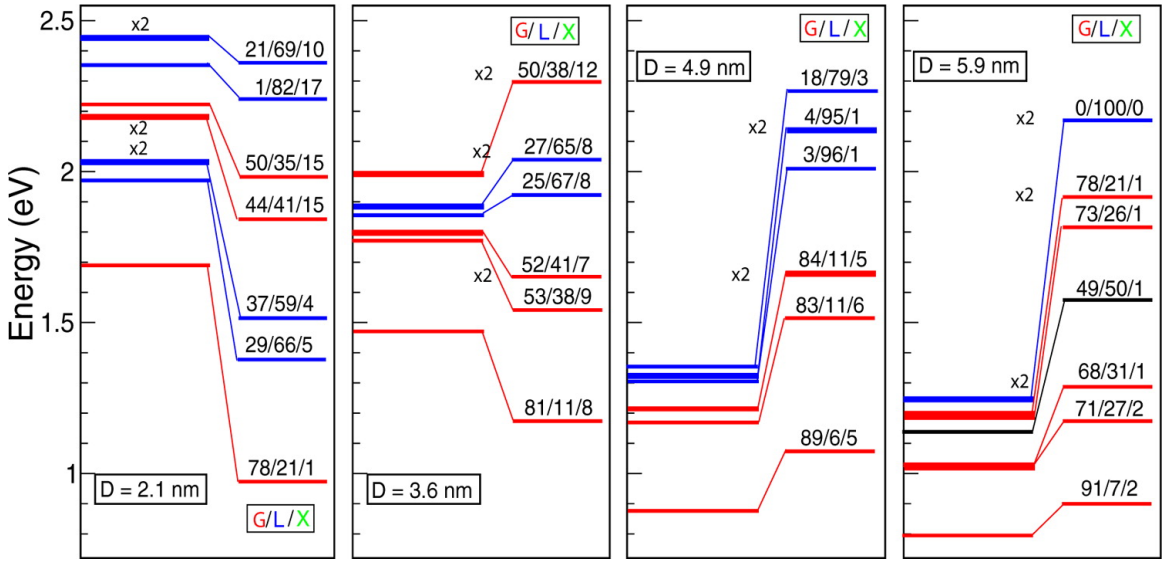

Figure 8.3 Conduction band electronic structure for four different Sb-centred dot sizes: Each panel refers to a different value of the dot diameter D and displays energy levels (left-hand side) and k-vector decomposition (right-hand side). The different states are colored according to their main character (Γ, red; L, blue; and X, green) resulting from such a decomposition. Two-fold degenerate states are indicated by 2.

As shown in 8.3, the wave function of the CB edge receives a non negligible contribution from the L point in the case of small dots. Such a component decreases with increasing size, up to $D = 5$ nm and then increases again for $D = 6$ nm, in Sb-centred structures. Interestingly we find that this trend is accompanied by a crossover between Sb-rich and In-rich structures for Sb-centred dots. In fact, for sizes smaller than $D = 6$ nm, Sb-centred nano-structures are also Sb-rich, whereas for $D = 6$ nm, the stoichiometry is slightly reversed with less than 1% excess of In atoms.

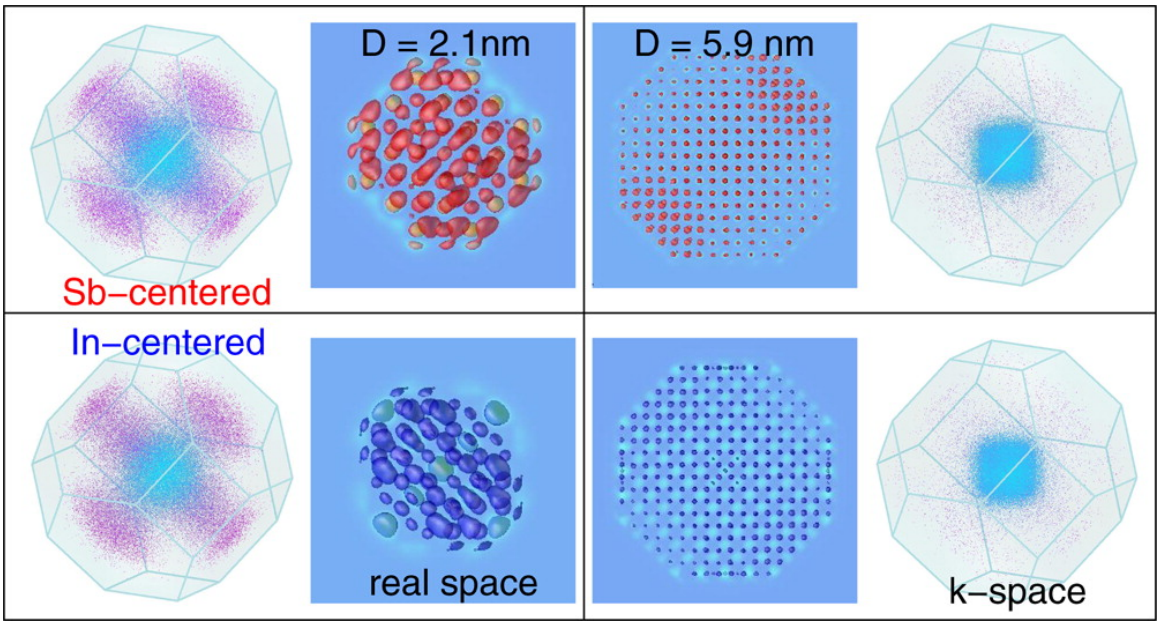

Figure 8.4 Real- and k-space representation of the CBM wave functions of $D = 2.1$ and $5.9nm$ dots for In-centred (blue) and Sb-centred (red) structures.

As a consequence of this mixed character of the CBM, the dot optical gap is not expected to converge to the bulk band gap at Γ for sizes within the experimental window, consistently with observation. For larger sizes, the L component is expected to vanish and the gap to converge to 0.18 eV. Again it is worth stressing that the 8-band **k·p** method cannot handle stoichiometry and that its predicted energy gaps *underestimate* the experimental ones for large R, despite the fact that (i) this approach is known to *overestimate* confinement (hence the band gap) due to the assumption of an infinite confining potential [157], and (ii) its predicted p character for the VBM [157] would imply absorption to occur between VBM-2 and CBM, again leading to an *overestimate* of the band gap. According to our results, the VBM has instead s-like symmetry in both In-rich and Sb-rich quantum dots within the experimental size range, and therefore transitions between band edge states are optically allowed. Interestingly, even an atomistic tight-binding method [161] did not appear to predict

the correct behaviour of the excitonic gap in quantum dots with diameters > 5 nm. One possible reason for this is the restricted choice of the basis set used, which may limit the validity of the electronic structure description to regions near the Γ point.

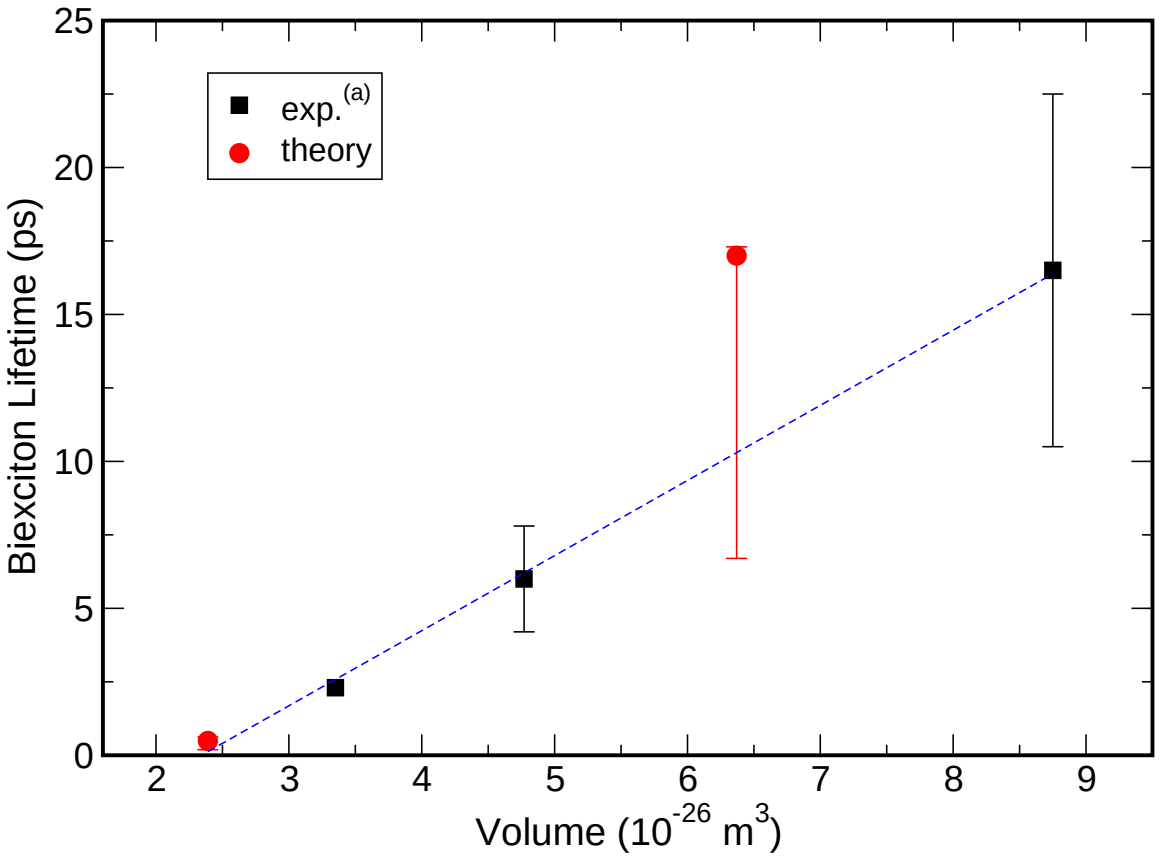

Figure 8.5 Bi-exciton recombination times: comparison of our results (red solid circles) with experiment [148] (black solid squares). The dashed line is a linear fit through all (experimental and theoretical) data. See the Figure 8.7 for an explanation to the origin of the error bars. Note that the carrier lifetimes were calculated by Marco Califano using his code as part of a joint publication.

8.7 Lifetimes of non-radiative carrier dynamics

Efficient Auger recombination is usually thought to be the cause of non-radiative bi-exciton decay. When the recombination takes place, the exciton energy is non-

radiatively transferred to another charge carrier, creating a hot exciton (see figure 3.1) [150]. CdSe quantum dots have been shown to exhibit Auger recombination times ranging from around 45 ps to 147 ps for quantum dot radii between 2.3 nm and 2.8 nm [150] (i.e., volumes $V = 5.1 \div 9.2\ 10^{-26}$ m^3). Interestingly, the bi-exciton decay times measured in InSb dots, although scaling linearly with the nanostructure volume, as expected for AR [149, 150], were about 1 order of magnitude smaller than in CdSe (6 ps to 16.5 ps for V$\sim 4.8 \div 8.8\ 10^{-26}$ m^3, [148] corresponding to R$\sim 2.25 \div 2.75$ nm), and about a factor of 2 faster than AR times observed in InAs quantum dots [153] ($\sim$ 10 ps for $V = 4.0\ 10^{-26}$ m^3). If these exceptionally fast bi-exciton decay times were indeed due to AR, then they could hint to very efficient carrier multiplication in these systems, as the two processes share the same matrix elements. This, coupled with a small electron effective mass, a low band gap and the highest mobilities among semiconductor materials, would make InSb quantum dots ideal building blocks for next-generation solar cells. Aiming to shed light on this issue, we therefore calculated AR times for InSb dots with two different radii in the experimental range. Our results, displayed in 8.5, confirm that the bi-exciton decay times measured experimentally are indeed due to efficient AR, opening the door for the exploitation of these nanostructures in photovoltaic devices.

Chang *et al.* recently reported fast electron intra-band decay times for colloidal InSb quantum dots [148]. These decay times were attributed to Auger cooling (AC), a non-radiative decay process in which the excess energy of a hot electron is transferred, upon its decay to the conduction band edge, to the hole, which is excited deep in the valence band [150]. Our calculated AC times are in good agreement with experiment, as shown in 8.6, supporting the theory that both non-radiative decay processes observed in this material are Auger-like.

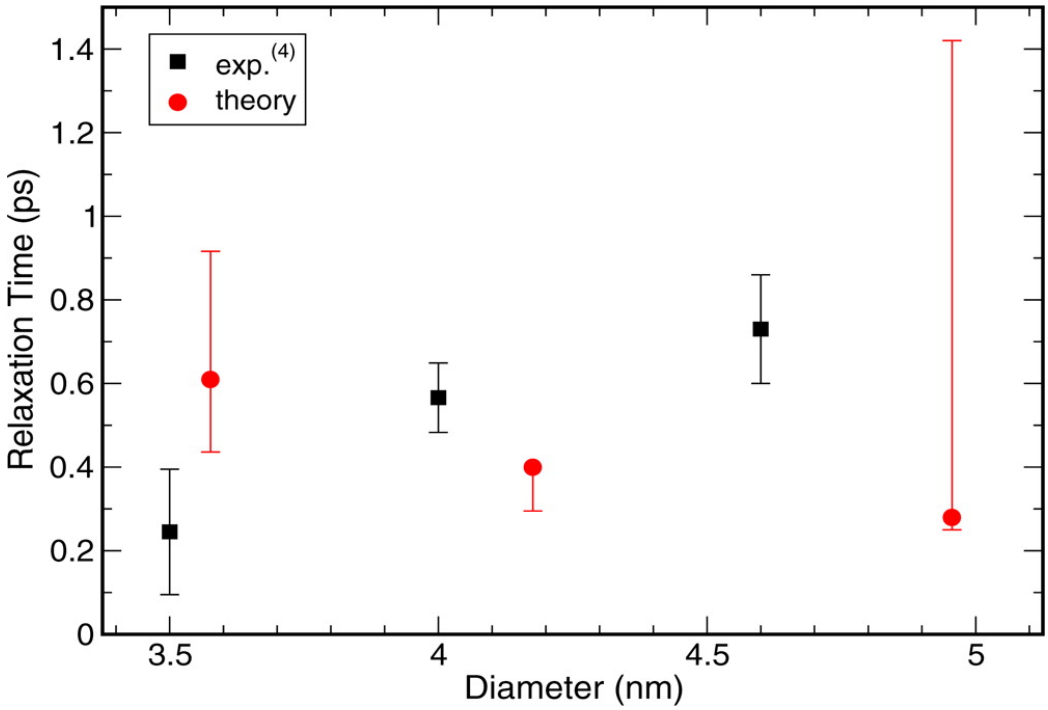

Figure 8.6 Electron cooling times as a function of NC diameter: Comparison of our results (red solid circles) with experiment [148] (black solid squares). For details of the determination of the error bars on the theoretical data, see the Figure 8.7.

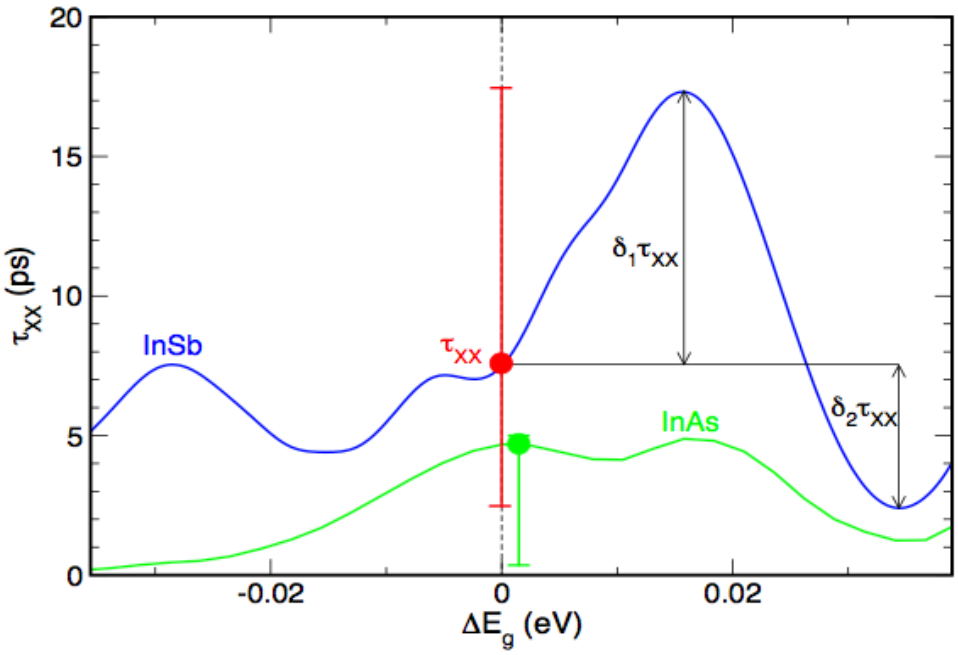

Figure 8.7 Calculated AR times for oleic-acid-capped InSb (R = 2.1 nm, blue curve and red symbol) and InAs (R = 2.0 nm, green curve and green symbol) dots in tetrachloroethylene 1,2 plotted as a function of ΔE_g, the variation of the energy gap around the value calculated for this size ($\Delta Eg = 0$), for a range of energies corresponding to a 5% size distribution in InSb colloidal quantum dots. The green symbol is slightly displaced to the right for clarity. The black arrows indicate the largest variations of τXX within this energy interval, compared to its value at $\Delta E_g = 0$, and are represented as asymmetric error bars in the symbols.

Figure 8.7 shows the methodology behind the error bars that appear in Figures 8.5 and 8.6. If τ (Δ E = 0) is located at a maximum of the curve, the error bar will appear only towards smaller values (this is the case, e.g., for $\tau(D = 4.18nm)$ in Fig. 8.5), whereas the opposite is true in the case of $\tau(\Delta E = 0)$ being at a minimum (see τ (D = 4.96 nm) in Fig. 8.6).

8.8 Concluding Remarks

The application of the atomistic semi-empirical pseudopotential method to InSb quantum dots has provided evidence in support of the following:

i. the s-like symmetry of their VBM in both In-rich and Sb-rich structures; in contrast with the predictions of continuum approaches;

ii. (a non-monotonic behaviour of the L-component (i.e., the contribution from k-vectors close to the L point in the first Brillouin zone) of the CBM wave function with size in Sb-centred structures (not exhibited by In-centred QDs);

iii. an apparent failure of the band edge absorption to converge to the bulk band gap, even for considerably large dot sizes, consistent with observation, as the transition to a completely Γ-like CBM, and therefore a bulk-like band edge absorption, is expected to occur at a size close to the exciton Bohr radius ;

iv. the importance of the structure's stoichiometry as a crucial parameter in the calculations, as only considering the observed composition will lead to an accurate reproduction of the experimental data for both radiative and non-radiative decay processes; [68].

v. the Auger-like nature of the ultra fast bi-exciton decay times, suggesting ultra-fast carrier multiplication.

Chapter 9

Main Achievements & Further Work

9.1 Main Achievements

The main achievements can be summarised as follows:

i The investigation into the improved carrier multiplication of quantum rods [58];

ii A new model to determine the size of strained quantum dots;

iii New passivation and local charge density methods;

iv The wave function decomposition methods in real and reciprocal space;

v The investigation into the carrier dynamics of colloidal InSb quantum dots [145].

In addition there have been several useful codes written that can be used in the future.

9.2 Additional Theoretical Analysis

9.2.1 Passivation & Surface Analysis

The surface charge analysis code used for passivation could be applied to other semiconductor materials. The goal would be to create a fully tested general passivation method, which worked for a wide range of semiconductors. In addition, work that analyses surface trap states in more detail could be carried out. As this code works at the atomistic level, it can be used to determine the surface charge density for structures with any shape such as rings or tetrapods. This type of application would help to justify the development of this code.

9.2.2 Novel Quantum Dot Shapes

Codes were developed to generate the strucures for novel quantum dot shapes, such as rings, tetrapods and pyramids. This opens the door to many possible theoretical investigations. The most interesting is possibly tetrapods, which have been attracting a lot of attention recently, as they exhibit a large difference between the peak excitation and the peak emission wavelength [162]. Using the tetrapod generation code, different structures can be analysed [163]. It would be interesting to compare the charge delocalisation of excitons in these structures with that in quantum dots and quantum rods. The real-space decomposition code could be applied to give a quantitative analysis of this.

9.3 Additional Code Development

9.3.1 Semi-Emprical Pseudopotential Codes in MATLAB

High-performance parallel codes can be very difficult to maintain due to their size and complexity, which can be an obstacle to further code development. An ambitious side project was to write a new full set of semi-empirical pseudopotential codes in MATLAB. At present a full working total crystal potential code has been created, which outputs suitable files that can be used with PESCAN. However, the creation of a MATLAB eigensolver is a long way off. It would be very useful since it would allow research to be carried out on a modern workstation, without the need to log into a supercomputer. The goal would be to create something more compact and workable. For example, the MATLAB GENPOT is around a hundred lines of code, whereas the FORTRAN version is several thousand. The problem with doing this is the amount of time required to write a new code that has an equivalent functionality to the existing one. Even if this was possible, the gains would be marginal and would not justify the time and effort devoted to this task. Indeed, producing journal papers, using codes that are already available, is usually seen as a better use of a researcher's time.

9.3.2 Visualisation

All of the 3D graphs in this thesis were plotted using MATLAB plotting scripts. These could all be combined into a single package with a nice graphical user interface. This would allow the user to visualise only selected features within a plot, for example, the local regions around each atom (as shown in figure 6.5). This could be useful since it is not possible to do this using many commercial plotting software packages.

9.3.3 Maintaining Existing Codes

There are many codes that need additional commenting/documentation so that they are more user-friendly. It is regrettable that this was not done at the time. However, it would be very useful to have a complete repository of the work.

This page is intentionally left blank

Bibliography

[1] W. Shockley and H. J. Queisser, "Detailed balance limit of efficiency of p-n junction solar cells," *Journal of applied physics*, vol. 32, no. 3, pp. 510–519, 1961.

[2] M. Jacoby, "The future of low-cost solar cells," *Chemical and Engineering News*, vol. 94, no. 18, pp. 30–35, 2016.

[3] S. Rühle, "Tabulated values of the shockley–queisser limit for single junction solar cells," *Solar Energy*, vol. 130, pp. 139–147, 2016.

[4] E. M. Bomhard, H.-P. Gelbke, H. Schenk, G. M. Williams, and S. M. Cohen, "Evaluation of the carcinogenicity of gallium arsenide," *Critical reviews in toxicology*, vol. 43, no. 5, pp. 436–466, 2013.

[5] A. De Vos, "Detailed balance limit of the efficiency of tandem solar cells," *Journal of Physics D: Applied Physics*, vol. 13, no. 5, p. 839, 1980.

[6] I. Fraunhofer, "New world record for solar cell efficiency at 46% french-german cooperation confirms competitive advantage of european photovoltaic industry," *Press Release*, vol. 26, no. 1, 2014.

[7] P. Lobaccaro, A. Raygani, A. Oriani, N. Miani, A. Piotto, R. Kapadia, M. Zheng, Z. Yu, L. Magagnin, D. C. Chrzan, *et al.*, "Electrodeposition of high-purity indium thin films and its application to indium phosphide solar cells," *Journal of The Electrochemical Society*, vol. 161, no. 14, pp. D794–D800, 2014.

[8] F. Pianezzi, P. Reinhard, A. Chirilă, B. Bissig, S. Nishiwaki, S. Buecheler, and A. N. Tiwari, "Unveiling the effects of post-deposition treatment with different alkaline elements on the electronic properties of cigs thin film solar cells," *Physical Chemistry Chemical Physics*, vol. 16, no. 19, pp. 8843–8851, 2014.

[9] M. Grätzel, "Dye-sensitized solar cells," *Journal of Photochemistry and Photobiology C: Photochemistry Reviews*, vol. 4, no. 2, pp. 145–153, 2003.

[10] M. Liu, M. B. Johnston, and H. J. Snaith, "Efficient planar heterojunction perovskite solar cells by vapour deposition," *Nature*, vol. 501, no. 7467, p. 395, 2013.

[11] S. Günes, H. Neugebauer, and N. S. Sariciftci, "Conjugated polymer-based organic solar cells," *Chemical reviews*, vol. 107, no. 4, pp. 1324–1338, 2007.

[12] A. Nozik, "Quantum dot solar cells," *Physica E: Low-dimensional Systems and Nanostructures*, vol. 14, no. 1, pp. 115–120, 2002.

[13] W. T. Welford and R. Winston, "Optics of nonimaging concentrators. light and solar energy," 1978.

[14] J. A. Schuller, E. S. Barnard, W. Cai, Y. C. Jun, J. S. White, and M. L. Brongersma, "Plasmonics for extreme light concentration and manipulation," *Nature materials*, vol. 9, no. 3, p. 193, 2010.

[15] T. Trupke, M. Green, and P. Würfel, "Improving solar cell efficiencies by up-conversion of sub-band-gap light," *Journal of Applied Physics*, vol. 92, no. 7, pp. 4117–4122, 2002.

[16] J. P. Clifford, K. W. Johnston, L. Levina, and E. H. Sargent, "Schottky barriers to colloidal quantum dot films," *Appl. Phys. Lett.*, vol. 91, p. 253117, 2007.

[17] J. M. Luther, M. Law, M. C. Beard, Q. Song, M. O. Reese, R. J. Ellingson, and A. J. Nozik, "Schottky solar cells based on colloidal nanocrystal films," *Nano Lett.*, vol. 8, p. 3488, 2008.

[18] I. J. Kramer, D. Zhitomirsky, J. D. Bass, P. M. Rice, T. Topuria, L. Krupp, S. M. Thon, A. H. Ip, R. Debnath, and H.-C. Kim, "Ordered nanopillar structured electrodes for depleted bulk heterojunction colloidal quantum dot solar cells," *Adv. Mater.*, vol. 24, p. 2315, 2012.

[19] X. Lan, J. Bai, S. Masala, S. M. Thon, Y. Ren, I. J. Kramer, S. Hoogland, A. Simchi, G. I. Koleilat, and D. Paz-Soldan, "Self-assembled, nanowire network electrodes for depleted bulk heterojunction solar cells," *Adv. Mater.*, vol. 25, p. 1769, 2013.

[20] C. Cheng, M. M. Lee, N. K. Noel, G. M. Hughes, J. M. Ball, H. E. Assender, H. J. Snaith, and A. A. R. Watt, "Polystyrene templated porous titania wells for quantum dot heterojunction solar cells," *ACS Appl. Mater. Interfaces*, vol. 6, p. 14247, 2014.

[21] J. Jean, S. Chang, P. R. Brown, J. J. Cheng, P. H. Rekemeyer, M. G. Bawendi, S. Gradecak, and V. Bulovic, "Zno nanowire arrays for enhanced photocurrent in PbS quantum dot solar cells," *Adv. Mater.*, vol. 25, p. 2790, 2013.

[22] A. K. Rath, M. Bernechea, L. Martinez, F. P. G. de Arquer, J. Osmond, and G. Konstantatos, "Solution-processed inorganic bulk nano-heterojunctions and their application to solar cells," *Nat. Photonics*, vol. 6, p. 529, 2012.

[23] R. Rossetti, S. Nakahara, and L. E. Brus, "Quantum size effects in the redox potentials, resonance Raman spectra, and electronic spectra of CdS crystallites in aqueous solution," *The Journal of Chemical Physics*, vol. 79, no. 2, p. 1086, 1983.

[24] M. A. Reed, J. N. Randall, R. J. Aggarwal, R. J. Matyi, T. M. Moore, and A. E. Wetsel, "Observation of discrete electronic states in a zero-dimensional semiconductor nanostructure," *Phys. Rev. Lett.*, vol. 60, pp. 535–537, Feb 1988.

[25] G. Konstantatos, I. Howard, A. Fischer, S. Hoogland, J. Clifford, E. Klem, L. Levina, and E. H. Sargent, "Ultrasensitive solution-cast quantum dot photodetectors," *Nature*, vol. 442, p. 180, 2006.

[26] L. Huang, C.-C. Tu, and L. Y. Lin, "Colloidal quantum dot photodetectors enhanced by self-assembled plasmonic nanoparticles," *Appl. Phys. Lett.*, vol. 98, p. 113110, 2011.

[27] S. Keuleyan, E. Lhuillier, V. Brajuskovic, and P. Guyot-Sionnest, "Mid-infrared hgte colloidal quantum dot photodetectors," *Nat. Photonics*, vol. 5, p. 489, 2011.

[28] L. Li, A. Pandey, D. J. Werder, B. P. Khanal, J. M. Pietryga, and V. I. Klimov, "Efficient synthesis of highly luminescent copper indium sulfide-based core/shell nanocrystals with surprisingly long-lived emission," *J. Am. Chem. Soc.*, vol. 133, p. 1176, 2011.

[29] J. S. Steckel, S. Coe-Sullivan, V. Bulovi, and M. G. Bawendi, "1.3 m to 1.55 m tunable electroluminescence from PbSe quantum dots embedded within an organic device," *Adv. Mater.*, vol. 15, p. 1862, 2003.

[30] L. Qian, Y. Zheng, J. Xue, and P. H. Holloway, "Stable and efficient quantum-dot light-emitting diodes based on solution-processed multilayer structures," *Nat. Photonics*, vol. 5, p. 543, 2011.

[31] W. W. Yu, L. Qu, W. Guo, and X. Peng, "Experimental determination of the extinction coefficient of CdTe, CdSe, and cds nanocrystals," *Chem. Mater.*, vol. 15, p. 2854, 2003.

[32] I. Moreels, Y. Justo, B. De Geyter, K. Haustraete, J. C. Martins, and Z. Hens, "Size-tunable, bright, and stable PbS quantum dots: A surface chemistry study," *ACS Nano*, vol. 5, p. 2004, 2011.

[33] C. d. M. Doneg, "Synthesis and properties of colloidal heteronanocrystals," *Chem. Soc. Rev.*, vol. 40, p. 1512, 2011.

[34] C. Steinhagen, M. G. Panthani, V. Akhavan, B. Goodfellow, B. Koo, and B. A. Korgel, "Synthesis of cu2znsns4 nanocrystals for use in low-cost photovoltaics," *Journal of the American Chemical Society*, vol. 131, no. 35, pp. 12554–12555, 2009.

[35] S. Kumar and T. Nann, "Shape control of ii–vi semiconductor nanomaterials," *Small*, vol. 2, no. 3, pp. 316–329, 2006.

[36] C. Murray, D. J. Norris, and M. G. Bawendi, "Synthesis and characterization of nearly monodisperse cde (e," *Journal of the American Chemical Society*, vol. 115, no. 19, pp. 8706–8715, 1993.

[37] J. Park, J. Joo, S. G. Kwon, Y. Jang, and T. Hyeon, "Synthesis of monodisperse spherical nanocrystals," *Angewandte Chemie International Edition*, vol. 46, no. 25, pp. 4630–4660, 2007.

[38] C. Burda, X. Chen, R. Narayanan, and M. A. El-Sayed, "Chemistry and properties of nanocrystals of different shapes," *Chemical reviews*, vol. 105, no. 4, pp. 1025–1102, 2005.

[39] D. V. Talapin, J.-S. Lee, M. V. Kovalenko, and E. V. Shevchenko, "Prospects of colloidal nanocrystals for electronic and optoelectronic applications," *Chemical reviews*, vol. 110, no. 1, pp. 389–458, 2009.

[40] F. Shieh, A. E. Saunders, and B. A. Korgel, "General shape control of colloidal Cds, CdSe, CdTe quantum rods and quantum rod heterostructures," *The Journal of Physical Chemistry B*, vol. 109, no. 18, pp. 8538–8542, 2005.

[41] S. Ahrenkiel, O. Mićić, A. Miedaner, C. Curtis, J. Nedeljković, and A. Nozik, "Synthesis and characterization of colloidal InP quantum rods," *Nano Letters*, vol. 3, no. 6, pp. 833–837, 2003.

[42] E. Lifshitz, M. Bashouti, V. Kloper, A. Kigel, M. Eisen, and S. Berger, "Synthesis and characterization of PbSe quantum wires, multipods, quantum rods, and cubes," *Nano Letters*, vol. 3, no. 6, pp. 857–862, 2003.

[43] N. G. Pavlopoulos, J. T. Dubose, N. Pinna, M.-G. Willinger, K. Char, and J. Pyun, "Synthesis and assembly of dipolar heterostructured tetrapods: Colloidal polymers with giant tert-butyl groups," *Angewandte Chemie*, vol. 128, no. 5, pp. 1819–1823, 2016.

[44] R. B. Vasiliev, D. N. Dirin, M. S. Sokolikova, S. G. Dorofeev, A. G. Vitukhnovsky, and A. M. Gaskov, "Growth of near-ir luminescent colloidal cdte/cds nanoheterostructures based on cdte tetrapods," *Mendeleev Communications*, vol. 19, no. 3, pp. 128–130, 2009.

[45] L. Manna, D. J. Milliron, A. Meisel, E. C. Scher, and A. P. Alivisatos, "Controlled growth of tetrapod-branched inorganic nanocrystals," *Nature materials*, vol. 2, no. 6, pp. 382–385, 2003.

[46] R. D. Schaller and V. I. Klimov, "High efficiency carrier multiplication in PbSe nanocrystals: implications for solar energy conversion," *Phys. Rev. Lett*, vol. 92, no. 18, p. 186601, 2004.

[47] J. E. Murphy, M. C. Beard, A. G. Norman, S. P. Ahrenkiel, J. C. Johnson, P. Yu, O. I. Micic, R. J. Ellingson, and A. J. Nozik, "Pbte colloidal nanocrystals: synthesis, characterization, and multiple exciton generation," *J. A. Chem. Soc.*, vol. 128, no. 10, pp. 3241–3247, 2006.

[48] R. D. Schaller, M. A. Petruska, and V. I. Klimov, "Effect of electronic structure on carrier multiplication efficiency: Comparative study of PbSe and CdSe nanocrystals," *Appl. Phys. Lett*, vol. 87, no. 25, p. 253102, 2005.

[49] J. Pijpers, E. Hendry, M. Milder, R. Fanciulli, J. Savolainen, J. Herek, D. Vanmaekelbergh, S. Ruhman, D. Mocatta, D. Oron, *et al.*, "Carrier multiplication and its reduction by photodoping in colloidal inas quantum dots," *J. Phys. Chem. C*, vol. 111, no. 11, pp. 4146–4152, 2007.

[50] M. C. Beard, K. P. Knutsen, P. Yu, J. M. Luther, Q. Song, W. K. Metzger, R. J. Ellingson, and A. J. Nozik, "Multiple exciton generation in colloidal silicon nanocrystals," *Nano Lett*, vol. 7, no. 8, pp. 2506–2512, 2007.

[51] V. Sukhovatkin, S. Hinds, L. Brzozowski, and E. H. Sargent, "Colloidal quantum-dot photodetectors exploiting multiexciton generation," *Science*, vol. 324, pp. 1542–1545, 2009.

[52] O. E. Semonin, J. M. Luther, S. Choi, H. Chen, J. Gao, A. J. Nozik, and M. C. Beard, "Peak external photocurrent quantum efficiency exceeding 100% via meg in a quantum dot solar cell," *Science*, vol. 334, no. 6062, pp. 1530–1533, 2011.

[53] M. Califano, A. Zunger, and A. Franceschetti, "Efficient inverse auger recombination at threshold in CdSe nanocrystals," *Nano Lett.*, vol. 4, no. 3, pp. 525–531, 2004.

[54] A. Franceschetti, J. M. An, and A. Zunger, "Impact ionization can explain carrier multiplication in PbSe quantum dots," *Nano Lett.*, vol. 6, no. 10, pp. 2191–2195, 2006.

[55] G. Allan and C. Delerue, "Role of impact ionization in multiple exciton generation in PbSe nanocrystals," *Phys. Rev. B*, vol. 73, p. 205423, 2006.

[56] R. D. Schaller, V. M. Agranovich, and V. I. Klimov, "High-efficiency carrier multiplication through direct photogeneration of multi-excitons via virtual single-exciton states," *Nat. Phys*, vol. 1, no. 3, pp. 189–194, 2005.

[57] R. J. Ellingson, M. C. Beard, J. C. Johnson, P. Yu, O. I. Micic, A. J. Nozik, A. Shabaev, and A. L. Efros, "Highly efficient multiple exciton generation in

colloidal PbSe and PbS quantum dots," *Nano Lett.*, vol. 5, no. 5, pp. 865–871, 2005.

[58] A. Sills and M. Califano, "Origins of improved carrier multiplication efficiency in elongated semiconductor nanostructures," *Physical Chemistry Chemical Physics*, vol. 17, no. 4, pp. 2573–2581, 2015.

[59] R. Schaller, M. Sykora, J. Pietryga, and V. Klimov, "Seven excitons at a cost of one: redefining the limits for conversion efficiency of photons into charge carriers," *Nano Lett.*, vol. 6, no. 3, pp. 424–429, 2006.

[60] A. G. Midgett, J. M. Luther, J. T. Stewart, D. K. Smith, L. A. Padilha, V. I. Klimov, A. J. Nozik, and M. C. Beard, "Size and composition dependent multiple exciton generation efficiency in PbS, PbSe, and PbSxse1x alloyed quantum dots," *Nano Lett.*, vol. 13, no. 7, pp. 3078–3085, 2013.

[61] P. D. Cunningham, J. E. Boercker, E. E. Foos, M. P. Lumb, A. R. Smith, J. G. Tischler, and J. S. Melinger, "Enhanced multiple exciton generation in quasi-one-dimensional semiconductors," *Nano Lett.*, vol. 11, no. 8, pp. 3476–3481, 2011.

[62] P. D. Cunningham, J. E. Boercker, E. E. Foos, M. P. Lumb, A. R. Smith, J. G. Tischler, and J. S. Melinger, "Correction to enhanced multiple exciton generation in quasi-one-dimensional semiconductors," *Nano Lett.*, vol. 13, no. 6, pp. 3003–3003, 2013.

[63] R. L. Sandberg, L. A. Padilha, M. M. Qazilbash, W. K. Bae, R. D. Schaller, J. M. Pietryga, M. J. Stevens, B. Baek, S. W. Nam, and V. I. Klimov, "Multiexciton dynamics in infrared-emitting colloidal nanostructures probed by a

superconducting nanowire single-photon detector," *ACS. Nano.*, vol. 6, no. 11, pp. 9532–9540, 2012.

[64] J. Yang, B.-R. Hyun, A. J. Basile, and F. W. Wise, "Exciton relaxation in PbSe nanorods," *ACS Nano*, vol. 6, no. 9, pp. 8120–8127, 2012.

[65] L. A. Padilha, J. T. Stewart, R. L. Sandberg, W. K. Bae, W.-K. Koh, J. M. Pietryga, and V. I. Klimov, "Aspect ratio dependence of auger recombination and carrier multiplication in PbSe nanorods," *Nano Lett.*, vol. 13, no. 3, pp. 1092–1099, 2013.

[66] M. C. Beard, J. M. Luther, O. E. Semonin, and A. J. Nozik, "Third generation photovoltaics based on multiple exciton generation in quantum confined semiconductors," *Acc. Chem. Res.*, vol. 46, no. 6, pp. 1252–1260, 2012.

[67] A. C. Bartnik, A. L. Efros, W. K. Koh, C. B. Murray, and F. W. Wise, "Electronic states and optical properties of PbSe nanorods and nanowires," *Phys. Rev. B*, vol. 82, no. 19, p. 195313, 2010.

[68] J. A. McGuire, J. Joo, J. M. Pietryga, R. D. Schaller, and V. I. Klimov, "New aspects of carrier multiplication in semiconductor nanocrystals," *Acc. Chem. Res*, vol. 41, no. 12, pp. 1810–1819, 2008.

[69] V. I. Klimov, "Mechanisms for photogeneration and recombination of multiexcitons in semiconductor nanocrystals: implications for lasing and solar energy conversion," *J. Phys. Chem. B*, vol. 110, no. 34, pp. 16827–16845, 2006.

[70] M. C. Beard, A. G. Midgett, M. C. Hanna, J. M. Luther, B. K. Hughes, and A. J. Nozik, "Comparing multiple exciton generation in quantum dots to impact

ionization in bulk semiconductors: Implications for enhancement of solar energy conversion," *Nano Lett.*, vol. 10, no. 8, pp. 3019–3027, 2010.

[71] R. D. Schaller, J. M. Pietryga, and V. I. Klimov, "Carrier multiplication in inas nanocrystal quantum dots with an onset defined by the energy conservation limit," *Nano Lett.*, vol. 7, no. 11, pp. 3469–3476, 2007.

[72] L.-W. Wang, M. Califano, A. Zunger, and A. Franceschetti, "Pseudopotential theory of auger processes in CdSe quantum dots," *Phys. Rev. Lett.*, vol. 91, no. 5, pp. 056404–1–056404–4, 2003.

[73] J. W. Luo, A. Franceschetti, and A. Zunger, "Carrier multiplication in semiconductor nanocrystals: Theoretical screening of candidate materials based on band-structure effects," *Nano Lett.*, vol. 8, no. 10, pp. 3174–3181, 2008.

[74] K. Hyeon-Deuk and O. V. Prezhdo, "Multiple exciton generation and recombination dynamics in small Si and CdSe quantum dots: an ab inition time-domain study," *ACS Nano*, vol. 6, pp. 1239–1250, 2012.

[75] J. M. An, A. Franceschetti, S. V. Dudiy, and A. Zunger, "The peculiar electronic structure of PbSe quantum dots," *Nano Lett.*, vol. 6, no. 12, pp. 2728–2735, 2006.

[76] S. Ithurria, M. Tessier, B. Mahler, R. Lobo, B. Dubertret, and A. L. Efros, "Colloidal nanoplatelets with two-dimensional electronic structure," *Nature Mater.*, vol. 10, no. 12, pp. 936–941, 2011.

[77] M. D. Tessier, C. Javaux, I. Maksimovic, V. Loriette, and B. Dubertret, "Spectroscopy of single CdSe nanoplatelets," *ACS Nano*, vol. 6, no. 8, pp. 6751–6758, 2012.

[78] K. P. Rice, A. E. Saunders, and M. P. Stoykovich, "Seed-mediated growth of shape-controlled wurtzite CdSe nanocrystals: Platelets, cubes, and rods," *J. Amer. Chem. Soc.*, vol. 135, no. 17, pp. 6669–6676, 2013.

[79] T. Mokari, M. Zhang, and P. Yang, "Shape, size, and assembly control of pbte nanocrystals," *J. A. Chem. Soc.*, vol. 129, no. 32, pp. 9864–9865, 2007.

[80] Z. Quan, W. Siu Loc, C. Lin, Z. Luo, K. Yang, Y. Wang, H. Wang, Z. Wang, and J. Fang, "Tilted face-centered-cubic supercrystals of PbS nanocubes," *Nano Lett.*, vol. 12, no. 8, pp. 4409–4413, 2012.

[81] H. et al *Science*, vol. 348, no. 6240, pp. 1226–1230, 2015.

[82] G. Bryant and W. Jaskolski, "Surface effects on capped and uncapped nanocrystals," *J. Phys. Chem. B*, vol. 109, no. 42, pp. 19650–19656, 2005.

[83] I. Kang and F. W. Wise, "Electronic structure and optical properties of PbS and PbSe quantum dots," *J. Opt. Soc. Am. B*, vol. 14, no. 7, pp. 1632–1646, 1997.

[84] A. L. Efros and M. Rosen, "The electronic structure of semiconductor nanocrystals 1," *Annu. Rev. Mater Sci*, vol. 30, no. 1, pp. 475–521, 2000.

[85] Y. H. Zhu, X. W. Zhang, and J. B. Xia *Phys. Rev. B*, vol. 73, p. 165326, 2006.

[86] G. Zohar, R. Baer, and E. Rabani, "Multiexciton generation in ivvi nanocrystals: The role of carrier effective mass, band mixing, and phonon emission," *J. Phys. Chem. Lett*, vol. 4, no. 2, pp. 317–322, 2013.

[87] C. Delerue and M. Lannoo, *Nanostructures: Theory and Modelling.* (Springer, New York 2004).

[88] S. Lee, L. Jönsson, J. W. Wilkins, G. W. Bryant, and G. Klimeck *Phys. Rev. B*, vol. 63, p. 195318, 2001.

[89] R. Viswanatha, S. Sapra, T. Saha-Dasgupta, and D. Sarma, "Electronic structure of and quantum size effect in iii-v and ii-vi semiconducting nanocrystals using a realistic tight binding approach," *Phys. Rev. B*, vol. 72, no. 4, p. 045333, 2005.

[90] F. Trani, G. Cantele, D. Ninno, and G. Iadonisi, "Tight-binding calculation of the optical absorption cross section of spherical and ellipsoidal silicon nanocrystals," *Phys. Rev. B*, vol. 72, no. 7, p. 075423, 2005.

[91] J. Diaz and G. W. Bryant, "Electronic and optical fine structure of gaas nanocrystals: The role of d orbitals in a tight-binding approach," *Physical Review B*, vol. 73, no. 7, p. 075329, 2006.

[92] M. Korkusinski, O. Voznyy, and P. Hawrylak, "Fine structure and size dependence of exciton and biexciton optical spectra in CdSe nanocrystals," *Phys. Rev. B*, vol. 82, no. 24, p. 245304, 2010.

[93] L.-W. Wang and A. Zunger, "Solving schrödingers equation around a desired energy: application to silicon quantum dots," *J. Chem. Phys.*, vol. 100, no. 3, pp. 2394–2397, 1994.

[94] A. Canning, L. Wang, A. Williamson, and A. Zunger, "Parallel empirical pseudopotential electronic structure calculations for million atom systems," *J. Comp. Phys.*, vol. 160, no. 1, pp. 29–41, 2000.

[95] J. Chelikowsky *J. Phys. D*, vol. 33, p. R33, 2000.

[96] A. Puzder, A. Williamson, J. C. Grossman, and G. Galli *Phys. Rev. Lett*, vol. 88, no. 9, p. 097401, 2002.

[97] L.-W. Wang and J. Li *Phys. Rev. B*, vol. 69, p. 153302, 2004.

[98] M. Marsili, S. Botti, M. Palummo, E. Degoli, O. Pulci, H.-C. Weissker, M. Marques, S. Ossicini, and R. Del Sole *J. Phys. Chem. C*, vol. 117, pp. 14229–14234, 2013.

[99] M. Govoni, I. Marri, and S. Ossicini, "Carrier multiplication between interacting nanocrystals for fostering silicon-based photovoltaics," *Nature Photon.*, vol. 6, no. 10, pp. 672–679, 2012.

[100] A. Kryjevski and D. Kilin, "Multiple exciton generation in silicon quantum dot arrays: density functional perturbation theory computation," *Mol. Phys.*, vol. 112, no. 3-4, pp. 430–440, 2014.

[101] M. Zieliński, "Including strain in atomistic tight-binding hamiltonians: An application to self-assembled inas/gaas and inas/InP quantum dots," *Phys. Rev. B*, vol. 86, no. 11, p. 115424, 2012.

[102] O. V. Prezhdo, "Photoinduced dynamics in semiconductor quantum dots: Insights from time-domain ab initio studies," *Acc. Chem. Res*, vol. 42, no. 12, pp. 2005–2016, 2009.

[103] A. Yoffe, "Low-dimensional systems: quantum size effects and electronic properties of semiconductor microcristallites (zero-dimensional systems) and some quasi-two-dimensional systems," *Adv. Phys.*, vol. 42, no. 2, pp. 173–266, 1993.

[104] A. Hafaiedh and N. Bouarissa, "Quantum confinement effects on energy gaps and electron and hole effective masses of quantum well aln," *Physica E: Low-dimensional Systems and Nanostructures*, vol. 43, no. 9, pp. 1638–1641, 2011.

[105] N. H. M. Al Wadiy, N. Bouarissa, and M. A. Khan, "Quantum confinement effects on the band structure and dielectric properties of nanostructured gaas," *Physica Scripta*, vol. 84, no. 1, p. 015704, 2011.

[106] J. Peng and G. Bester, "Charged excitons and biexcitons in laterally coupled (in, ga) as quantum dots," *Physical Review B*, vol. 82, no. 23, p. 235314, 2010.

[107] P. Franco and M. I. P. Shamos, "Computational geometry: an introduction," 1985.

[108] J. C. Phillips and L. Kleinman, "New method for calculating wave functions in crystals and molecules," *Physical Review*, vol. 116, no. 2, p. 287, 1959.

[109] P. Harrison and A. Valavanis, *Quantum wells, wires and dots: theoretical and computational physics of semiconductor nanostructures*. John Wiley & Sons, 2016.

[110] E. K. Gross and R. M. Dreizler, *Density functional theory*, vol. 337. Springer Science & Business Media, 2013.

[111] D. Vanderbilt, "Soft self-consistent pseudopotentials in a generalized eigenvalue formalism," *Physical Review B*, vol. 41, no. 11, p. 7892, 1990.

[112] G. Bester, "Electronic excitations in nanostructures: an empirical pseudopotential based approach," *Journal of Physics: Condensed Matter*, vol. 21, no. 2, p. 023202, 2008.

[113] C. Vömel, S. Z. Tomov, O. A. Marques, A. Canning, L.-W. Wang, and J. J. Dongarra, "State-of-the-art eigensolvers for electronic structure calculations of large scale nano-systems," *Journal of Computational Physics*, vol. 227, no. 15, pp. 7113–7124, 2008.

[114] Y. Zhou and Y. Saad, "A chebyshev–davidson algorithm for large symmetric eigenproblems," *SIAM Journal on Matrix Analysis and Applications*, vol. 29, no. 3, pp. 954–971, 2007.

[115] A. Canning, O. Marques, C. Voemel, L.-W. Wang, J. Dongarra, J. Langou, and S. Tomov, "New eigensolvers for large-scale nanoscience simulations," in *Journal of Physics: Conference Series*, vol. 125, p. 012074, IOP Publishing, 2008.

[116] A. Franceschetti, H. Fu, L. Wang, and A. Zunger, "Many-body pseudopotential theory of excitons in InP and CdSe quantum dots," *Physical Review B*, vol. 60, no. 3, p. 1819, 1999.

[117] M. Califano, A. Franceschetti, and A. Zunger, "Lifetime and polarization of the radiative decay of excitons, biexcitons, and trions in CdSe nanocrystal quantum dots," *Physical Review B*, vol. 75, no. 11, p. 115401, 2007.

[118] J. Bang, H. Yang, and P. H. Holloway, "Enhanced and stable green emission of zno nanoparticles by surface segregation of mg," *Nanotechnology*, vol. 17, no. 4, p. 973, 2006.

[119] F. Le Formal, N. Tétreault, M. Cornuz, T. Moehl, M. Grätzel, and K. Sivula, "Passivating surface states on water splitting hematite photoanodes with alumina overlayers," *Chemical Science*, vol. 2, no. 4, pp. 737–743, 2011.

[120] D. A. Hines and P. V. Kamat, "Recent advances in quantum dot surface chemistry," *ACS applied materials & interfaces*, vol. 6, no. 5, pp. 3041–3057, 2014.

[121] B. K. Hughes, D. A. Ruddy, J. L. Blackburn, D. K. Smith, M. R. Bergren, A. J. Nozik, J. C. Johnson, and M. C. Beard, "Control of PbSe quantum dot surface chemistry and photophysics using an alkylselenide ligand," *ACS nano*, vol. 6, no. 6, pp. 5498–5506, 2012.

[122] A. H. Ip, S. M. Thon, S. Hoogland, O. Voznyy, D. Zhitomirsky, R. Debnath, L. Levina, L. R. Rollny, G. H. Carey, A. Fischer, *et al.*, "Hybrid passivated colloidal quantum dot solids," *Nature nanotechnology*, vol. 7, no. 9, pp. 577–582, 2012.

[123] P. R. Brown, D. Kim, R. R. Lunt, N. Zhao, M. G. Bawendi, J. C. Grossman, and V. Bulovic, "Energy level modification in lead sulfide quantum dot thin films through ligand exchange," *ACS nano*, vol. 8, no. 6, pp. 5863–5872, 2014.

[124] E. J. Klem, H. Shukla, S. Hinds, D. D. MacNeil, L. Levina, and E. H. Sargent, "Impact of dithiol treatment and air annealing on the conductivity, mobility, and hole density in PbS colloidal quantum dot solids," *Applied Physics Letters*, vol. 92, no. 21, p. 212105, 2008.

[125] J. M. Luther, M. Law, M. C. Beard, Q. Song, M. O. Reese, R. J. Ellingson, and A. J. Nozik, "Schottky solar cells based on colloidal nanocrystal films," *Nano letters*, vol. 8, no. 10, pp. 3488–3492, 2008.

[126] G. I. Koleilat, L. Levina, H. Shukla, S. H. Myrskog, S. Hinds, A. G. Pattantyus-Abraham, and E. H. Sargent, "Efficient, stable infrared photovoltaics based on

solution-cast colloidal quantum dots," *ACS nano*, vol. 2, no. 5, pp. 833–840, 2008.

[127] D. V. Talapin and C. B. Murray, "PbSe nanocrystal solids for n-and p-channel thin film field-effect transistors," *Science*, vol. 310, no. 5745, pp. 86–89, 2005.

[128] A. G. Pattantyus-Abraham, I. J. Kramer, A. R. Barkhouse, X. Wang, G. Konstantatos, R. Debnath, L. Levina, I. Raabe, M. K. Nazeeruddin, M. Gratzel, *et al.*, "Depleted-heterojunction colloidal quantum dot solar cells," *ACS nano*, vol. 4, no. 6, pp. 3374–3380, 2010.

[129] J. Tang, K. W. Kemp, S. Hoogland, K. S. Jeong, H. Liu, L. Levina, M. Furukawa, X. Wang, R. Debnath, D. Cha, *et al.*, "Colloidal-quantum-dot photovoltaics using atomic-ligand passivation," *Nature materials*, vol. 10, no. 10, pp. 765–771, 2011.

[130] A. Puzder, A. J. Williamson, N. Zaitseva, G. Galli, L. Manna, and A. P. Alivisatos, "The effect of organic ligand binding on the growth of CdSe nanoparticles probed by ab initio calculations," *Nano Letters*, vol. 4, no. 12, pp. 2361–2365, 2004.

[131] M. Califano, G. Bester, and A. Zunger, "Prediction of a shape-induced enhancement in the hole relaxation in nanocrystals," *Nano Letters*, vol. 3, no. 9, pp. 1197–1202, 2003.

[132] P. a. Graf, K. Kim, W. B. Jones, and L.-W. Wang, "Surface passivation optimization using DIRECT," *Journal of Computational Physics*, vol. 224, pp. 824–835, June 2007.

[133] M. T. Frederick and E. A. Weiss, "Relaxation of exciton confinement in CdSe quantum dots by modification with a conjugated dithiocarbamate ligand," *ACS nano*, vol. 4, no. 6, pp. 3195–3200, 2010.

[134] R. D. Harris, V. A. Amin, B. Lau, and E. A. Weiss, "Role of interligand coupling in determining the interfacial electronic structure of colloidal cds quantum dots," *ACS nano*, vol. 10, no. 1, pp. 1395–1403, 2016.

[135] S. Lian, D. J. Weinberg, R. D. Harris, M. S. Kodaimati, and E. A. Weiss, "Subpicosecond photoinduced hole transfer from a cds quantum dot to a molecular acceptor bound through an exciton-delocalizing ligand," *ACS nano*, vol. 10, no. 6, pp. 6372–6382, 2016.

[136] M. T. Frederick, V. A. Amin, L. C. Cass, and E. A. Weiss, "A molecule to detect and perturb the confinement of charge carriers in quantum dots," *Nano letters*, vol. 11, no. 12, pp. 5455–5460, 2011.

[137] X. Zhao, C. M. Wei, L. Yang, and M. Y. Chou, "Quantum Confinement and Electronic Properties of Silicon Nanowires," *Physical Review Letters*, vol. 92, p. 236805, June 2004.

[138] D. Medaboina, V. Gade, S. Patil, and S. Khare, "Effect of structure, surface passivation, and doping on the electronic properties of Ge nanowires: A first-principles study," *Physical Review B*, vol. 76, p. 205327, Nov. 2007.

[139] X. Huang, E. Lindgren, and J. R. Chelikowsky, "Surface passivation method for semiconductor nanostructures," *Physical Review B*, vol. 71, no. 16, p. 165328, 2005.

[140] H.-x. Deng, S.-s. Li, and J. Li, "Quantum Confinement Effects and Electronic Properties of SnO 2 Quantum Wires and Dots," pp. 4841–4845, 2010.

[141] J. Wang, S.-S. Li, Y. Liu, and J. Li, "Passivation of CuI Quantum Dots," *The Journal of Physical Chemistry C*, vol. 116, pp. 21039–21045, Oct. 2012.

[142] A. Molina-Sanchez, A. García-Cristóbal, and G. Bester, "Semiempirical pseudopotential approach for nitride-based nanostructures and ab initio based passivation of free surfaces," *Physical Review B*, vol. 86, no. 20, p. 205430, 2012.

[143] J.-W. Luo, A. Franceschetti, and A. Zunger, "Quantum-size-induced electronic transitions in quantum dots: Indirect band-gap gaas," *Physical Review B*, vol. 78, no. 3, p. 035306, 2008.

[144] A. Williamson, A. Franceschetti, H. Fu, L. Wang, and A. Zunger, "Indirect band gaps in quantum dots made from direct-gap bulk materials," *Journal of electronic materials*, vol. 28, no. 5, pp. 414–425, 1999.

[145] A. Sills, P. Harrison, and M. Califano, "Exciton dynamics in InSb colloidal quantum dots," *The journal of physical chemistry letters*, vol. 7, no. 1, pp. 31–35, 2015.

[146] O. Madelung, U. Rössler, and M. Schulz, "Group iv elements, iv-iv and iii-v compounds," *Part a–Lattice Properties, Landolt-Börnstein–Group III Condensed Matter*, vol. 41, 2001.

[147] W. Liu, A. Y. Chang, R. D. Schaller, and D. V. Talapin, "Colloidal InSb nanocrystals," *Journal of the American Chemical Society*, vol. 134, no. 50, pp. 20258–20261, 2012.

[148] A. Y. Chang, W. Liu, D. V. Talapin, and R. D. Schaller, "Carrier dynamics in highly quantum-confined, colloidal indium antimonide nanocrystals," *ACS nano*, vol. 8, no. 8, pp. 8513–8519, 2014.

[149] V. I. Klimov, A. A. Mikhailovsky, D. McBranch, C. A. Leatherdale, and M. G. Bawendi, "Quantization of multiparticle auger rates in semiconductor quantum dots," *Science*, vol. 287, no. 5455, pp. 1011–1013, 2000.

[150] V. I. Klimov, "Optical nonlinearities and ultrafast carrier dynamics in semiconductor nanocrystals," 2000.

[151] A. Pandey and P. Guyot-Sionnest, "Multicarrier recombination in colloidal quantum dots," 2007.

[152] L.-W. Wang, M. Califano, A. Zunger, and A. Franceschetti, "Pseudopotential theory of auger processes in CdSe quantum dots," *Physical review letters*, vol. 91, no. 5, p. 056404, 2003.

[153] R. D. Schaller, J. M. Pietryga, and V. I. Klimov, "Carrier multiplication in inas nanocrystal quantum dots with an onset defined by the energy conservation limit," *Nano letters*, vol. 7, no. 11, pp. 3469–3476, 2007.

[154] M. Shim, S. V. Shilov, M. S. Braiman, and P. Guyot-Sionnest, "Long-lived delocalized electron states in quantum dots: a step-scan fourier transform infrared study," *The Journal of Physical Chemistry B*, vol. 104, no. 7, pp. 1494–1496, 2000.

[155] P. Kambhampati, "Hot exciton relaxation dynamics in semiconductor quantum dots: radiationless transitions on the nanoscale," *The Journal of Physical Chemistry C*, vol. 115, no. 45, pp. 22089–22109, 2011.

[156] M. Califano, "Photoinduced surface trapping and the observed carrier multiplication yields in static CdSe nanocrystal samples," *ACS nano*, vol. 5, no. 5, pp. 3614–3621, 2011.

[157] A. L. Efros and M. Rosen, "Quantum size level structure of narrow-gap semiconductor nanocrystals: Effect of band coupling," *Physical Review B*, vol. 58, no. 11, p. 7120, 1998.

[158] D. Kim, D.-H. Kim, J.-H. Lee, and J. C. Grossman, "Impact of stoichiometry on the electronic structure of PbS quantum dots," *Physical review letters*, vol. 110, no. 19, p. 196802, 2013.

[159] L.-W. Wang and A. Zunger, "Local-density-derived semiempirical pseudopotentials," *Physical Review B*, vol. 51, no. 24, p. 17398, 1995.

[160] A. Franceschetti, H. Fu, L. Wang, and A. Zunger, "Many-body pseudopotential theory of excitons in InP and CdSe quantum dots," *Physical Review B*, vol. 60, no. 3, p. 1819, 1999.

[161] W. Sukkabot, "Tight-binding theory of the excitonic states in colloidal InSb nanostructures," *Materials Science in Semiconductor Processing*, vol. 27, pp. 51–55, 2014.

[162] D. V. Talapin, J. H. Nelson, E. V. Shevchenko, S. Aloni, B. Sadtler, and A. P. Alivisatos, "Seeded growth of highly luminescent CdSe/CdS nanoheterostructures with rod and tetrapod morphologies," *Nano letters*, vol. 7, no. 10, pp. 2951–2959, 2007.

[163] J. Li, "Shape effects on electronic states of nanocrystals," *Nano letters*, vol. 3, no. 10, pp. 1357–1363, 2003.